2015

Fabrication of gamma titanium aluminide alloys by gas tungsten arc welding-based additive layer manufacturing

Yan Ma
University of Wollongong

FABRICATION OF GAMMA TITANIUM ALUMINIDE ALLOYS BY GAS TUNGSTEN ARC WELDING-BASED ADDITIVE LAYER MANUFACTURING

A thesis submitted in fulfilment of the requirements

for the award of the degree

DOCTOR OF PHILOSOPHY

from

UNIVERSITY OF WOLLONGONG

By

YAN MA

B. Eng., M. Eng.

School of Mechanical, Materials and Mechatronics Engineering

Faculty of Engineering and Information Sciences

March, 2015

Declaration

I, Yan Ma, declare that this thesis, submitted in fulfilment of the requirements for award of Doctor of Philosophy, in the School of Mechanical, Materials and Mechatronics Engineering, University of Wollongong, Australia, is wholly my own work unless otherwise referenced or acknowledged. The document has not been submitted for qualifications at any other academic institution.

Yan Ma

Signature:

March, 2015

Acknowledgements

First and foremost, I wish to express my sincere appreciation and gratitude to my principal supervisor, Prof. Huijun Li, for giving me an invaluable opportunity to pursue my study in the University of Wollongong (UOW). I am greatly indebted to Huijun for his valuable guidance, constant encouragement, support and friendship during the course of this study. Without his help I would never have completed this work.

I am deeply grateful to my co-supervisors, Dr. Dominic Cuiuri and Dr. Zengxi Pan, for their strong guidance, informative discussion and close supervision. It was a great pleasure working with them. Special thanks are extended to Dominic for his patience and assistance with the manufacturing process.

I wish to acknowledge the staff from the Australia Nuclear Science and Technology Organisation (ANSTO) and The Open University (OU) in the United Kingdom. I am grateful to Prof. Klaus-Dieter Liss from ANSTO for his assistance in the neutron phase transformation experiments, Dr. Anna Paradowska and Dr. Mark Reid from ANSTO and Dr Sanjooram Paddea from OU for the residual stresses measurements.

I would like to convey sincere appreciation to the staff and my fellow graduate students in the Faculty of Engineering and Information Science. Special thanks go to Mr. Greg Tillman for his friendship and tremendous assistance in metallographic preparation, Mr. Chen Shen for his great help in producing components and samples preparation for the neutron diffraction experiments. I wish to thank Dr. David Wexler, Mr. Stuart Rodd, Mr. Nick Mackie and Mr. Tony Remo for their technical assistance. I also thank Dr. Nicholas Hoye for his help during the manufacturing process, Dr. Liang Chen, Dr. Zhixiong Zhu, Dr. Zhiyang Wang, Dr. Jian Han and Mr. Chen Shen for their discussion and friendship.

I also appreciate the assistance from the China Scholarship Council (CSC), University of Wollongong (UOW) and the Welding Technology Institute of Australia (WTIA) for providing the scholarships to support my study.

Last but not least, I would like to thank my family for their love, patience, understanding and constant support during the progression of this thesis.

Abstract

Although intermetallic titanium aluminide alloys have extensive practical industrial applications owing to their unique characteristics, their usage has been limited by the difficulties and high cost of fabrication.

This research proposes an alternative manufacturing approach to fabricating titanium aluminide alloys, which combines in-situ alloying and additive layer manufacturing (ALM) using gas tungsten arc welding (GTAW). This new fabrication process promises significant time and cost saving in comparison to traditional methods. Since the chemical composition, microstructural features and mechanical performance of the as-fabricated components can be greatly influenced by the manufacturing parameters, the effect of several important variables including arc current, interpass temperature and wire feed rate have been investigated in this study. Suitable parameters for producing crack-free components have been determined.

Apart from the process parameters, it is also important to evaluate the microstructural evolution and the variation of mechanical properties in relation to the location within one build. The typical additively layer manufactured γ-TiAl based alloy consists of comparatively large α_2 grains in the near-substrate zone, fully lamellar colonies with various sizes and interdendritic γ structure in the intermediate layer bands, followed by fine dendrites and interdendritic γ phases in the top region. Microhardness measurements and tensile testing results indicate relatively homogeneous mechanical characteristics throughout the deposited material. The exception to this homogeneity occurs in the near-substrate zone immediately adjacent to the pure Ti substrate used in these experiments, where the alloying process is not as well controlled as in the higher regions. The tensile properties are also different for the vertical (build) direction and horizontal (travel) direction because of the differing microstructure in each direction.

Various post production heat treatments have been carried out on the as-fabricated components. The contour method was used to measure the residual stresses, which were clearly reduced by applying the low temperature heat treatment. The degree of stress relief is greater as the treatment temperature is increased from 400 to 500 °C. Investigations were also conducted to assess the influence of various heat treatment conditions on the microstructure evolution, phase transformations and mechanical properties. Post production heat treatment at 1200 °C for 12 hours led to full transformation of the dendritic structure, while interdendritic areas were still visible in the heat-treated samples at 1060 °C for the same duration. A different microstructure was finally produced by heat treatment at 1200 °C and 1060 °C for 24 h, exhibiting equiaxed γ grains and fully lamellar colonies respectively. The heat-treated samples at 1200 °C / 24 h possessed higher ductility but lower strength compared with the as-fabricated samples, while the 1060 °C / 24 h treatment resulted in the highest strength but poor ductility (0.4 %). Additionally, the relatively homogenous microstructure in the majority region after all post production heat treatments effectively eliminated the anisotropy of mechanical properties for the vertical and horizontal directions.

Finally, the GTAW-based ALM process with twin wire in situ alloying was used to successfully produce functionally graded TiAl alloy with a compositional gradient ranging from pure Ti at the substrate to Ti-50 at.% Al at the maximum height of the deposition. The microstructure and chemical composition were characterised using optical microscopy and electron microscopy. Microstructural features across the graded composition correspond to those typically observed in conventional α-Ti, Ti_3Al- and TiAl-based alloys. The microhardness profile with the composition gradient showed a linear variation of hardness as a function of composition, with the range of 25~33 at.% Al exhibiting the highest microhardness value with only a slight fluctuation of hardness value throughout this range. The morphology and amount of α_2 phase could offer a reasonable explanation for the above phenomenon.

List of Figures

List of Tables

List of Abbreviations and Symbols

1. Abbreviations

ALM	additive layer manufacturing
GTAW	gas tungsten arc welding
FGMs	functionally graded materials
Ti	chemical element – Ti
Al	chemical element – Al
TiAl	titanium aluminide – intermetallic compound
Ti_3Al	titanium aluminide – intermetallic compound
$TiAl_3$	titanium aluminide – intermetallic compound
$TiAl_2$	titanium aluminide – intermetallic compound
Ti_xAl_y	titanium aluminide – intermetallic compound
SF	stacking faults
APB	antiphase boundaries
BDTT	brittle to ductile transition temperature
IM	ingot metallurgy
ISM	induction skull melting
VAR	vacuum arc melting
PAM	plasma arc melting
HIP	hot-isostatic pressing

PM	Powder metallurgy
AM	Additive manufacturing
3D	three-dimensional
SFF	solid freeform fabrication
RM	rapid manufacturing
3DP	3D printing
RP	Rapid prototyping
CAD	computer-aided design
LMD	Laser melting deposition
EBM	electron beam melting
H_2O	water
HNO_3	concentrated nitric acid
HF	hydrofluoric acid
OM	Optical Microcopy
SEM	scanning electron microscopy
EDS	energy dispersive X-ray spectroscopy
XRD	X-ray diffraction
WOMBAT	high intensity powder diffractometer
ANSTO	Australian Nuclear Science and Technology Organisation
WAALM	wire and arc additive layer manufacturing
HAZ	heat affected zone

Z	the build direction
X	the lateral direction
Y	the travel direction
UTS	ultimate tensile strength
YS	yield strength
EL	Elongation
L	liquid
PST	polysynthetically twinned crystals
CCT	continuous cooling transformation
EDM	electro-discharge machine
CMM	coordinate measuring machine
2D	two-dimensional
DC	discontinuous coarsening
FGMMC	functionally graded metal matrix composites
TIG	tungsten inert gas

2. Symbols

γ	gamma phase, face-centred tetragonal structure in TiAl
α_2	alpha 2 phase, hexagonal structure in Ti_3Al
β	beta phase, body-centred cubic structure in Ti
α	alpha phase, face-centred cubic structure in Ti

°C	Celsius degree
$g \cdot cm^{-3}$	gram per cubic centimetre
at.%	atom percent
σ_y	yield strength
$\sigma_{0,y}$	lattice frictional stress
k_y	dislocation unpinning parameter
d	average grain diameter
L/min	litre per minute
mm/min	millimetre per minute
wt.%	weight percent
rpm	revolutions per minute
mm/s	millimetre per seconds
λ	wavelength
Å	Angstrom
°	degree
min^{-1}	per minute
kV	Kilovolts
mA	milliampere
g	gram
s^{-1}	per seconds

Q	the heat input
E	the voltage
I	the arc current
n	the electrode efficiency
v	the welding speed
J/mm	Joule per millimetre
V	volt
A	ampere
HV0.2	unit of the Vickers microhardness (indentation load of 200 g)
θ	theta
μm	micrometer
MPa	megapascal
T_β	beta transus temperature
T_s	solidus temperature
T_L	liquidus temperature
nm	nanometre
h	hours
Te	eutectoid temperature

Table of Contents

1 Introduction

1.1 General

Titanium aluminide alloys based on the intermetallic phases γ (TiAl) and α_2 (Ti_3Al) are well known for their strongly ordered nature and the directional bonding of the compounds. The resultant superior thermo-physical properties of these materials include a high melting point of 1460°C, low density, high strength and stiffness, good corrosion, creep, and oxidation resistance, and high ignition resistance when compared with conventional titanium alloys [1-3].

Based mainly upon the outstanding properties mentioned above, there is an ever-increasing demand for the development of titanium aluminide alloys, since these materials are widely recognised as new classes of materials satisfying the advanced design requirements. These proposed design concepts focus on higher service temperatures, lighter weight, and higher operation speeds. As such, titanium aluminides can ultimately find their use in a wide range of components in practical industrial applications [4, 5].

Despite the desirable characteristics of γ-TiAl based alloys, one of the major barriers to their widespread use has been associated with difficulties in processing and the subsequent high costs [6]. Many improvements have been made in the production of γ-TiAl based alloys using conventional casting, ingot forging, powder processing and also new advanced techniques such as sheet production by hot-rolling, laser forming and sintering. Although each of these processes is capable of producing material with acceptable properties, processing costs are still prohibitive for many commercial applications [7, 8]. The future exploitation should be focused on reducing the high manufacturing costs.

Rapid prototyping or additive layer manufacturing (ALM) in a layer-by-layer fashion is an emerging technology for fabricating geometrically complex components to near-net-

shape that are either difficult or impossible to fabricate by other processing methodologies. It also offers a great potential of time and cost savings in comparison to traditional manufacturing technology [9, 10]. In particular, aerospace and automotive components made from materials such as titanium alloys and titanium aluminides that are difficult to manufacture by conventional production processes represent interesting applications for additive manufacturing. Additionally, joining techniques such as fusion welding are one of the most economical and effective methods for both the fabrication and repair of materials, and there have been significant developments in these industrial processes. Therefore, new manufacturing techniques have received an increased interest recently based on the combination of additive manufacturing and welding technology.

1.2 Objectives of Current Research

In the present study, in-situ alloying and additive layer manufacturing based on the gas tungsten arc welding (GTAW) process are combined with separate wire feeding of titanium and aluminium elements to produce titanium aluminide components. The alloy of interest is γ-TiAl, since it is the most widely used titanium aluminide alloy. The general objective is to evaluate the feasibility of the new fabricating technique and to investigate the quality of the as-fabricated wall materials. A number of issues that may be relevant to this purpose are fusion zone solidification, microstructural evolution, defects, residual stress, mechanical behaviour and effect of post weld heat treatment. The specific objectives of this work are as follows:

(1) To study the effect of manufacturing parameters on the characteristics of the as-fabricated materials, and to establish an operational window for obtaining defect-free γ-TiAl based alloy components using the GTAW-based ALM process.

(2) To thoroughly investigate the effect of location on the microstructural features and mechanical properties of GTAW-based ALM produced γ-TiAl alloys.

(3) To characterise the residual stress distribution, microstructural features and mechanical properties of GTAW-based ALM produced γ-TiAl alloys in the as-fabricated and various post production heat-treated conditions.

(4) To build up TiAl-based functionally graded materials (FGMs) using the GTAW-based ALM process, and to preliminarily investigate the achieved microstructural features and microhardness variation as a function of composition gradient.

1.3 Major Contributions of Current Research

This research study concentrates on the relatively rapid and inexpensive GTAW-based ALM method rather than the popular laser or electron beam based ALM techniques. The repeatable and reproducible γ-TiAl walls obtained in this study prove useful in the GTAW-based ALM process of titanium aluminide alloys. The results also provide new insights into the effects of repeated localised thermal cycles on these materials including the microstructural features, physical and mechanical properties that form during the specific process. This is in turn used to optimise GTAW-based ALM technology for functional graded Ti-Al alloys. It is anticipated that the present study can improve the feasibility of GTAW-based ALM approach and promote its development as an industrially viable means of producing structural components with large scale.

In addition, the findings of this study will contribute to an in-depth understanding of additively manufactured intermetallics. Of particular importance is the location dependence of phase evolution and the mechanical performance. This knowledge will be applied to intermetallics and functionally graded alloys fabricated from more complex alloy wires using the GTAW-based ALM systems.

Finally, it is hoped that the successful development of intermetallics and functionally graded alloys through the GTAW-based ALM technique will bring significant technical knowledge and economic benefits for alloy components manufactures and the alloy industry in general.

1.4 Outline of Thesis

This thesis is organised as follows:

A brief literature review is presented in Chapter 2, which describes the current knowledge within the field of titanium aluminide alloys including the basic information of Ti-Al binary system, conventional and novel manufacturing technology (current additive manufacturing processes) and joining methods. This is followed by a brief summary of manufacturing aspects and the existing problems related to titanium aluminides as well as current research in this area.

Chapter 3 introduces the characterisation techniques and the corresponding equipment that have been used in this study.

In Chapter 4, the novel in-situ alloying process using GTAW-based ALM is used to fabricate γ-TiAl alloy walls. The influence of various manufacturing parameters including arc current, wire feed rate ratio and interpass temperature on the γ-TiAl deposits are investigated with respect to microstructure, composition and microhardness.

Further characterisation of the additively manufactured γ-TiAl alloys is presented in Chapter 5 through in-depth investigations of the microstructure evolution and tensile properties at different locations and in different orientations.

Chapter 6 addresses the relationships between various post production heat treatment conditions and the microstructure and tensile properties of additively manufactured γ-

TiAl alloys. The residual stresses within the as-fabricated components and their change after stress relief heat treatment are also evaluated in this chapter.

The versatility of the in-situ alloying GTAW-based ALM process is further examined by fabricating functionally graded Ti-Al alloys. The aspects of composition gradient and its subsequent microstructural features and microhardness properties are presented in Chapter 7.

Chapter 8 provides a summary of the primary findings in this study and makes recommendations relating to future work that would be required in commercial development of additively manufactured γ-TiAl alloys and functionally graded Ti-Al alloys, as well as the GTAW-based ALM process itself.

2 Literature Review

In this chapter, a comprehensive overview of titanium aluminides is introduced, including the basic characteristics, development, manufacturing and joining technology. The intermetallic compounds within γ-TiAl alloys are briefly reviewed, along with an introduction of microstructure and mechanical properties as well as their relationship, and finally the manufacturing techniques. Particular attention is given to additive manufacturing and its application to γ-TiAl alloys.

2.1 Titanium Aluminides

Two-phase titanium aluminide intermetallics are an emerging class of materials in a variety of commercial applications. A fundamental understanding of phase transformation and microstructural evolution is essential to the development of various titanium aluminide alloys. Another critical influence is the inter-relationship between structure and property. A substantial amount of relevant information will be provided in this section.

2.1.1 Constitution of Binary Titanium Aluminides

Several different intermetallic phases that represent superlattice of the terminal solid solutions have been found to exist in titanium aluminides. These compounds have long been known as an attractive basis for lightweight high-temperature materials. Table 2.1 indicates the crystallographic data for all the intermetallic phases [11]. The most of favourable of these compounds are Ti_3Al (α_2) and TiAl (γ), and their properties give them engineering significance.

Ti_3Al (α_2) phase has an Al content between 22 ~ 39 at.% and orders according to $D0_{19}$ structure (Figure 2.1a) with a hexagonal symmetry. It derives from an A_3 type structure

but presents a long-range order only in the direction perpendicular to the c-axis. The α_2-phase forms during cooling by $\beta \rightarrow \alpha \rightarrow \alpha_2$ transformation type, and transforms to disordered hcp structure at a temperature range of 1125 ~ 1150°C [12]. The α_2 phase has been found to exhibit good high temperature strength, but has very low ductility. Along with this, it also has a high rate of oxygen and hydrogen absorption, which in turn leads to further embrittlement at high temperatures [13, 14].

Table 2.1 Al-Ti crystal structure and lattice parameter data [11].

Phase	Composition, at.% Al	Pearson symbol	Space group	Prototype	Lattice parameter, nm
$TiAl_3$ (HT)	74.5-75.0	*tI*8	*I*4/*mmm*	$TiAl_3$	*a* = 0.3849 *c* = 0.8609
$TiAl_3$ (LT)	~75	*tI*32	*I*4/*mmm*	…	*a* = 0.3877 *c* = 3.3828
Ti_5Al_{11}	66-71	(a)	…	…	*a* = 0.3953 *c* = 0.4104(b)
$TiAl_2$	66-67	*tI*24	$I4_1/amd$	$HfGa_2$	*a* = 0.3970 *c* = 2.4309
$Ti_{1-x}Al_{1+x}$	63-65	*tP*4	*P*4/*mmm*	AuCu	*a* = 0.4030 *c* = 0.3955
Ti_3Al_5	62	*tP*32	*P*4/*mbm*	Ti_3Al_5	*a* = 1.1293 *c* = 0.4038
TiAl (γ)	50-62	*tP*4	*P*4/*mmm*	AuCu	*a* = 0.4000 *c* = 0.4075(c)
Ti_3Al (α_2)	~20-39	*hP*8	$P6_3/mmc$	Ni_3Sn	*a* = 0.5782 *c* = 0.4629

(a) Tetragonal. (b) Subcell parameters at 66 at.% Al. (c) at 50 at.% Al.

TiAl (γ) phase exists within a wide composition range, containing 48.5 to 66 at.% Al content. Its $L1_0$ type face-centred tetragonal structure consists of atomic layers perpendicular to the c-axis (Figure 2.1b). Due to the layered arrangement of Ti and Al atoms along the (001) direction the c-axis of the unit cell shows tetragonal distortion

and the c/a ratio for the stoichiometric composition is around 1.02 [15]. The lattice parameters a and c show a linear dependence on Al content and the tetragonal distortion increases with increasing Al content [16]. The γ-TiAl phase can remain ordered up to its melting point of roughly 1450 °C. The γ phase exhibits excellent oxidation resistance and has very low hydrogen absorption, but its room temperature ductility is close to none.

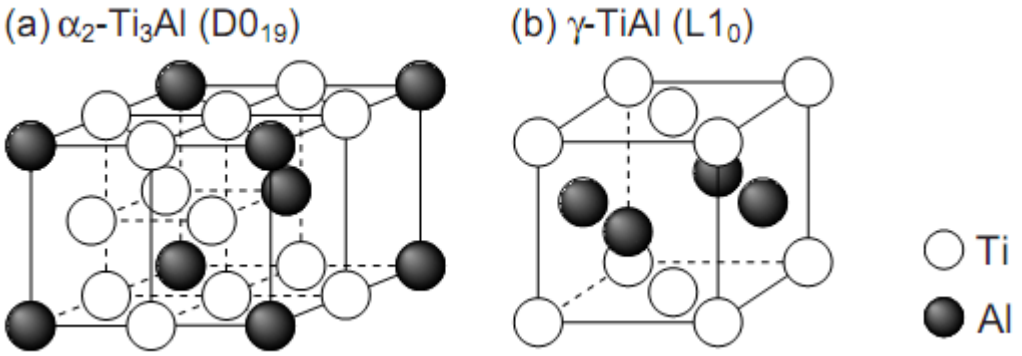

Figure 2.1 Structures of ordered phase in the Ti-Al binary system: (a) α_2-Ti_3Al ($D0_{19}$), and (b) γ-TiAl ($L1_0$) [17].

Conversely, $TiAl_3$ orders according to the $D0_{22}$ structure. This structure is related to two $L1_2$ type unit cells stacked along the c-axis with an antiphase boundary of $\frac{1}{2}[110](001)$ type at every other (001) plane [12]. Compounds such as $TiAl_2$ and Ti_xAl_y reported by Braun and Ellner [18] and Inui and Yamaguchi [19] do not exhibit good mechanical characteristics for industrial applications.

2.1.2 Phase Transformations and Microstructures

According to the binary Ti-Al phase diagram (Figure 2.2) [20], the TiAl-based alloys that correspond to an Al concentration between 35 ~ 65 at.% consist either of a mixture of γ and α_2 phases or of a single γ phase. However, the microstructure of pure γ phase with more than 50 at.% Al content is characterised by equiaxed γ grains exhibiting no ductility. Even after microstructural refinement and small alloy additions this alloy composition shows very little improvement in ductility [21]. Therefore, the dual phase

of titanium aluminide with a mixture of α_2 and γ phase existing between 37 at.% and 49 at.% Al content has been considered to be a more significant engineering alloy for several structural applications [22-24]. As shown in the central part of the binary Ti-Al phase diagram (Figure 2.3 [25]), the equilibrium phases in this concentration range are: the disordered solution phases liquid, hcp α-Ti, bcc β-Ti, and the ordered intermetallic compounds γ-TiAl and α_2-Ti_3Al. The Al content directly determines the solidification microstructure of these alloys.

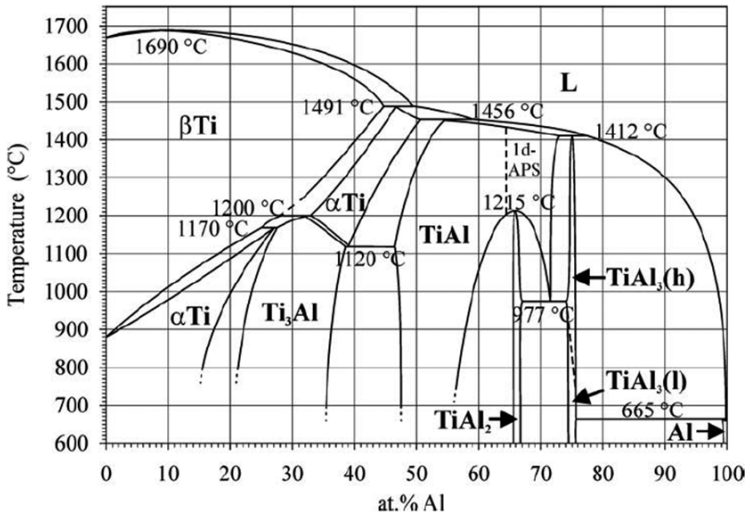

Figure 2.2 Binary phase diagram of Ti-Al system [20].

The alloys containing less than 45 at.% Al always solidify through the single β phase, while the solidification of alloys with Al concentrations of 45~49 at.% can be completed by peritectic formation of the α phase from primary β dendrites. The solidification path is as follows: L → [β]/[β+α]+L → β+α → α → α+γ → α_2+γ. On cooling, the β phase becomes unstable and transforms into the α phase. With further solid state cooling, the α phase becomes unstable and orders into the α_2 phase at around 1117°C. Stacking faults are produced by this ordering reaction on the basal plane with many antiphase boundaries. The γ phase then nucleates and grows (α → α_2+SF (stacking faults) → α_2+γ) from these faults following the orientation relationship $(0001)_{\alpha_2} \parallel \{111\}_{\gamma}$ and $\langle 11\bar{2}0\rangle_{\alpha_2} \parallel \langle 1\bar{1}0\rangle_{\gamma}$ [26, 27].

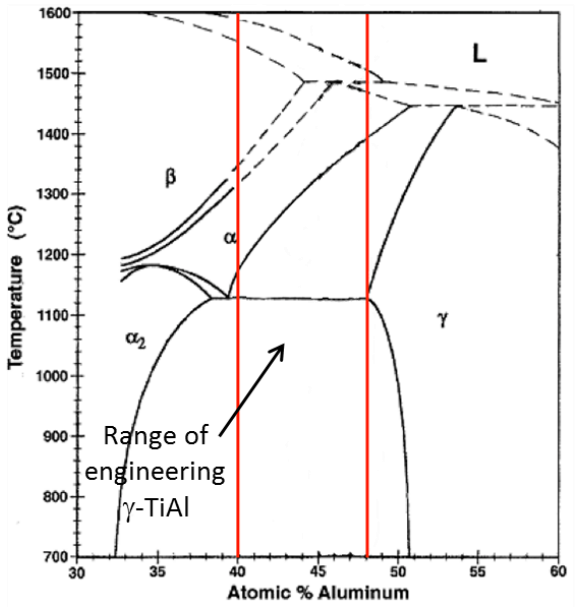

Figure 2.3 Central part of the binary Ti-Al phase diagram [25].

However, a variety of different solid state phase transformation can occur during cooling from high-temperatures depending on the thermo-mechanical processing route and conditions, and hence a range of microstructural morphologies can be obtained. For instance, during casting or ingot processing, the peritectic reaction based solidification often results in macroscopic columnar grains and a pronounced microsegregation of the alloying elements [28]. In general, the wide range of microstructures are classified into four categories, namely near-gamma, duplex, nearly-lamellar, and fully lamellar as shown in Figure 2.4 [29, 30].

The near-gamma microstructure (Figure 2.4a) is formed when the material is heat-treated in the $\alpha_2+\gamma$ phase field. Heat-treatment in this phase field results in the coarsening of the existing γ grains. The microstructure is characterised by coarse gamma grain regions with fine γ grain stringer regions containing dispersed α_2 particles.

The duplex microstructure (Figure 2.4b) is a mixture of fine fully lamellar colonies and equiaxed γ grains. It forms when heating temperature is in the $\alpha+\gamma$ phase field where the α/γ phase volume ratio is equal to 1. A very fine duplex microstructure can form with an average grain size in the order of 10 μm. Due to the very fine grain size, the duplex

microstructure exhibits the best ductility and strength at room temperature, but at higher temperatures creep and fatigue resistance is very low.

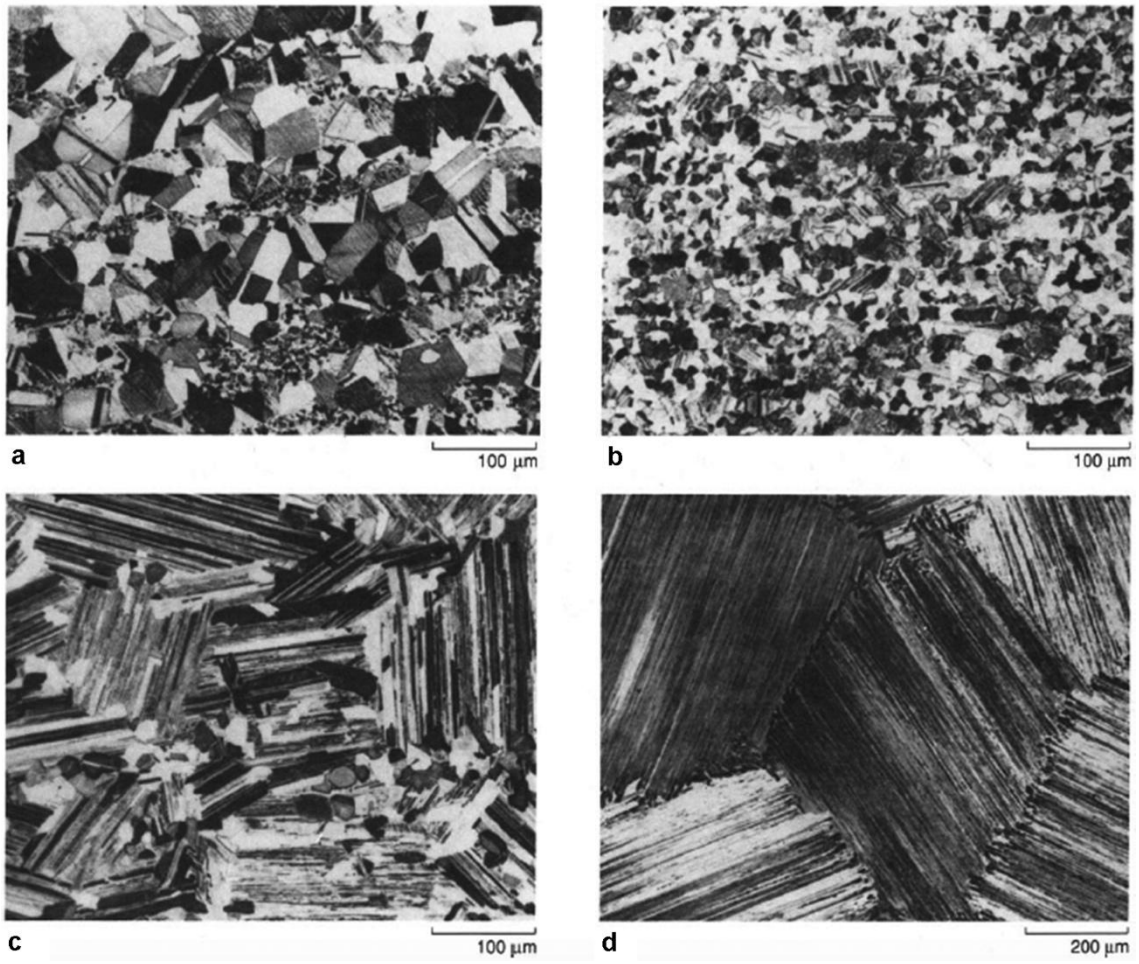

Figure 2.4 Microstructure types in dual phase titanium aluminides: (a) fully lamellar, (b) duplex, (c) nearly lamellar and (d) near gamma [29, 30].

The fully lamellar morphology consists of alternating α_2 and γ plates. The formation of this microstructure always occurs upon slow cooling from temperatures in the pure α phase field to room temperature (Figure 2.4c). In addition, the intermediate cooling rates can lead to the formation of Widmanstätten lath colonies and feathery structures as shown in Figure 2.5 [31]. Widmanstätten colonies (Figure 2.5a) are packets of parallel $\alpha_2 + \gamma$ lamellae inside lamellar colonies and have a different interface orientation to the surrounding lamellae [32]. The feathery structures (Figure 2.5b) resemble lamellar structures and have the usual crystallographic-orientation relationship between the

phases, but are misoriented by less than around 15° with respect to the surrounding colony [33]. It usually has excellent creep and fatigue resistance properties but low ductility and strength due to the coarse grains in the range of 200 to 1000 μm.

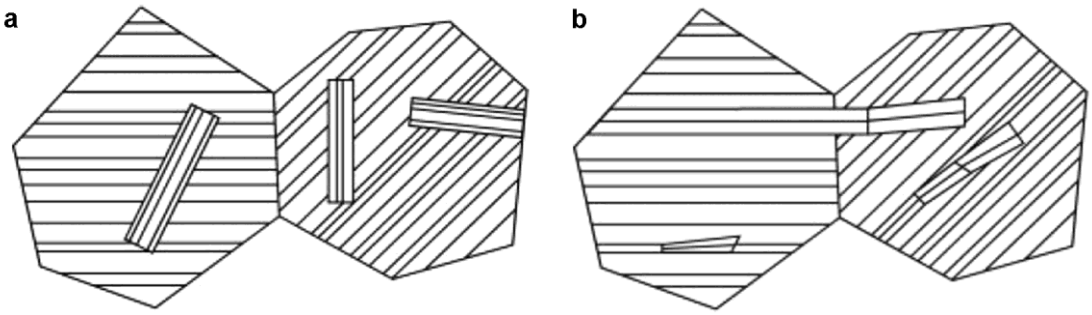

Figure 2.5 Schematic illustration of the morphology of lamellar microstructure with characteristic alternations: (a) Widmanstätten colonies, and (b) feathery structure [32].

The nearly lamellar microstructure (Figure 2.4d) forms at an intermediate temperature between that of fully lamellar and duplex. It is characterized by a majority of lamellar colonies with some equiaxed γ grains.

Of these microstructures, the duplex and fully lamellar microstructure have exhibited mechanical properties conducive for a range of commercial applications [34]. Hence, over the past decades, the development of gamma titanium aluminides has been geared towards development of microstructures having the best features of duplex and fully lamellar microstructure properties [35, 36].

2.1.3 Mechanical Properties

Titanium aluminide alloys display attractive properties such as low density, high elastic moduli, low diffusion coefficient, good structural stability, and good resistance against both oxidation and corrosion (Table 2.2 [31]). As discussed earlier, due to the long-range order of intermetallics, titanium aluminides lack room temperature ductility and fracture toughness. Fatigue crack growth rates are also an area of concern [37], therefore, these alloys must possess a good balance of various low and high temperature mechanical properties for technical applications. In the past, the appealing

properties of titanium aluminides were outweighed by their difficulties in processing and machining at room temperature.

Table 2.2 Properties of titanium alloys, titanium aluminides and superalloys [31].

Property	Ti-Base	Ti_3Al-Base	TiAl-Base	Superalloys
Structure	hcp/bcc	$D0_{19}$	$L1_0$	fcc/$L1_2$
Density (g/cm^{-3})	4.5	4.1-4.7	3.7-3.9	7.9-8.5
Modulus (GPa)	95-115	110-145	160-180	206
Yield Strength (MPa)	380-1150	700-990	350-600	800-1200
Tensile Strength (MPa)	480-1200	800-1140	440-700	1250-1450
Room-temp. Ductility (%)	10-25	2-10	1-4	3-25
High-temp. Ductility (%/°C)	12-50	12-20/660	10-600/870	20-80/870
Room-Temp. Fracture Toughness (MPa$\sqrt{m}$)	12-50	13-30	12-35	30-100
Creep Limit (°C)	600	750	750*-950†	800-1090
Oxidation (°C)	600	650	800‡-950§	870-1090

* Duplex microstructures. † Fully-lamellar microstructures. ‡ Uncoated. § Coated/Actively cooled.

2.1.3.1 Deformation Mechanism

It is well known that titanium aluminides are quite brittle materials and exhibit typical deformation behaviour of intermetallics including lack of ductility (1~3 % at room temperature), strong plastic anisotropy, anomalous increase of the yield stress with temperature, complex slip geometry and break-down of Schmid's law [38]. These attributes can be determined by the dislocation cores and the kinematics of dislocation propagation.

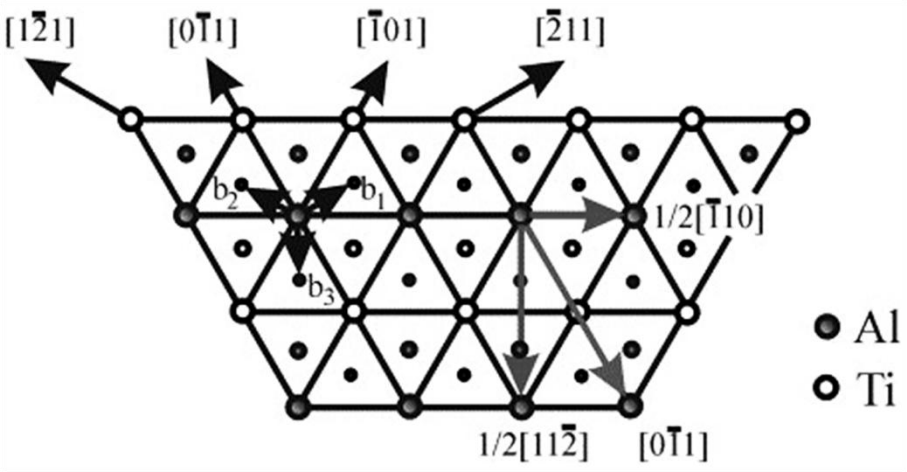

Figure 2.6 Potential slip and twinning systems of the $L1_0$ structure, schematic drawing of a three-layer sequence of atom stacking on the (111) plane shown by small, medium and large circles [39, 40].

The deformation phenomena in two-phase γ-TiAl based alloys are often governed by the γ phase. As such, the slip planes in the $L1_0$ structure that has a close relationship with the face-centred cubic lattice play a key role in the deformation modes of the engineering γ-TiAl alloys [41, 42]. The controlling deformation systems in the γ phase are recognised as ordinary dislocations with Burgers vector $\frac{1}{2}\langle 110]$, ordered twinning of the type $\frac{1}{6}\langle 11\bar{2}]\{111\}$ and superdislocations with Burgers vectors $\langle 101]$, all operating on the close-packed $\{111\}$ planes, as shown in Figure 2.6 [39, 40]. Instead, the glide elements of α_2 phase are determined by the hexagonal ordered $D0_{19}$ crystal structure. Their deformation is primarily provided by the two types of superdislocations $\frac{1}{3}\langle 11\bar{2}0\rangle$ gliding on the $\{10\bar{1}0\}$ prism planes or the basal plane $\{0001\}$ and $\frac{1}{3}\langle\bar{1}2\bar{1}6\rangle$ gliding on the pyramidal planes $\{1\bar{2}11\}$. The decomposition of $\frac{1}{3}\langle 11\bar{2}0\rangle$ superdislocation into superpartials is much easier on the prism plane than on the basal plane due to the lower APB energy on the prism plane [43, 44]. The $\frac{1}{3}\langle\bar{1}2\bar{1}6\rangle\{1\bar{2}11\}$ pyramidal slip system shows a similar mechanism and its decomposition may lead to pinning [45, 46]. Accordingly, a large amount of tensile elongation can be produced by prismatic slip but a limited amount of ductility is present in basal plane slip [47]. As such, the lack of

independent slip systems is thought to be a contributing factor for the brittleness of the two-phase γ-TiAl based alloys [48]. It has been established that the effect of α_2 phase in the two-phase alloys is to improve the purity of γ phase by gettering the interstitial impurities [49, 50]. As a consequence, the glide of $\frac{1}{2}\langle 110]$ ordinary dislocations is the dominant deformation mode, followed by mechanical twinning that is primarily caused by the presence of lamellar structure [31, 51].

2.1.3.2 Tensile Properties

In general, the chemical composition, a well-controlled manufacturing process and the post production heat treatment procedures are considered as key factors that influence the microstructure and thereby achieve the required properties for the envisaged application. Engineering alloys of technical interest contain between 43 and 48 at.% Al, together with other alloying additions. This is mainly due to the fact that the ductility of dual phase alloys increases with an increase in Al concentration up to 48 at.% and then decreases with a further increase in Al concentration beyond 50 at.% [21, 52]. In general, a reduction in Al content tends to increase the strength level, but reduces ductility and oxidation resistance.

It is now accepted that technical alloys should contain both the γ and α_2 phases so that dislocations at phase boundaries can contribute to deformation and oxygen within the γ phase can be scavenged by the α / α_2 phase. In binary alloys, the Al level determines the initial phase to precipitate on solidification and the subsequent phase transformations. For a given alloy, properties are very dependent on microstructure, and microstructure is strongly sensitive to composition. Figure 2.7 shows the sensitivity of mechanical properties to microstructural features of titanium aluminides [53]. The better room temperature ductility and strength are found to appear in the fine grained duplex microstructure and equiaxed structures than fully lamellar microstructure. Yet, the desirable high temperature properties such as creep and fatigue resistance are obtained

with the fully lamellar structure. The nearly-γ structure has been demonstrated to have the highest ductility at room temperature as a result of the high volume fraction of the γ grain despite having a coarser grain size than the duplex structure [54].

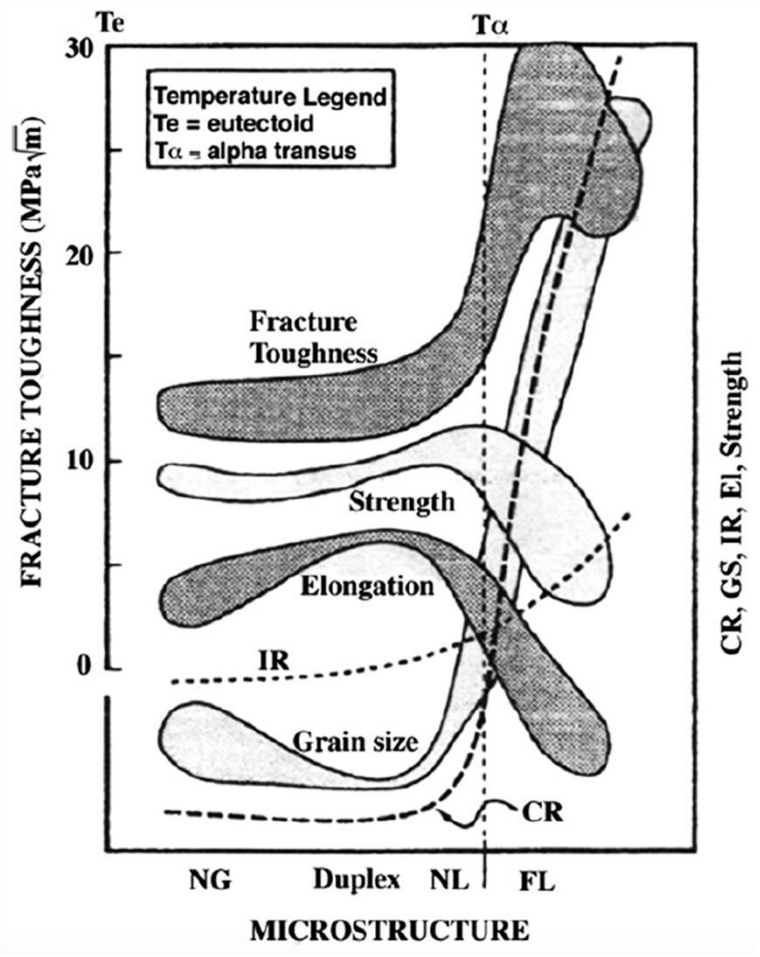

Figure 2.7 Microstructure-properties relationships in titanium aluminides [53].

The tensile properties and their relationship with microstructural characteristics of the two-phase titanium aluminides can be interpreted in terms of the Hall–Petch equation [55]:

$$\sigma_y = \sigma_{0,y} + k_y d^{-1/2} \qquad \text{Eq. 2.1}$$

Here σ_y is the yield strength, $\sigma_{0,y}$ is a measure of the lattice frictional stress, k_y is a dislocation unpinning parameter and d is the average grain diameter.

It has been demonstrated that colony size, interlamellar spacings, and alloy addition are three interrelated factors that affect the mechanical properties of the TiAl alloys with fully lamellar structures [56]. The poor room temperature tensile strength and ductility of fully lamellar microstructures compared to that of fine-grained duplex microstructure are principally due to their coarse grain size. Therefore, the room temperature tensile properties can be improved by reducing the colony size and lamellar spacing.

The tensile properties of dual phase γ-TiAl alloys are also dependent on the test temperature. There is a clear brittle to ductile transition temperature (BDTT) range of 700 ~ 800 °C, which is related to the alloy composition and microstructural features. The tensile strength increases as temperature goes up to the BDTT and then decreases with a further increase of temperature. Conversely, the ductility increases slightly when the test temperature increases to the BDTT, while it shows a significant increase beyond the BDTT owing to the increased activities of twinning and ordinary dislocations [57].

2.1.4 Applications

Gamma titanium aluminides have attracted significant attention in a variety of automotive and aerospace applications. The purpose in these applications is to substitute the heavier conventional titanium, nickel or iron-based superalloys in certain ranges of stress and temperature.

In the field of automotive applications, the γ-TiAl alloys offer interesting possibilities due to their high heat resistance, low density and high thermal conductivity. The major uses of these intermetallic alloys are in turbine rotors, blades of turbochargers and exhaust valves [58]. The first commercial use of γ-TiAl alloys has been in high performance turbochargers for sports cars in 1999 [59]. Also, it has been demonstrated that improved power output and reduced fuel consumption are achieved for automotive reciprocating engines where certain components made with titanium aluminide have been substituted for those using traditional materials [60, 61]. However, the long-term

use of titanium aluminides in such applications will be primarily determined by the availability of alternative cost-effective manufacturing technologies.

The aerospace sector appears to be another suitable application for titanium aluminide intermetallics. The first major aerospace applications of γ-TiAl alloys have been focused on the development of aero-engine craft. Traditionally, aero-engine components operating above 600 °C have used steel or nickel-based alloys. These much heavier alloys are not able to meet the requirements involving higher trust to weight ratios, fewer compressor and turbine stages, and increased turbine entry temperatures [62]. In order to achieve these targets, much work has concerned titanium intermetallic systems. Their low density and good resistance to temperature promote the development of γ-TiAl alloys for rotating components in turbine engines [12]. Also, a significant amount of time and effort have been spent in developing low-pressure and high-pressure turbine blades with γ-TiAl alloys for aircraft engines [63-66]. The corresponding qualification and certification procedures have been successfully completed. Because of this achievement, the utilisation of titanium aluminide intermetallics can dramatically expand in aero-engines. The γ-TiAl alloys also have fascinating potential for a number of exotic aerospace applications. Components made from titanium aluminides can effectively reduce the exhaust and noise pollution as well as increase the failure strength in supersonic high-speed civilian transport system, for instance, hypersonic planes and space vehicles [67].

2.2 Manufacturing of Titanium Aluminides

Industrial scale processing routes that have been used to produce γ-TiAl alloy billets and components include investment casting, ingot or powder metallurgy. In most aspects these techniques are the same as those used to produce conventional titanium and nickel-based alloys [28]. Figure 2.8 indicates a flowchart of typical processing methods

for titanium aluminides [68]. As can be seen from this flowchart, for the case of TiAl alloys these processes often require a series of additional post-processing steps such as hot-isostatic pressing, ageing, annealing, and hot working to improve the mechanical properties to desirable levels and to obtain the desired component geometries. For casting and ingot metallurgy processes, the main difficulties encountered in producing γ-TiAl are the development of cracks, inhomogeneous microstructure and coarse-grained microstructure, resulting in poor mechanical properties. For example, casting defects and strong segregation of impurity elements are found in titanium aluminides produced by various casting method [69]. Bryant and Semiatin [70] have pointed out that microsegregation is an obvious phenomenon in multicomponent ingot-metallurgy titanium aluminides as well as in binary alloys. Powder metallurgy minimises these problems, but introduces the likelihood of porosity and contamination [71]. Although post-processing operations can solve many of the problems associated with the three main processes, and each manufacturing route can produce acceptable material, the overall production costs are inevitably increased. High costs especially due to the post processing steps after ingot production or powder consolidation have, in most cases so far, outweighed the benefits of high performance and weight savings in the final application [72].

In order to reduce the post-processing steps and their costs, titanium aluminide components with desired mechanical properties and complex shapes have been successfully formed using several advanced techniques such as direct rolling, laser forming, and spark plasma sintering. Reduced production time is the major advantage of these techniques compared to the traditional methods, while the main drawbacks are porosity and limited scalability [73].

Therefore, novel manufacturing methods are required to have the potential to substantially reduce the manufacturing costs and simultaneously increase the material productivity (the “fly-to-buy-ratio” in the aerospace sector). As such, near net-shape

techniques have received greater attention in a combination of casting, welding, super-plastic forming, diffusion bonding and powder metallurgy.

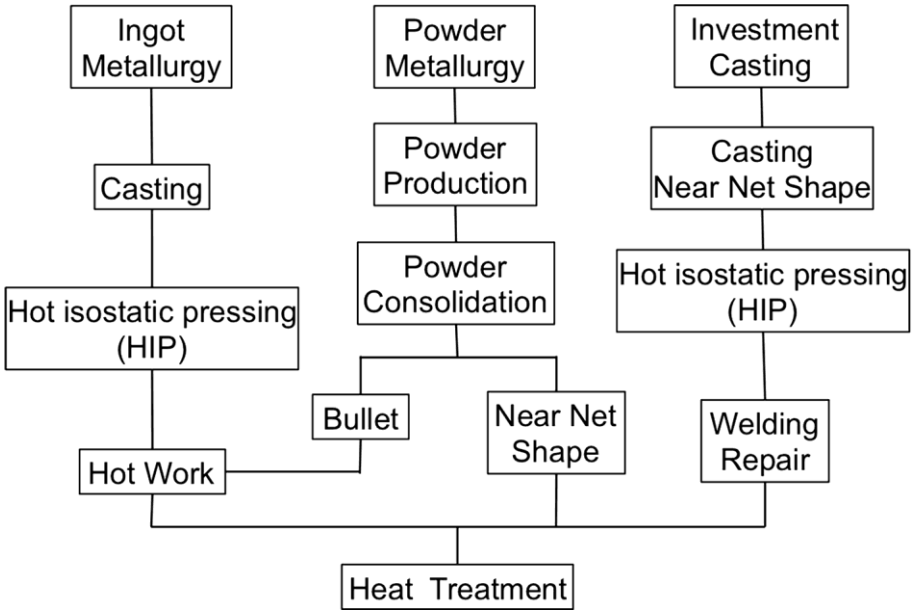

Figure 2.8 A flowchart of typical processing method for titanium aluminides [68].

2.2.1 Ingot Metallurgy and Casting

Conventional ingot metallurgy (IM) has successfully utilised three principal melting techniques involving induction skull melting (ISM), vacuum arc melting (VAR) and plasma arc melting (PAM) [74, 75]. The TiAl ingots can be produced by the arc melting of a consumable electrode acting as the negative pole of the arc in a high vacuum environment. The positive pole of the arc is a water-cooled copper mold that contains the molten metal and does not contaminate the ingot [31].

It has been well documented that the main problems encountered when applying ingot metallurgy to titanium aluminide alloys are the development of cracks and the presence of dendritic, inhomogeneous and coarse-grained microstructure [76-78]. Hence, post production steps are necessary to produce titanium aluminide parts with desirable microstructural features and the required mechanical properties. For example, Figure 2.9 illustrates the necessary post production routes for producing a TiAl compressor blade [53].

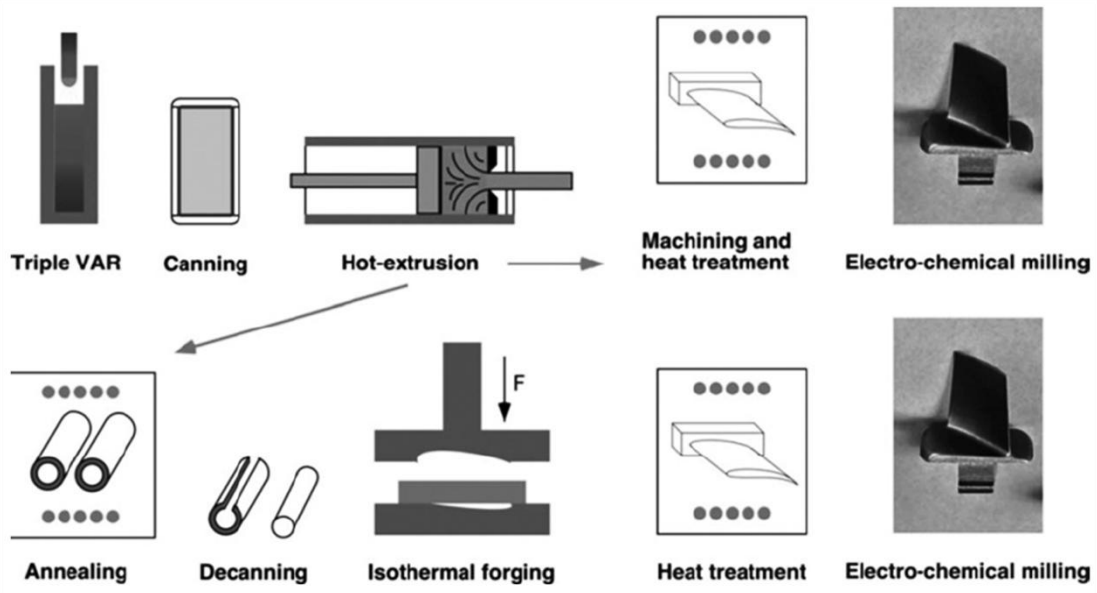

Figure 2.9 Processing routes required for the production of high-pressure aero engine compress or blades from a TiAl ingot [53].

The titanium aluminide ingots and castings are necessarily subjected to several thermo-mechanical routes such as hot rolling, isothermal forging, and hot extrusion in order to achieve the designed component shape that is free of impurities. The residual stresses inside the components can be relieved by further heat treatments. In addition to these thermo-mechanical treatments, hot isostatic pressing (HIP) and the associated dynamic recrystallisation have also been applied on the ingots and castings to improve chemical homogeneity and refine microstructure [4, 79].

2.2.2 Powder Metallurgy

Powder metallurgy (PM) is a widely used technique to produce complex components. This technique loads the metal powders into a die to form compacts at approximately room temperature, which are then placed inside a furnace. A near-net shape component with adequate mechanical properties can be achieved by sintering of the powder particles under a protective atmosphere at a temperature below the melting point of the material in order to maintain the required compact shape [80].

Two essential approaches named as prealloyed and elemental powder technologies have been applied to produce titanium aluminide components. The powder-metallurgical production of titanium aluminide parts is usually accomplished with the help of rapid solidification methods and the compaction of these powders to the final component by hot isostatic pressing (HIP). Hot isostatic pressing (HIP) of powder compacts is a very popular powder metallurgy based method to produce TiAl billets [81-84]. In addition, secondary processing such as hot rolling or superplastic forming is necessary to achieve suitable properties for different applications [85].

The primary advantage of powder metallurgy is lower overall production cost due to little machining. Thus, near-net shape titanium aluminide components can be made on an economical basis with high quality and minimal waste. Further, powder metallurgy can overcome many of the problems associated with ingot metallurgy, such as centerline porosity, chemical inhomogeneity, regions of varying density and microstructure [86]. Besides, new alloys that cannot be made by conventional ingot metallurgy can receive considerable development through powder metallurgy.

However, there are still some disadvantages. The presence of impurities in the powders in the form of interstitial elements leads to porosity in the final product [87]. To overcome this potential problem, high purity TiAl powders have been successfully produced by gas atomization process, but the cost of raw materials is increased significantly. Another problem associated with powder metallurgy is the limited flexibility in hot isostatic pressing to control the grain size of the final part.

2.2.3 Additive Layer Manufacturing

Additive manufacturing (AM) or 3D printing is an emerging process for joining materials to make objects from 3D model data. As opposed to traditional subtractive manufacturing methodologies, components can be economically produced by progressive consolidation of raw materials, such as powder or wire, in a layer-by-layer

manner with this additive approach [88]. This innovative technology is becoming a cost-effective competitor to machining and forming technologies and has been proven to be very effective in building up complex geometries layer by layer, and so is often referred to as additive layer manufacturing (ALM). There are many terms commonly used for AM, such as solid free form fabrication (SFF), rapid manufacturing (RM), 3D printing (3DP), and so forth, but they all have the origins of rapid prototyping [89]. An overview of the different additive manufacturing processes is shown in Figure 2.10 [90]. These technologies were first created to produce pre-production design models, but they have expanded since then.

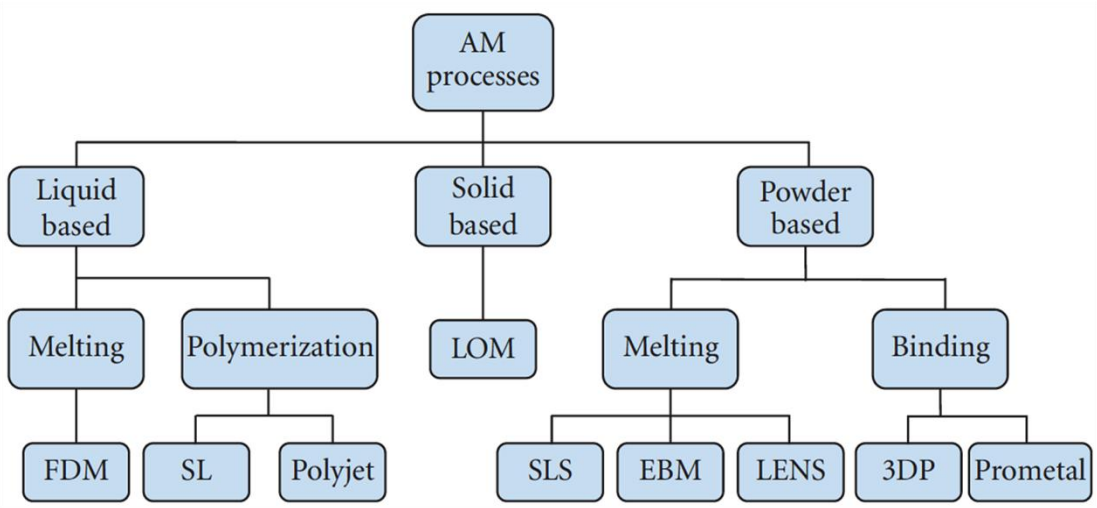

Figure 2.10 Three-dimensional printing processes [90].

Rapid prototyping (RP) was introduced first in 1980's [91]. As one of the earlier ALM processes, 3D objects has been successfully produced by RP technology using computer-aided design (CAD). The product development with this process shows major advances involving the time and cost reduction, human interaction, and consequently the product development cycle [92]. In addition, it is possible to produce components with complex shapes that would be extremely difficult to machine.

Not all commonly manufactured components can be produced by the RP process even though many metals and ceramics can be successfully printed [93]. The part size is still

limited. In some cases, components with larger dimension are not able to be produced by currently available additive manufacturing equipment.

Nevertheless, additive manufacturing is a rapidly growing technology due to several advantages. The manufacturing costs and required time can be effectively reduced by using AM process. This promising technique can also provide an economical way to produce unique products at low volumes. Also, the environmental and ecological potential of AM process leads to light-weight components on demand with optimised designs by using less raw material, creating less waste material and eliminating hard tooling.

2.2.3.1 Metal Additive Layer Manufacturing

Metal additive layer manufacturing (ALM) has experienced extensive development and found enormous attractions over the past decade [94]. A heat source, such as laser, electron beam or welding arc, is focused on a substrate to create a melt pool following a designed moving path. The melted raw materials (powder or wire) can be progressively consolidated to form the final components in a layer-by-layer manner as represented schematically in Figure 2.11 [95].

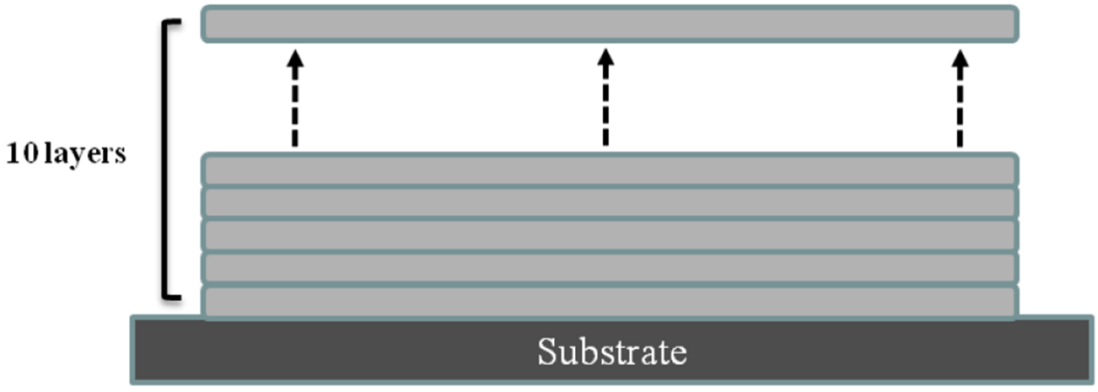

Figure 2.11 ALM multilayer procedure consisting of 10 layers of Ti-6Al-4V deposited on a substrate of the same material [95].

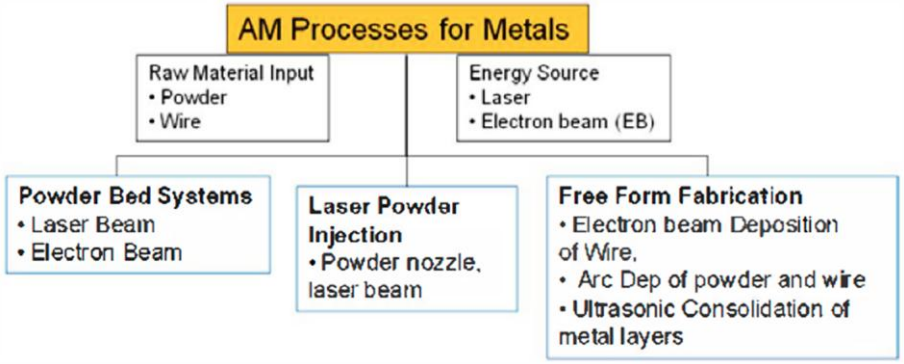

Figure 2.12 Metal additive manufacturing processes [96, 97].

ALM systems that produce metal parts can be divided into three broad groups: powder-bed systems, laser powder injection and free-form fabrication, as shown in Figure 2.12 [96, 97]. The first group consists of systems that use a laser or electron beam to heat powder to melt and form parts [98, 99]. All of the systems in this group produce parts in a powder bed, meaning that the parts being fabricated are entirely surrounded by unused powder when the build process is complete. The second group of metal-based ALM systems is laser powder injection system, where the powder is fed through a nozzle and laser beam melts the powder at the point where it crosses the beam path. It is capable of producing functionally graded materials with automated dispensing control of multiple materials [100], and does not require a powder bed. The third group is the freeform fabrication ALM processes including electron beam deposition of metal wire [101], ultrasonic consolidation of metal layers [102], and arc deposition of powder and wire [103, 104].

During fabrication, the energy source and type of raw material are two key process elements required to form the components. The most commonly used heat source in current ALM systems is laser or electron beam. Laser-based systems are capable of producing a surface finish that is as good as or better than a sand-cast finish, although not as good as a finish-machined component. In addition, fine feature details can also be obtained in the components built by laser systems. Electron beam systems are many times faster than laser-based systems despite somewhat more expensive equipment.

Superior mechanical properties and lower distortion can be achieved by electron beam systems. The surface finish and feature detail have significantly improved in recent years but is not yet able to match the capabilities of laser systems [105].

With respect to the input materials for ALM technology, many of the powder based systems use powder recycling and are prone to high impurity levels in the output materials [106]. Wire-based techniques can overcome many of the problems of powder-based techniques. It has been demonstrated that the wire-feed processes are more economical and less susceptible to contamination from the atmosphere in comparison to processes using powders [107]. Also, the deposition rates of wire-feed systems can be more than ten times higher, and there is almost no limitation regarding the size of the component that can be built, provided the manipulator is sufficiently large and appropriate inert gas shielding can be maintained around the melting zone or other areas at critically high temperatures [108].

However, less attention has been paid to wire-feed processes in comparison to powder-bed or powder-feed (also: blown-powder) processes in the last decades. The increasing market demand has promoted wire-feed processes in recent years [109, 110]. Mostly for these reasons, it may be prudent to focus research activities on relevant issues for wire-based processes involving repeatability, material properties, material usage, possible part size, and building speed.

2.2.3.2 Applications

The AM technology has matured significantly from its development years in the late 1990s. Now the innovative technology has been welcomed in many industrial sectors such as biomedical, aerospace, automotive and tooling, due to the obvious advantages in product customisation, maximum material savings, and gradual and controlled porous structures [111]. Additive manufacturing in combination with imaging technology is transforming the practice of medicine; it is now possible to have a precise model of a

body part and implant before surgery, increasing the likelihood of a successful procedure despite its complexity [112]. Additive manufacturing simplifies the design process across a wide range of disciplines such as civil engineering and architecture, as 3D scaled models complex civil projects can be quickly and economically produced [113]. The application of additive layer manufacturing in the automotive industry is useful for modelling of new components, or small-volume reproduction of obsolete parts. Aerospace and automotive components made from materials such as titanium alloys and titanium aluminides that are difficult to manufacture by conventional production processes represent particularly interesting applications for additive manufacturing. In the aerospace industry, additive layer manufacturing is advantageous in reducing the buy-to-fly ratio, reducing wastage and processing time, saving energy and giving more flexibility of complex parts that would be difficult to achieve using conventional machining processes [114].

Numerous ALM processes have been successfully established for conventional metals, including aluminium [115, 116], nickel [117, 118], steel [108] and titanium [97, 119]. Among them, considerable production-related studies have been conducted on ALM processes applied to titanium alloys, particularly on Ti-6Al-4V. Several investigators have assessed the build rate, surface quality, overall deposition accuracy, level of impurities, post-processing treatment such as hot isostatic processing, heat treatment, extent of machining, and cost, compared to conventional subtractive processes. Kelly and Kampe [120, 121] have investigated the microstructural characterization and thermal history in laser additive manufactured Ti-6Al-4V builds, respectively. The resultant microstructure consisted of a periodic, scale-graded layer of basketweave Widmanstätten α and a banding that consisted of colony Widmanstätten α. Also, a numerical model has been developed to study the effect of process parameters on the thermal-profile characteristic. The constructed model has been used to develop a microstructure-evolution map to qualitatively determine the equilibrium and non-equilibrium transformations during laser additive manufacturing. Mok et al. [122, 123]

have assessed the microstructure and mechanical properites of Ti-6Al-4V walls produced with the high powered diode laser additive manufacturing process. The investigations demonstrated that the wire-fed deposition process was able to provide a high deposition rate with good quality. Baufeld et al. [124] compared the microstructure and mechanical properties of Ti-6Al-4V components fabricated by laser-beam deposition and shaped metal deposition with GTAW. Both techniques were shown to have high deposition rate and the capability to produce ALM components with excellent mechanical properties. Martina et al. [106] studied the benefits of plasma wire depostion for the additive layer manufacture of Ti-6Al-4V. They also established regression models capable of predicting the main geometric features of the deposited ALM walls. All the results showed the feasibility of using plasma wire deposition for ALM of large aerospace structural components. In Brandl et al. [125] the elementary properties of wire-fed additive layer manufactured T-6Al-4V material in correlation to process parameters and heat treatments were discussed comprehensively. However, the reason of hardness variation with post heat treatment could not be determined from the current results and has to be verified by further experiments. Additionally, Wang et al. [126] utilised wire and arc additive manufacture out-of-chamber deposition technology to successfully fabricate large near-net shape Ti-6Al-4V components and investigated their microstructure, tensile and fatigue properties. The averaged yield and ultimate tensile strengths of the as-deposited material were found to be slightly lower than those for a forged Ti-6Al-4V bar, while the ductility was similar and the mean fatigue life was significantly higher when porosity that caused by contamination of the wire was avoided. Therefore, it is necessary to minimise wire contamination in order to implement wire and arc ALM in the aerospace industry.

However, the application of ALM to intermetallics such as titanium aluminide has been limited to laser melting- and electron beam melting-based techniques. D Srivastava [127, 128] applied direct laser fabrication to fabricate TiAl alloy components using gas

atomised TiAl powders. The range of processing parameters was identified and controlled by an intelligent feedback system. The authors also established the relationship of processing parameters and the subsequent heat treatment with the microstructure and mechanical properties. Nevertheless, large extent of thermal cracking was found in the as-fabricated component and the quality of surface finish should be improved. Laser melting deposition (LMD) ALM has been used to produce TiAl intermetallics and the resultant microstructure and mechanical properties were analysed in detail [129]. In comparison to the conventional routes, LMD processed specimen showed smaller grain size and higher ultimate tensile strength but very low ductility due to the fully lamellar microstructure. The effects of heat treatment have also been evaluated [130]. Uniform microstructure was obtained after annealing at certain conditions for as-fabricated alloys with different composition. The room-temperature strength was improved after heat treatment, while the ductility was still very low. The first successful application of electron beam melting (EBM) on fabricating TiAl components has been reported to consolidate Ti-47Al-2Cr-2Nb powders [131]. Two EBM processing routes of prealloyed TiAl powders have also been explored to successfully produce near net shape parts, while the processing conditions should be adjusted to reduce vaporisation and achieve the desired γ-TiAl phase [6]. Furthermore, Murr et al. [132] have demonstrated the potential to build near net shape and complex titanium aluminide products directly using powder-bed electron beam melting (EBM) technology for aerospace and automotive applications. However, non-optimised build parameters leaded to some regions of residual porosity in the EBM-fabricated titanium aluminide alloys. Biamino et al. [133] recently succeeded in producing γ-TiAl based alloy with low levels of internal defects and consistent tensile properties by using powder-bed EBM. The as-fabricated titanium aluminide part exhibited fine and homogeneous microstructure as well as very low residual microporosity after hot isostatically pressing. Therefore, the improvement of current techniques and the

development of new processes with high level of precision play an important role in making ALM systems faster and more productive.

2.3 Joining Techniques for γ-TiAl Alloys

As demonstrated in the previous section, titanium aluminides are valuable structural materials in the aerospace, automotive and power generation industries due to their superior properties at elevated temperature such as high specific strength and modulus [134]. In order to achieve effective industrial utilisation, γ-TiAl alloys have attracted a great deal of research interest in methods for joining of these alloys together, and also the joining to other related materials. To cover this range of joining requirements, a diverse set of techniques are needed. Solid-state joining, brazing and fusion welding processes will be described in the following sections.

2.3.1 Solid State Welding

Several specialised solid state welding processes have been reported to obtain joints between titanium and aluminium as well as titanium alumindes and themselves. Friction stir welding, as a press welding method, have been used to produce a lap joint of titanium and aluminium with free defect and considerable mechanical property [135, 136]. The effect of heat treatment on the interlayer of friction weld joint has been investigated by Fuji [137]. Sound γ-TiAl welds with good high-temperature strength have also been obtained by friction stir welding [138].

Another effective solid joining method is diffusion bonding. This technique has been reported to successfully join commercially pure Al and pure Ti [139]. Also, diffusion bonding is a suitable process for titanium aluminides. Defect free titanium aluminide bonds has been achieved by diffusion bonding at different temperature ranges and using different bonding pressures [140, 141]. Heat treatment has also been performed to improve the mechanical properties of the bonds.

2.3.2 Brazing Techniques

Brazing is the bonding of metal that occurs when a high-temperature filler is allowed to melt and flow into a joint by capillary action before the filler solidifies [142]. For reactive metals such as titanium and aluminium, brazing processes are usually conducted in a vacuum or inert gas atmosphere to prevent surface oxidation during heating [143].

Since brazing does not impose severe stresses on the weld, this technique has received special attentions in joining TiAl alloys to themselves or to other materials. Infrared brazing was utilised by Shiue et al. [144, 145] to join TiAl alloys with pure Ag, BAg-8 and BAlSi-4 brazing alloys. The interfacial microstructural evolution, joints properties and reaction kinetics were comprehensively evaluated. Ti–Ni–Cu brazing alloys were used by Wallis et al. [146] to braze TiAl alloys. High-quality brazed joints with good room temperature and high-temperature properties were obtained.

2.3.3 Laser and Electron Beam Fusion Welding

Although solid state welding processes and brazing techniques can produce successful titanium aluminide joints, some problems such as ultimate joint strength, long joining time, high cost of equipment and restricted component dimensions have limited the application of these methods. Hence, fusion welding techniques for titanium aluminides including electron beam welding (EBW), laser welding and gas tungsten arc welding (GTAW) are necessary alternatives for achieving joints with the desired properties. Due to its importance to this study, the GTAW process will be described in detail in the following section.

Electron beam welding uses the high power density of an electron beam to produce excellent reproducible welds with low distortion and high integrity at high weld speeds done in a high-vacuum chamber [147]. These advantages lead to frequent application of electron beam welding in the aerospace industry. The weldability of γ-TiAl joints by

electron beam welding has been studied by Xu et al. [148]. The results have indicated that the high heat stress and microstructure brittleness cause solid state cracking in the titanium aluminide welds. EBW has been used to produce crack-free joints through controlling the weld cooling rate in order to allow the α phase to fully decompose [149, 150]. Chen et al. [151] have investigated the crack formation in electron beam welded titanium aluminides and found a composite control method to prevent cold cracking. However, the expensive equipment and restricted size of the components are major inconveniences for the development of electron beam welding.

Apart from electron beam welding, the laser welding process is also capable of high scanning speed and is readily automated for manufacturing. Major advantages include high reproducibility and very narrow beam focus, and consequently reduced distortion. In some cases, large and complex formed structures can be easily produced in an ambient atmosphere [152]. However, the reactivity of titanium aluminides with oxygen requires inert gas shielding to protect the welds. While this may place size limitations on the laser welding equipment, it is nevertheless much less expensive than providing the high vacuum environment required for EBW. In the literature, the mechanical and microstructural characteristics have been thoroughly investigated in Ti-24Al-17Nb laser welds [153] and laser welded titanium-aluminium joints [154]. Post weld heat treatment is advisable to reduce residual stress at the welds and optimise the microstructure. These results are useful for modification of the welding parameters in order to improve the properties.

2.3.4 Gas Tungsten Arc Welding

Gas tungsten arc welding (GTAW) is a fusion welding process that forms a stable electric arc between a non-consumable tungsten electrode and a workpiece of opposite polarities in an inert atmosphere, as shown in Figure 2.13 [155]. The arc produces a molten weld pool at the workpiece surface, into which additional filler material (usually in the form of wire or rod) can be fed if required by the application. For the butt joint

shown in Figure 2.13, a relatively small addition of filler material may be required to provide reinforcement of the joint. For the additive layer manufacturing process, a significantly larger quantity of material is added, to produce a significant buildup of material in order to produce the desired component as rapidly as possible.

There are a series of controlling parameters that have a dominant effect on the final product in GTAW. The arc current is a key variable that governs the penetration depth, melting width, welding speed, weld bead quality, and ultimately limits the achievable deposition rate. The arc voltage is determined by arc length, arc current, and the shielding gas. The preferred shielding gas for most reactive materials is argon, due to the low cost and low ionisation potential. Arc length has the most significant effect on the arc voltage (approximately 0.3Volt/mm), while the arcing current has a smaller influence (approximately 0.01Volt/Ampere). For short arc lengths (approximately 3mm) and moderate arc current (less than 150 Amperes), the arc voltage is dominated by the fall voltages in the anode and cathode regions. Under such conditions, the GTAW arc voltage is approximately 12 Volts.

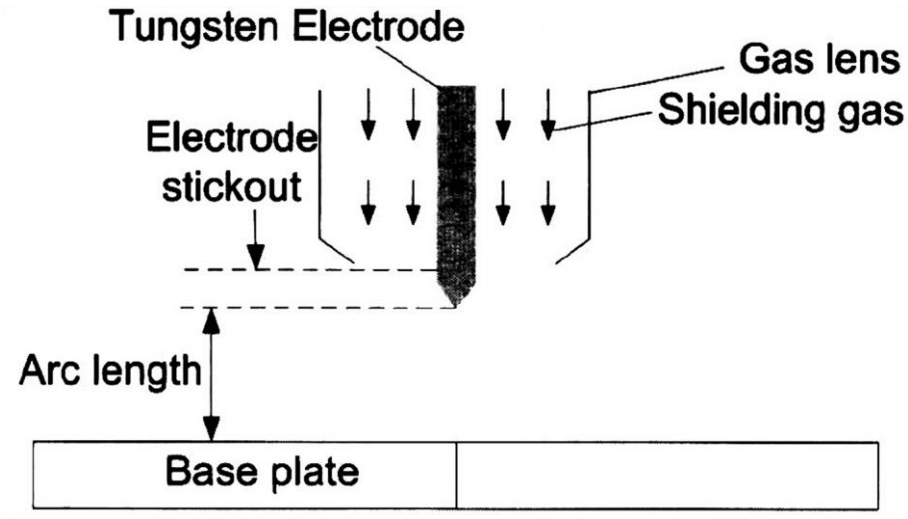

Figure 2.13 Schematic drawing of gas tungsten arc welding [155].

Generally, the arc current multiplied by the arc voltage generates the heat energy developed in the arcing zone. Approximately 80% of the heat can be transferred to the

workpiece causing a small molten region, which can solidify subsequently to form the weld metal. The size of the molten weld pool is determined by the heat input to the weld pool and the conductive and radiative heat losses away from the weld pool. In addition, the feeding rate of the filler metal is independent of the arc current, but is ultimately limited by the energy available to satisfactorily melt both the filler metal and the workpiece. Within limits, this allows independent control of dilution (mixing, or alloying, of filler material with the molten workpiece material) and the energy input to the weld.

Therefore, the GTAW process can offer great flexibility for both manual and automatic application at minimum capital investment. As a very stable and clean welding process, GTAW has become the most widely used process for joining titanium and titanium alloys [156, 157] as well as additively manufactured titanium alloys as referenced in section 2.2.3.2. However, less attention has been given to the welding of titanium aluminides using GTAW. Kelly [158] provided a detailed study on repair welding of γ-TiAl alloys with the GTAW process. The effects of welding parameters, preweld heat treatment, preheating and postweld heat treatment on the weldability of titanium aluminide welds have been investigated in this study. The results have demonstrated that crack-free GTA Ti-48Al-2Cr-2Nb titanium aluminide welds can be produced after optimising the ductility. The microstructural characteristics in both fusion zone and heat-affected zone of γ-TiAl welds using the GTAW process have been studied by Mallory et al. [159, 160]. A dendritic solidification microstructure and compositional coring produced during non-equilibrium solidification have been found in the weld fusion zone, while the weld HAZ has been found to exhibit equiaxed γ and grain boundary α_2 base metal microstructure. However, Mallory et al. did not investigate tensile properties on the GTA weldment. Bharani and Acoff [161] have successfully produced crack- and void-free γ-TiAl welds by using the GTAW process with highest current levels, which can produce the most desirable weld microstructures for both the

cast and extruded γ-TiAl alloys. Also, the weldability of γ-TiAl welds produced by GTAW and the effects of postweld heat treatment have been evaluated and discussed. The welded microstructure exhibited predominantly columnar-dendritic growth from the fusion line to the weld centreline with supersaturated α_2 phase and massive γ metastable structures. Less cracking has been obtained by increasing the welding current, which significantly decrease the amount of α_2 phase in the fusion zone. Additionally, a reduction in ductility and a decrease in tensile strength have been observed in the as-welded condition [162, 163]. Arenas and Acoff [162, 163] suggested that postweld heat treatment was effective to modify the fusion zone microstructure and decrease the hardness. However, the postweld heat treatment response of tensile properties for GTA welded titanium aluminide alloy is still unknown. As can be seen from the review of previous work, there is no published work on the γ-TiAl components produced by a combination of GTAW and ALM although it promises to be an economical manufacturing technique. A series of comprehensive studies are required to establish the feasibility of GTAW-based ALM processing routes for titanium aluminides.

2.4 General Summary of Previous Work

It is generally recognised that intermetallic γ-TiAl based alloys are promising structural materials for high temperature aerospace and automotive applications, including turbine wheels, compressor blades and pistons for reciprocating engines. Central to such applications is the attractive combination of low density, unique mechanical properties such as high specific strength and modulus, and good resistance against oxidation and corrosion.

Major effort has been devoted for over a decade to gain a deeper understanding of the phase transformation, microstructure evolution and their influence on mechanical properties. The maturity in understanding of the intrinsic characteristics has promoted

the improvement of manufacturing technologies for γ-TiAl alloys, including powder metallurgy, ingot metallurgy and casting. These conventional processes have successfully produced TiAl components with suitable mechanical properties for several high temperature applications in the aerospace and automotive industries. However, the associated cost has been acknowledged as the chief limitation for titanium aluminides to successfully reach the market in a wide range of component forms.

In order to find an economic alternative, several research studies have investigated the use of additive layer manufacturing with minimal post-processing steps for titanium aluminides. Additive layer manufacturing is used to produce complex, near net shape components through deposition of many consecutive layers in the form of powder or wire, offering high geometrical flexibility and major savings in time, material, and hence cost. For many engineering materials, relatively cost-effective fabricating processes have been provided by the appropriate combination of joining methods and additive layer manufacturing. Nevertheless, the current additive manufacturing techniques are not suitable to every manufacturing material. In the case of titanium aluminides, the main limitations of currently available additive manufacturing technology involve the cost, size limitations and material quality.

Based on the above review, research opportunities concentrate on addressing the issues of developing γ-TiAl alloys with the desired balance of mechanical properties while further reducing the overall manufacturing cost for large components. Considerable work and research are required to promote the development of additive layer manufacturing as a mainstream process for TiAl component production.

3 Experimental Instruments and Methodologies

This chapter describes the experimental instruments and methodologies used for the sample preparation and characterisation in this study. The experimental procedure and the corresponding results are introduced in the following chapters.

3.1 Gas Tungsten Arc Welding-based Additive Layer Manufacturing (GTAW-based ALM)

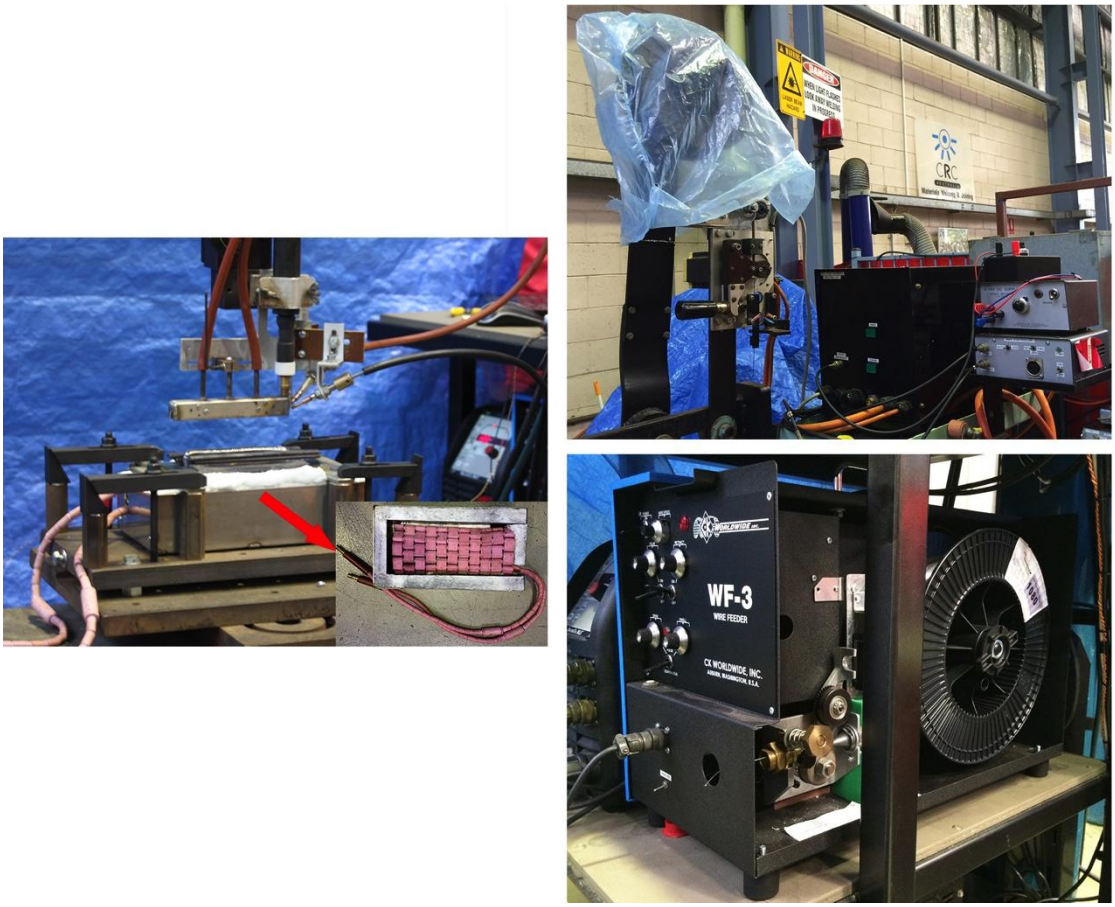

Figure 3.1 Experimental configuration of GTAW-based ALM process.

A water cooled machine mount GTAW torch and commercial GTAW inverter power source were used to provide the heat source for additive layer manufacturing of γ-TiAl

alloys and TiAl-based functionally graded materials. During the GTAW-based ALM process, an appropriately designed argon gas shielding device was used to avoid atmospheric oxidation, to produce a final product with minimal oxygen and nitrogen contamination. Interpass temperature was controlled by a preheating system using a flexible ceramic pad heater. The experimental configuration of GTAW-based ALM process is shown in Figure 3.1. The welding process parameters used for all experiments are listed in Table 3.1.

Table 3.1 Summary of GTAW-based ALM processing parameters.

Polarity	DCEN (Direct Current with Negative Polarity)
Electrode	2 % Ceriated, 2.4 mm ϕ
Shielding gas	Welding Grade Argon
Flow rate-Torch nozzle	8 L/min
Flow rate-Trailing shield Front	10 L/min
Flow rate-Trailing shield Rear	7 L/min
Pre-flow duration	30 seconds
Up slope duration	5 seconds
Down slope duration	1 second
Post flow duration	30 seconds
Travel speed	100 mm/min
Arc length	3.5 ~ 4 mm
Voltage	12 ~ 14 V

A twin-wire feeding system, consisting of two synchronised wire feeding units with integrated wire speed sensors, was used to separately deliver pure Ti wire with a diameter of 1.0 mm and pure Al wire with a diameter of 0.9 mm at individually adjustable speeds. With such an arrangement, in-situ alloying of elemental Ti and Al for

titanium aluminides can be accomplished in a well-controlled manner. These wires were deposited onto commercially pure Ti substrates with a plate size of 200 mm × 100 mm × 6 mm. The chemical composition of Ti and Al wires as well as Ti plates is shown in Table 3.2.

Table 3.2 Chemical composition of substrate and feeding wires (wt.%).

	N_{max}	C_{max}	H_{max}	O_{max}	Fe_{max}	Si_{max}	Zn_{max}	Cu_{max}	Mn_{max}	Mg_{max}	Ti_{max}	Al_{max}
Ti plate	0.03	0.08	0.015	0.25	0.30	−	−	−	−	−	Bal.	−
Ti wire	0.03	0.08	0.015	0.25	0.30	−	−	−	−	−	Bal.	−
Al wire	−	−	−	−	0.15	0.15	0.06	0.02	0.02	0.02	0.02	Bal.

3.2 Sample Preparation for Metallography

After the GTAW-based ALM process experiments were performed, the as-fabricated parts were sectioned into appropriately sized samples in the region of interest using an Accutom-50 cutting device (Figure 3.2). The parameters for the cutting process on this equipment are listed below:

Cutting Blade: Bucher series 15HC diamond, no: 11-4245

Programmed as Struers 358CA

Blade Rotation Speed: 3000 rpm

Feed Speed: 0.020 mm/s

Force Limit: Low

Cooling system: Recirculate water

Figure 3.2 Struers Accutom-50 precision cutting machine.

Figure 3.3 Struers CitoPress-20.

Afterwards, a CitoPress-20 hot mounting press, shown in Figure 3.3, was used to mount the sectioned samples in Polyfast resin (conductive). The mounted samples were then ground and polished on a Struers Tegrapol-21 automatic grinder-polisher (Figure 3.4), based on the standard metallographic method for γ-TiAl alloys. The details of the grinding-polishing procedure are given in Table 3.3.

Before microstructural investigation, the freshly polished samples were etched with Kroll's reagent consisting of 100ml distilled water (H_2O), 5ml concentrated nitric acid (HNO_3) and 3ml 3% hydrofluoric acid (HF).

Figure 3.4 Struers Tegrapol-21.

Table 3.3 Sample preparation procedures for microstructural analysis.

Procedure	Surface	Force, N	Time, minute	Solution
Grinding	1200# SiC paper	25	2	Water
Polishing	15μm MD-Pan cloth	25	15	Water-based lubricant
Polishing	0.25μm MD-Chem cloth	25	10	50% OPS

3.3 Microscopy

3.3.1 Stereo Microscopy and Optical Microscopy (OM)

A stereo microscopy (Figure 3.5) was used to obtain an overall image of the cross-sections of the as-fabricated components. The low magnification images from this microscope contributed to preliminary inspections of the macrostructure within the GTAW-based ALM produced samples.

Figure 3.5 Leica M205A stereo microscope.

Further, the microstructural characteristics of the as-fabricated materials were determined by Leica DMR optical microscope (Figure 3.6). The high-magnification visible-light images captured by this equipment are used to present the cross-sections of samples in subsequent sections.

Figure 3.6 Leica DMR optical microscope.

3.3.2 Scanning Electron Microscopy

The key microstructure of GTAW-based ALM produced samples and fractographic features of broken tensile samples in this work were primarily characterised using a JEOL JSM-6490LA scanning electron microscopy (SEM) equipped with an energy dispersive X-ray spectrometer (EDS) as shown in Figure 3.7, operating at 20 kV.

In addition, the achievable microstructure in γ-TiAl alloys is strongly influenced by the chemical composition. Therefore, it is important to investigate the chemical composition of as-fabricated materials. Because different atomic elements have different atomic structure which generates a unique X-ray emission spectrum, the elemental analysis in this work was performed by using the EDS technique.

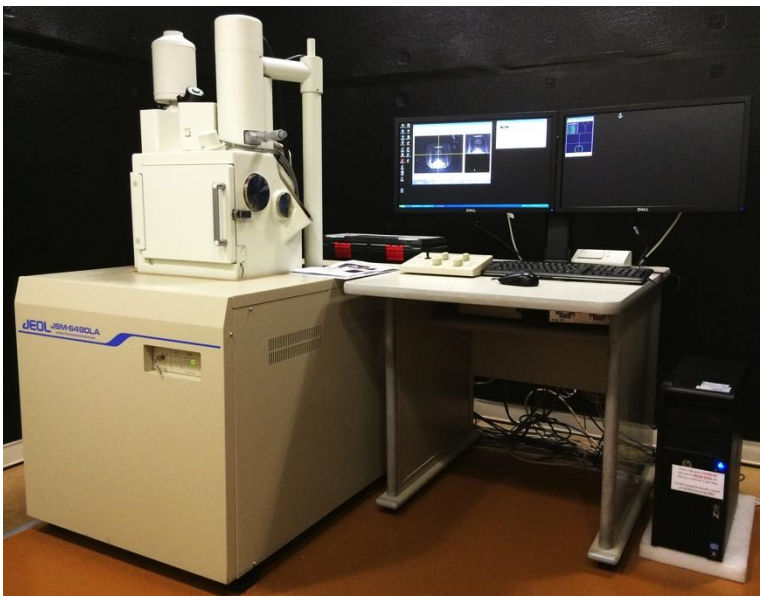

Figure 3.7 JEOL JSM-6490LA SEM.

3.4 X-ray Diffraction

The phase constitution of all samples in this study was identified by X-ray diffraction (XRD) performed with a GBC MMA X-ray diffractometer (Figure 3.8) using monochromatic Cu Kα radiation (wavelength λ = 1.5418Å). All diffraction patterns were obtained in a continuous-scan mode with a scanning speed of 4° min^{-1} in the range of 20 ~ 90°. The accelerating voltage and tube current were set at 35 kV and 28.6 mA, respectively. The volume fractions of the different phases were estimated using the integrated intensities through Rietveld refinement.

Figure 3.8 GBC MMA X-ray diffractometer.

3.5 Neutron Diffraction and Contour Method

Neutron diffraction experiments on the GTAW-based ALM produced samples were conducted using a high-intensity and high-speed powder diffractometer (WOMBAT) at the OPAL research reactor of the Australian Nuclear Science and Technology Organisation (ANSTO) [164]. This instrument is capable of accurately measuring light elements in the presence of heavy elements, and is also well suited for multiphase materials and for quantitative phase analysis, in which the presence of minority materials can be measured accurately.

Contour method was applied to measure the residual stress of the GTAW-based ALM produced samples and low temperature heat treated samples. All the experiments were conducted at The Open University in the United Kingdom.

3.6 Mechanical Tests

3.6.1 Microhardness Testing

The microhardness testing were performed on a DuraScan 70 automatic hardness tester using the Vickers hardness method. This facility is shown in Figure 3.9. A load of 200 g was applied to each sample. Each indent was evaluated using Ecos Workflow^{TM} software and the corresponding results were presented graphically.

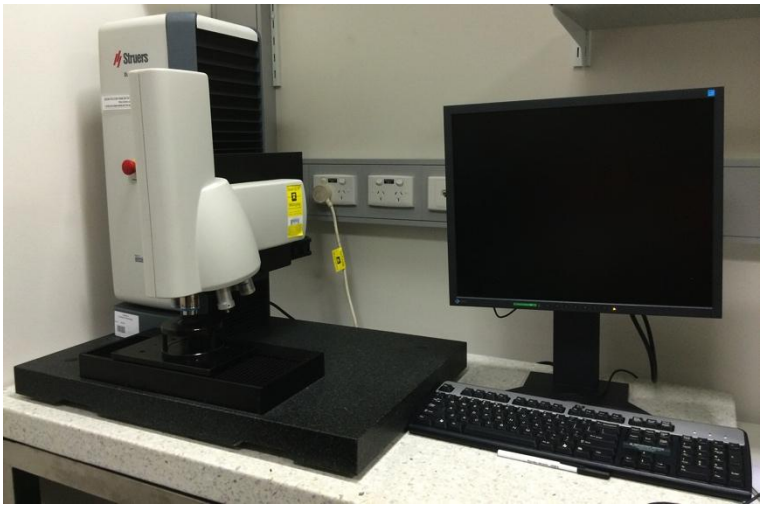

Figure 3.9 DuraScan 70 automatic hardness tester.

3.6.2 Tensile Testing

The tensile testing of all samples was performed at room temperature on a MTS370 servo-hydraulic load unit under automated control (Figure 3.10). The applied strain rate was 0.05 s^{-1}. The sample dimensions are shown in Figure 3.11.

Figure 3.10 Photo of MTS370 machine.

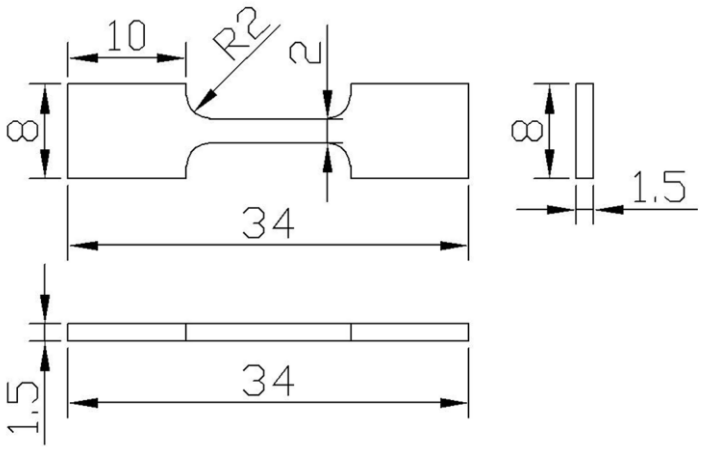

Figure 3.11 Configuration of specimen for tensile testing, units are in mm.

4 Effect of Processing Parameters on γ-TiAl Alloys Produced by the GTAW-based ALM Process

4.1 Introduction

Over the previous decade, additive layer manufacturing (ALM) has been shown to be a feasible and economical alternative to traditional manufacturing methods for many conventional metals due to its ability to produce geometrically intricate components with major savings in time, material, and hence cost [9, 10].

Aerospace and automotive components made from materials such as titanium alloys and titanium aluminides that are difficult to manufacture by conventional production processes represent particularly interesting applications for additive manufacturing. As reviewed in Chapter 2, gamma titanium aluminides are promising structural materials due to the attractive combination of low density, unique mechanical properties, and resistance to oxidation. However, limited work has been devoted to developing ALM processes for titanium aluminide alloys when compared to other alloys. Moreover, all previous research on ALM processed titanium aluminide alloys has been conducted using laser or electron beam as heating source and pre-alloyed metal powders as the deposition medium. Depending on the powders used, the resulting deposits can exhibit an unacceptably high level of defects and impurities. To address this issue, the use of material in the form of solid wire has received attention because the wire-feeding processes are less susceptible to contamination from the atmosphere in comparison to processes using powders [107]. However, the feedstock material is generally restricted to a single wire with the same composition as the substrate, even though studies on wire and arc additive manufacturing technique have been extensively documented [108, 125, 126, 165].

Although more interest has gravitated to wire and arc additive layer manufacturing (WAALM) with the continuing need to reduce the cost and contamination [125, 126, 165, 166], no information is currently available on the use of WAALM to fabricate titanium aluminides, in particular the effects of processing parameters on microstructure and properties. In this context, the present work focuses on an innovative additive layer manufacturing approach for titanium aluminides. The gas tungsten arc welding process combined with in-situ alloying from separate wire feeding of Ti and Al elements is used to produce γ-TiAl based alloys, thereby providing the flexibility of altering the composition during fabrication.

In considering the conditions necessary for efficient production of additively manufactured parts, the bead geometry should be optimised for minimum waste. Moreover, the heat source, feedstock ingredients and deposition process must be critically selected with the objective of achieving components with acceptable properties and shapes. It is well known that welding relies on the heat input, which is dependent on the variables shown in following equation.

$$Q = \frac{EI}{v}\eta \qquad \text{Eq. 4.1}$$

where Q is the heat input (J/mm), E is the voltage (V), I is the arc current (A), η is the arc efficiency, and v is the welding speed (mm/min). The arc current is the driving factor as it provides the energy to melt the feeding wires when the other variables are kept constant. If there is insufficient or very low arc current it will not allow the weld metal and the parent metal to fuse or join properly. If the arc current applied is excessive it will produce an unnecessarily wide weld pool and hence an over-built deposit that will require a large amount of material to be removed by machining in order to achieve the desired shape. Excessive current can also create turbulence in the shielding gas and weld pool, thus causing contamination.

Furthermore, for this novel GTAW-based ALM approach as well as other additive manufacturing techniques, it is important to understand the effects of the processing parameters on microstructure and properties, in order to achieve material of acceptable quality, repeatability, and reproducibility. Similar to multipass welding processes applied to conventional metallic alloys, the interpass temperature for WAALM is an important process parameter that affects the microstructural and mechanical properties of the fabricated component. Interpass temperature refers to the temperature of the material in the weld area immediately before the second and each subsequent pass of a multiple pass weld [167]. When welding ferrous alloys, a controlled interpass temperature slows the cooling rate through the alloy's critical temperature to avoid occurrence of defects. Particularly for γ-TiAl alloys, crack-free parts with improved microstructure can be obtained at appropriate cooling rates [150, 151]. In general, γ-TiAl alloys are sensitive to solid-state cracking caused by high heat stress and microstructure brittleness [148, 162], which can be strongly influenced by the interpass temperature. When the constraint in the weldment is small, phase transformations that occur during welding of TiAl play a critical role in weld quality, as investigated by Chaturvedi [150]. Therefore, the influence of interpass temperature on γ-TiAl alloys is only considered for microstructural characteristics in this study.

A key concern for the in-situ alloying process is the effectiveness of the wire mixing behaviour during production of the as-fabricated materials, which determines the microstructure and thus the uniformity of the properties.

Therefore, this chapter aims to better understand the influence of different processing parameters including arc current, interpass temperature and wire feed conditions on the geometry, microstructural characteristics and microhardness of the in-situ alloyed and additively manufactured titanium aluminide components, and thereby decide upon a suitable combination of parameters for future application of this process.

4.2 Experimental Procedure

4.2.1 Investigated Materials

The titanium aluminide alloys used in the current study were all produced by additive layer manufacturing based on GTAW and in-situ alloying. A pure titanium substrate was used as a base metal for depositing the alloys. The GTAW torch was focused on the substrate to create a melt pool into which the Ti and Al wires were delivered individually by two wire-feeding units. In this case, the Ti and Al elemental wires were separately delivered into the weld pool, and the elements are mixed in the molten pool. The elemental feed rates were controlled individually by independently setting the speed of the two-wire feeding units. Figure 4.1 shows the schematic drawing of GTAW-based ALM process. The first layer was bonded to the substrate. After completing a layer, the GTAW torch and the twin wire feedstock nozzles were raised vertically by a distance equal to the layer thickness. A new layer was subsequently deposited onto the previous layer until the component was fully constructed in the layer-by-layer fashion. The deposition process was protected from oxidation by using an appropriately designed argon gas shielding device, to produce a final product with minimal oxygen and nitrogen contamination. The basic processing parameters of the equipment can be found in Table 3.1, and these remained constant for all experiments. Three sets of walls were produced to the effect of the processing parameters (arc current, interpass temperature and wire feed rate ratio) on the final materials:

(1) Set 1: Three straight walls with 6 layers each were built using different arc current (120, 140 and 160 A) at 765 mm/min Ti wire-feeding rate and 855 mm/min Al wire-feeding rate, in order to investigate the effect of arc current on the final product. The desirable composition was Ti-(43~45) at.% Al based on the calculation of the selected wire-feeding rate. The interpass temperature of 100 °C was used to conduct these experiments.

(2) Set 2: Five straight walls with 20 layers each were fabricated using 120 A current with the same wire feed rate for both wires as in Set 1, to study the effects of interpass temperature. Various interpass temperatures were selected from 100 to 500 °C.

(3) Set 3: Four straight walls, all 100 mm in length, were produced at different wire feed rate ratio using 120 A current and 400 °C interpass temperature. Four groups of Al and Ti wire feed settings were selected: these were 615 mm/min Al and 765 mm/min Ti for Group 1; 730 mm/min Al and 765 mm/min Ti for Group 2; 855 mm/min Al and 765 mm/min Ti for Group 3; and 1015 mm/min Al and 780 mm/min Ti for Group 4. Their corresponding ratios of Al to Ti wire-feeding rates are 0.80, 0.95, 1.12 and 1.30, respectively for the four groups. The final products were investigated in detail to explore the effects of wire feed ratio.

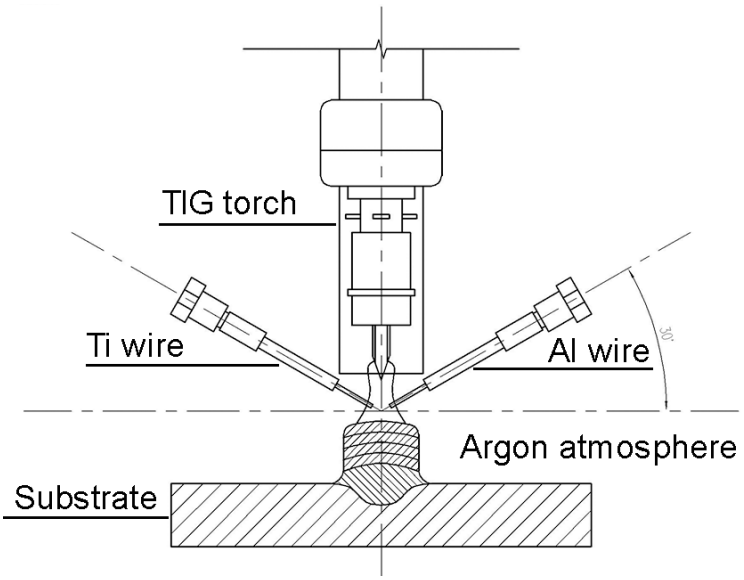

Figure 4.1 Schematic representation of GTAW-based ALM process.

The following analyses were performed to compare the specimens: wall width and height measurements (only for set 1), microstructure observation, chemical composition and phase evaluation, and microhardness tests.

4.2.2 Metallography

Optical micrographs (OM) were taken of the polished and etched cross-sections. Scanning electron microscopy (SEM) equipped with an energy dispersive X-ray spectroscopy (EDS) analysis system was utilised to determine the element distribution in the different regions of the Set 1 specimens. In order to gain a clear indication of the wire mixing behavior in the GTAW-based ALM produced wall components, compositional analysis of the specimens from Sets 2 and 3 was conducted by EDS measurements adjacent to hardness indentations at approximately 1 mm distance. The accuracy of all chemical composition measurements is ± 0.5 at.%. Phase identification was performed using X-ray diffractometer (XRD) with Cu Kα radiation (λ = 1.5418Å).

4.2.3 Microhardness Testing

All of the Vickers microhardness values were measured on cross-sections of the specimens at a load of 200 g (HV0.2).

The average microhardness value for each of the three walls in Set 1 was calculated from 5 indentations at any one region. Vickers microhardness profiles were performed along the wall vertical centreline at 1 mm intervals from the fusion line to the last layer for all the specimens in Set 2 and 3. The mean hardness value and its standard deviation were then calculated for each sample.

4.3 Results

4.3.1 Geometry of As-fabricated Walls

Generally the arc current is a controlled parameter that has the greatest effect on the bead geometry [168]. The two basic geometrical properties are the width and the height of deposited materials. For a given volume, the width and the height are two competing

geometries. If the width increases the height should decrease for a given material deposition rate, and this ratio can be altered by changing the arc current.

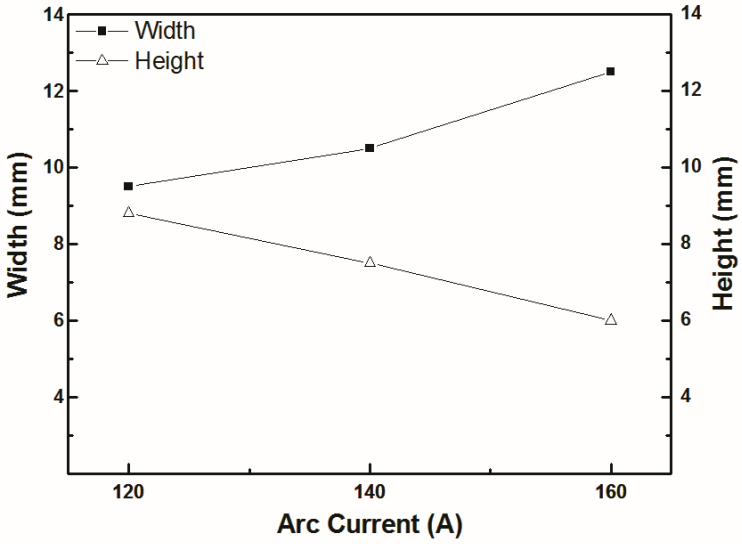

Figure 4.2 Effect of arc current on geometry of the wall components produced by GTAW-based ALM process.

Figure 4.2 shows the effect of the arc current on the geometry of the as-fabricated wall components. The width of the as-fabricated walls exhibits an increasing trend with an increase in the arc current from 120 to 160 A. The situation was reversed for the effect of arc current on the height of the as-fabricated walls. The heat input is directly proportional to the product of arc current and arc voltage. An increase in current will result in an increase in the heat input for constant arc length. Although there is a large amount of heat produced, the amount of material that is deposited fails to retain the heat, therefore cooling faster. The energy input per unit mass of deposited material (Joules per gram) is much greater than what is required to melt the feed wires, which increase the width of the weld pool. The width and height always compete, as they have to match the volume of materials deposited. Consequenly, the width of the as-fabricated walls will be increased while the height will be limited.

In addition, the arc current strongly influences the weld pool penetration, as shown in the typical cross-sections of the GTAW-based ALM produced walls in Figure 4.3. With

increasing the arc current, much more dilution from the pure Ti substrate that is mixed into the weld pool during deposition of the first layer, where penetration of the weld pool into the substrate is over 2 mm for 160 A arc current (Figure 4.3c). This effect is reduced as the next few layers are added.

In regards to the separate issue of heat affected zone (HAZ) in the substrate, the unexpectedly larger HAZ of the 120 A built sample when compared with that of the 140 A built sample is the result of applying the first two heating passes without feeding wires. This was not done for the other two samples, where material was deposited from the first pass onwards.

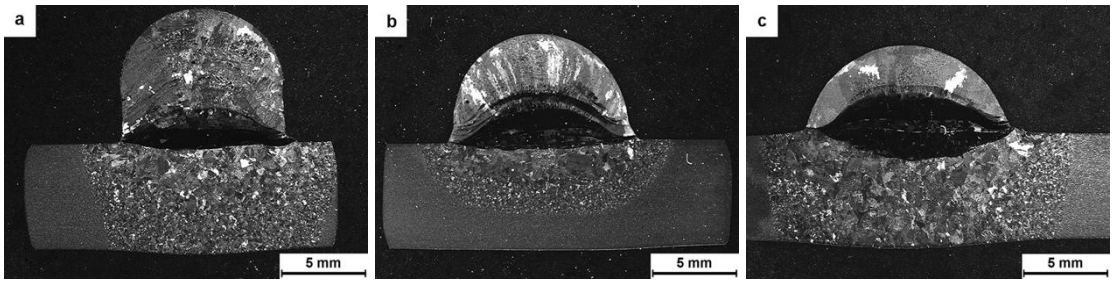

Figure 4.3 Typical cross-section morphology of wall components produced by GTAW-based ALM process using different arc current: (a) 120 A, (b) 140 A, and (c) 160 A.

4.3.2 Effect of Processing Parameters on Macro- and Microstructure

4.3.2.1 Effect of Arc Current on Macro- and Microstructure

It can be seen from Figure 4.3 that all values of arc current produce the typically rounded top surface resulting from the surface tension of the molten material in the weld pool. Large columnar grains oriented parallel to the build-up direction can also be observed, similar to those described in ALM-built Ti-6Al-4V products [120, 169].

The microstructural characterisation in the cross-sections of the GTAW-based ALM produced walls is shown in Figure 4.4. The representative microstructure within the as-fabricated walls is mainly dendrites and lamellar colonies. Arenas [162] described similar microstructures in titanium aluminide welds produced by GTAW. Less dendrites

and interdendritic structures while more lamellar colonies are optically visible in the samples as the arc current is increased from 120 to 160 A as shown in Figures 4.4a, 4.4c and 4.4e. For all samples, on the other hand, the near-substrate zones exhibit a totally different microstructure when compared with the microstructure in the top regions. Inhomogeneous coarse grains decorated by fine plates within each grain interior are observed in the near-substrate zones of samples produced by 120 A (Figure 4.4b) and 140 A (Figure 4.4d), while acicular laths can be found inside the grains with a network of crooked grain boundaries for the 160 A fabricated sample in Figure 4.4f.

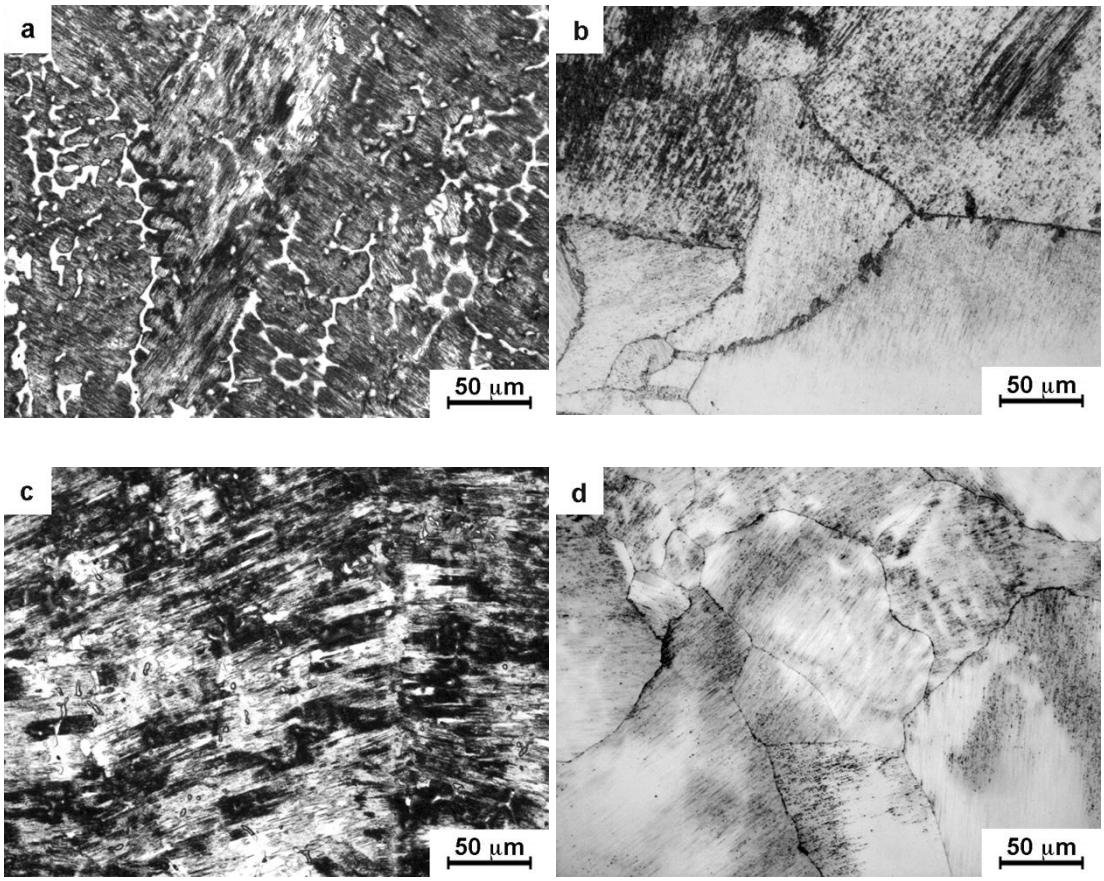

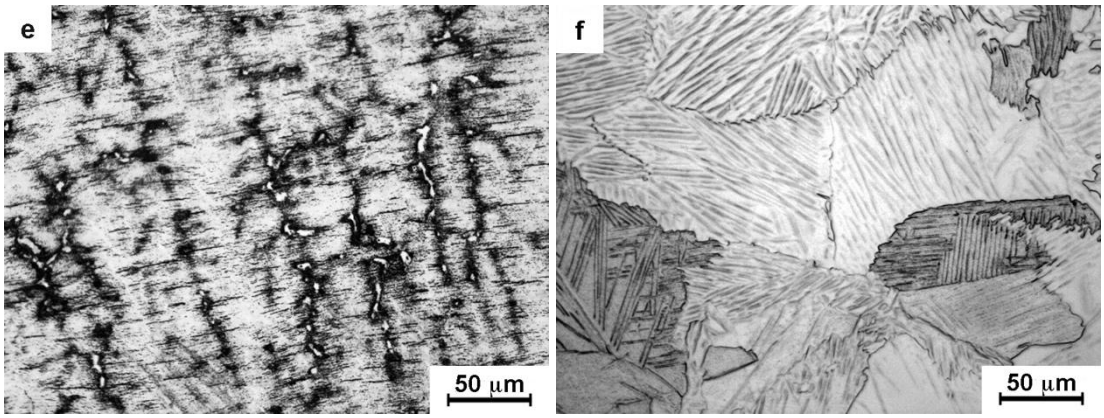

Figure 4.4 Representative microstructure of different regions in wall components produced by GTAW-based ALM process using different arc current: (a) top region and (b) near-substrate zone in the sample produced by 120 A arc current, (c) top region and (d) near-substrate zone in the sample produced by 140 A arc current, (e) top region and (f) near-substrate zone in the sample produced by 160 A arc current.

4.3.2.2 Effect of Interpass Temperature on Macro- and Microstructure

The micrographs in Figures 4.5 ~ 4.8 show the influence of different interpass temperature on microstructure in the same region of the GTAW-based ALM produced walls. The microstructure in cross-sections of each component is described in top, middle and near-substrate regions. All of the samples have coarse α_2 grains with γ laths precipitated at grain boundaries in the near-substrate zone (Figure 4.5). As the build-up continues, fully lamellar colonies with differing sizes and interdendritic γ structures are observed forming layer by layer. Therefore, the microstructures in Figure 4.6 and Figure 4.7 appear alternatively in the middle region. The top regions (Figure 4.8) present finer dendrites and interdendritic areas in comparison to the microstructure in the middle region.

Considering the same region in different samples, the different interpass temperature provides similar microstructural characteristics. Additionally, slightly finer and fewer dendrites and interdendritic structure are found in the top region as the samples undergo higher interpass temperatures.

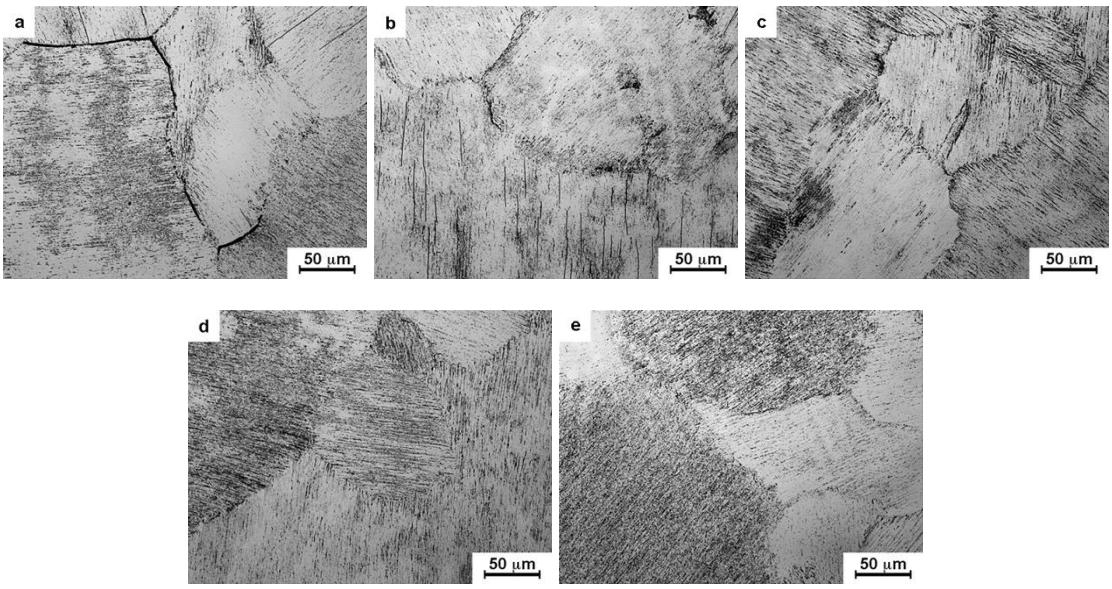

Figure 4.5 Typical microstructure in the near-substrate zone of the GTAW-based ALM produced walls experiencing different interpass temperature: (a) 100 °C, (b) 200 °C, (c) 300 °C, (d) 400 °C, and (e) 500 °C.

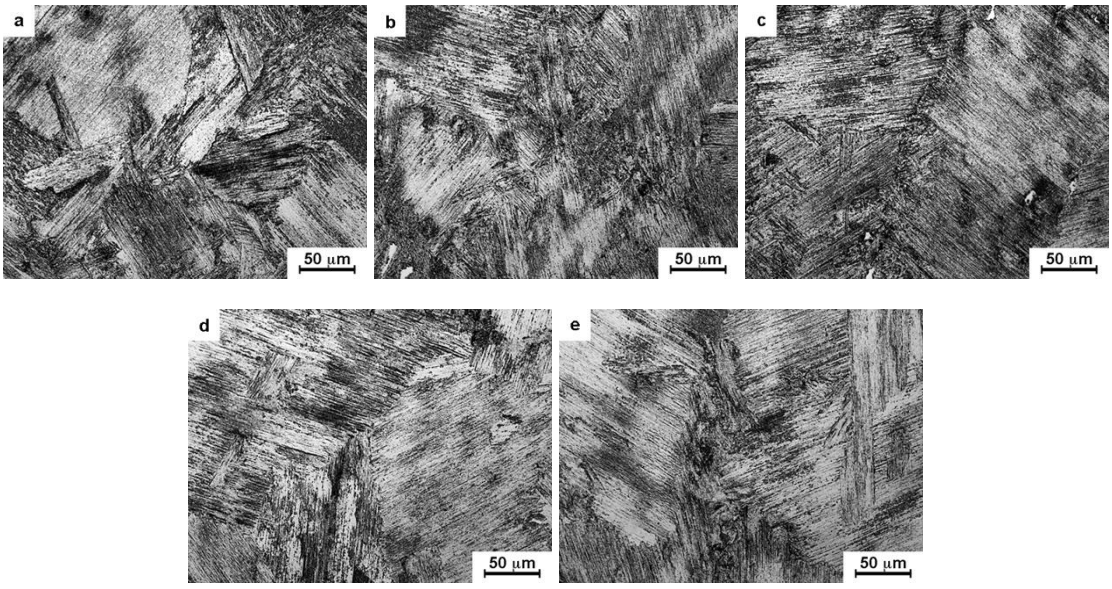

Figure 4.6 Typical microstructure in the middle region of the GTAW-based ALM produced walls experiencing different interpass temperature, lamellar colonies consist of α_2 and γ lamellae: (a) 100 °C, (b) 200 °C, (c) 300 °C, (d) 400 °C, and (e) 500 °C.

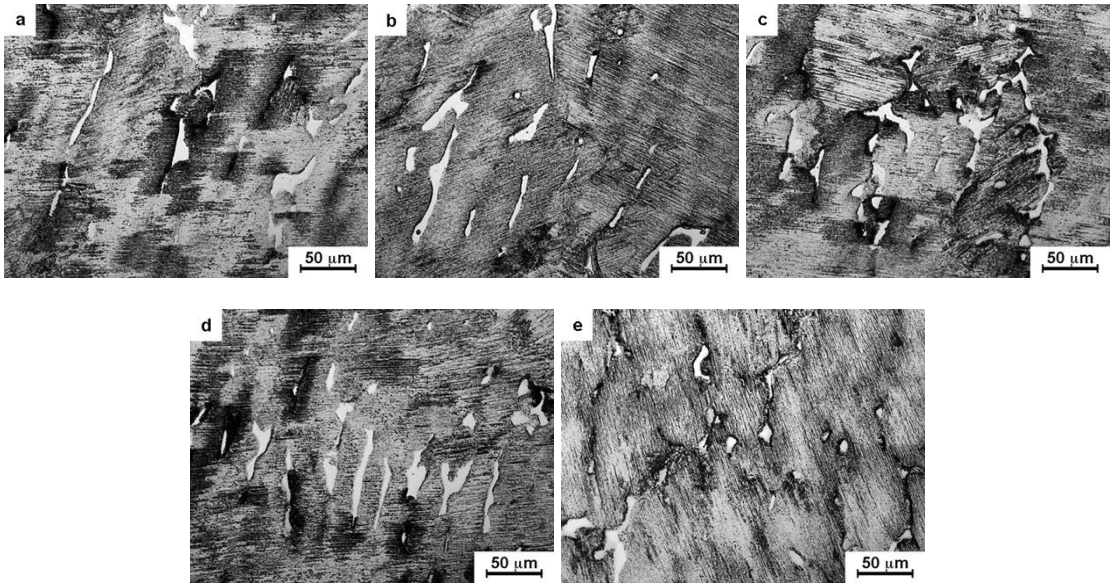

Figure 4.7 Typical microstructure in the middle region of the GTAW-based ALM produced walls experiencing different interpass temperature, the white areas show the interdendritic γ phase: (a) 100 °C, (b) 200 °C, (c) 300 °C, (d) 400 °C, and (e) 500 °C.

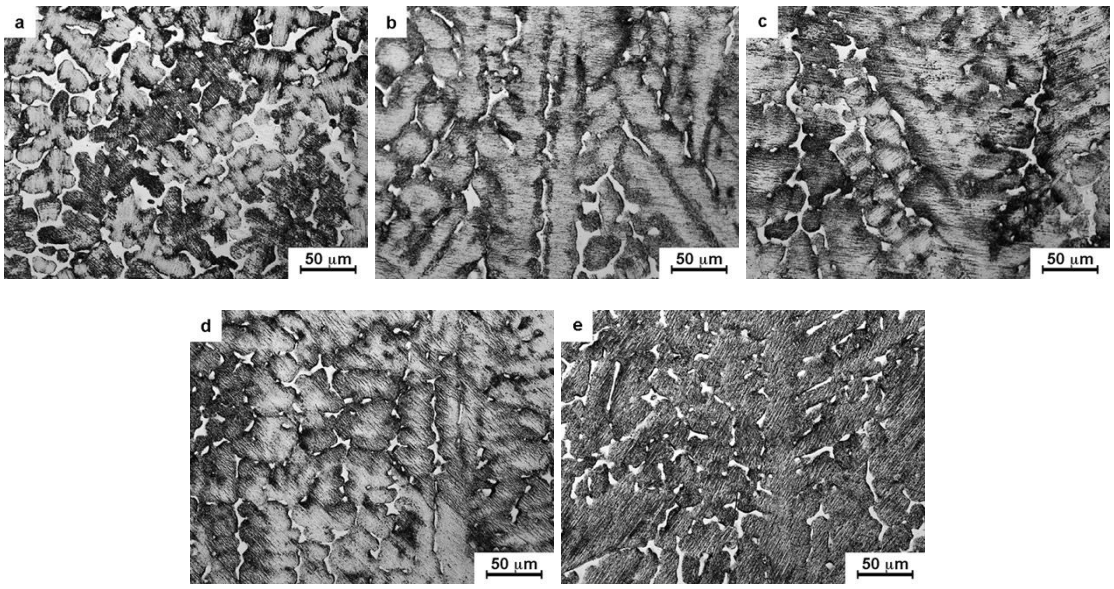

Figure 4.8 Typical microstructure in the top region of the GTAW-based ALM produced walls experiencing different interpass temperature, the white areas show the interdendritic γ phase: (a) 100 °C, (b) 200 °C, (c) 300 °C, (d) 400 °C, and (e) 500 °C.

4.3.2.3 Effect of Wire Feed Rate Ratio on Macro- and Microstructure

Microscopic characteristics analysis in the cross-sections of the GTAW-based ALM produced walls does not show any appreciable change in microstructure as a function of wire-feeding rate ratios, even though the change in ratio results in significantly different Al:Ti atomic ratios.

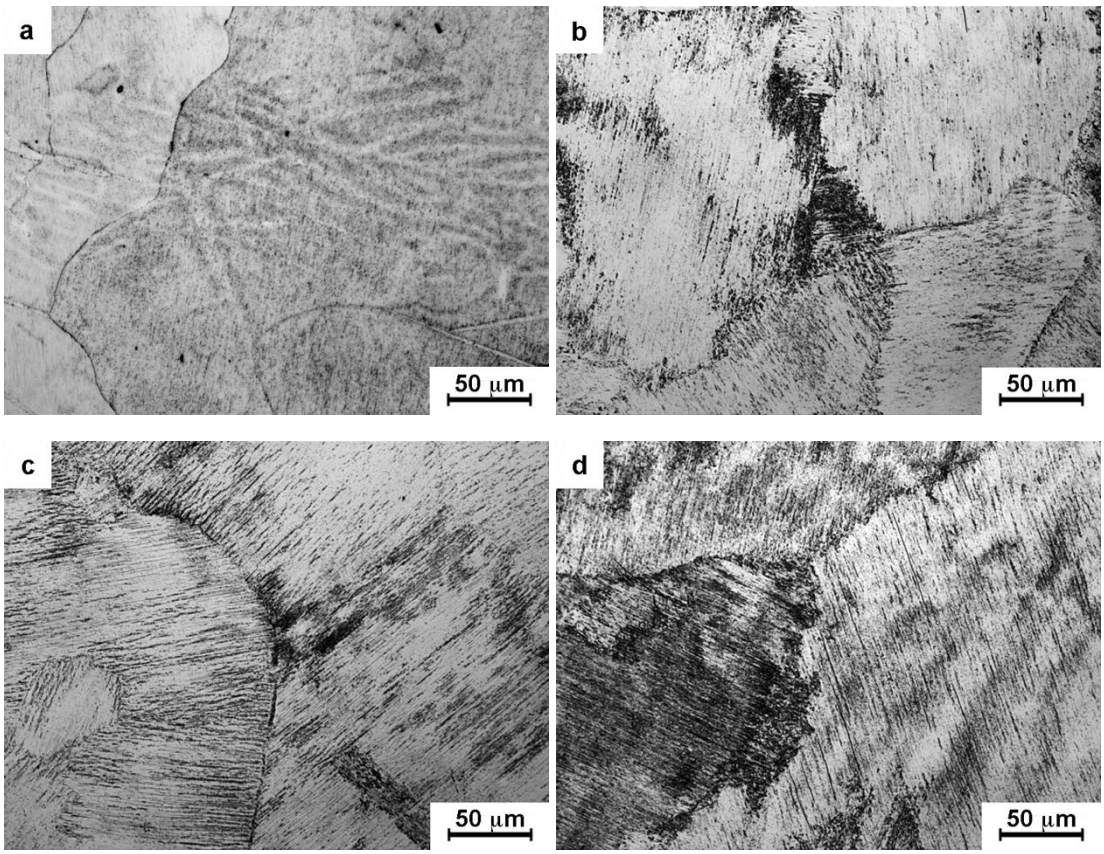

Figure 4.9 Representative microstructure in the near-substrate zone of the GTAW-based ALM produced walls using wire feed rate ratio of 0.80, the white areas show the interdendritic γ phase: (a) top region, (b) and (c) middle region, and (d) near-substrate zone.

As shown in Figures 4.9 ~ 4.11, dendritic, interdendritic structures and lamellar colonies with different proportions at different locations compose the characteristic microstructure within the as-fabricated walls. The near-substrate zone presents comparatively large α_2 grains as shown in Figure 4.9. Some finer γ laths precipitate at the grain boundaries and display more contrast variation. Fully lamellar colonies with different sizes (Figures 4.10a~d) and interdendritic γ structure (Figures 4.10e~h) can be found in the middle region of the samples. The finer dendrites and interdendritic γ phases surrounded by lamellar microstructure are visible in the top layers in Figure 4. 11.

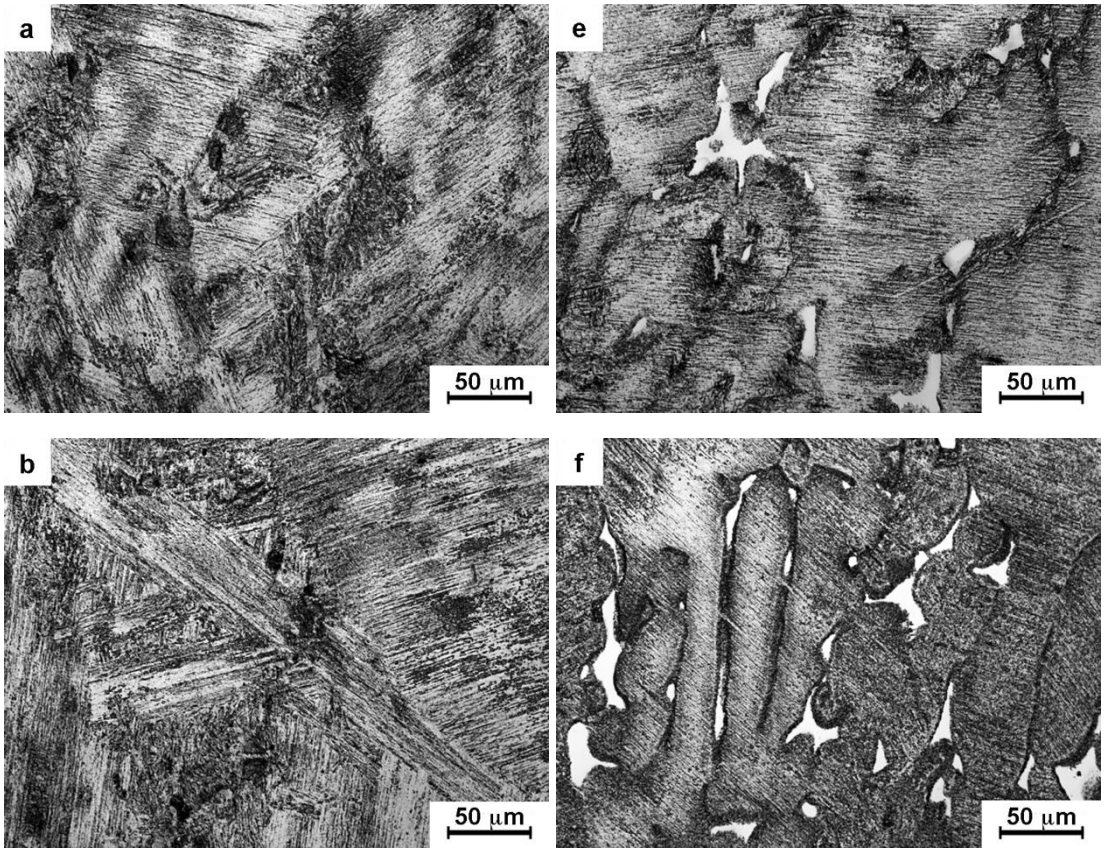

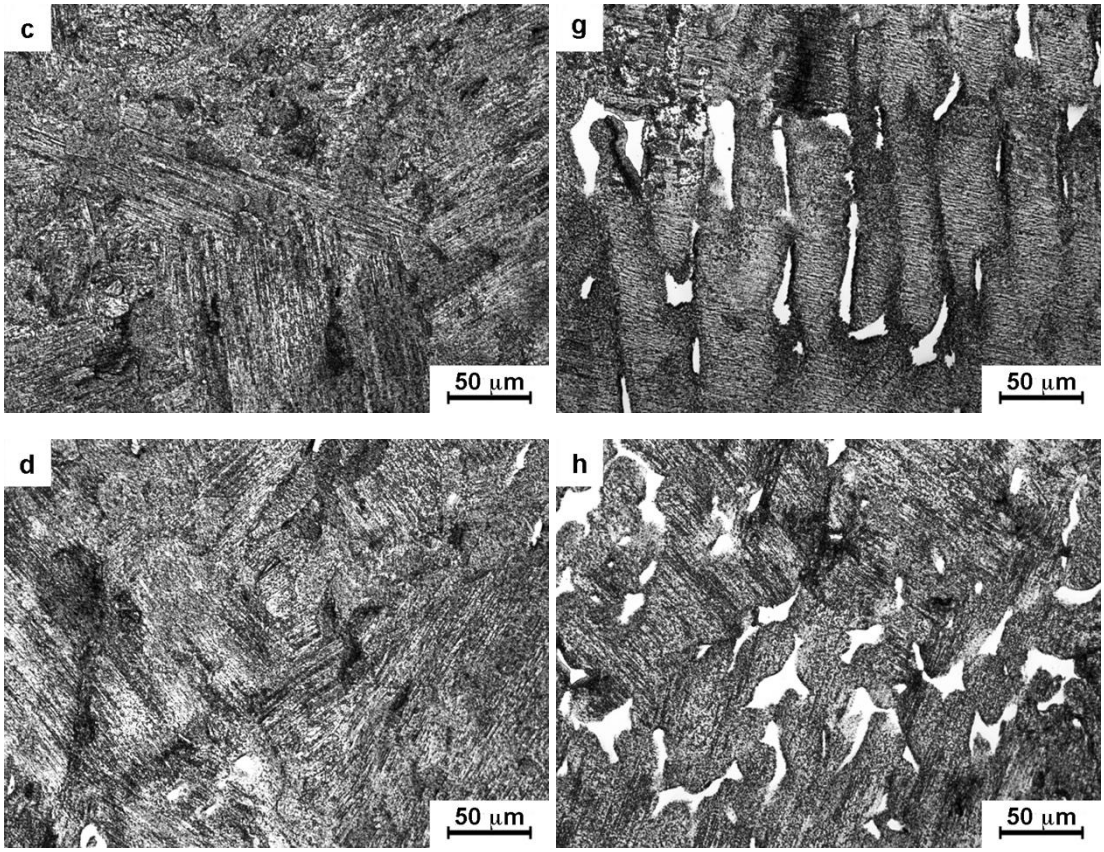

Figure 4.10 Representative microstructure in middle region of the GTAW-based ALM produced walls using different wire feed rate ratio, the white areas show the interdendritic γ phase: (a) and (e) 0.80, (b) and (f) .95, (c) and (g) 1.12, and (d) and (h) 1.30.

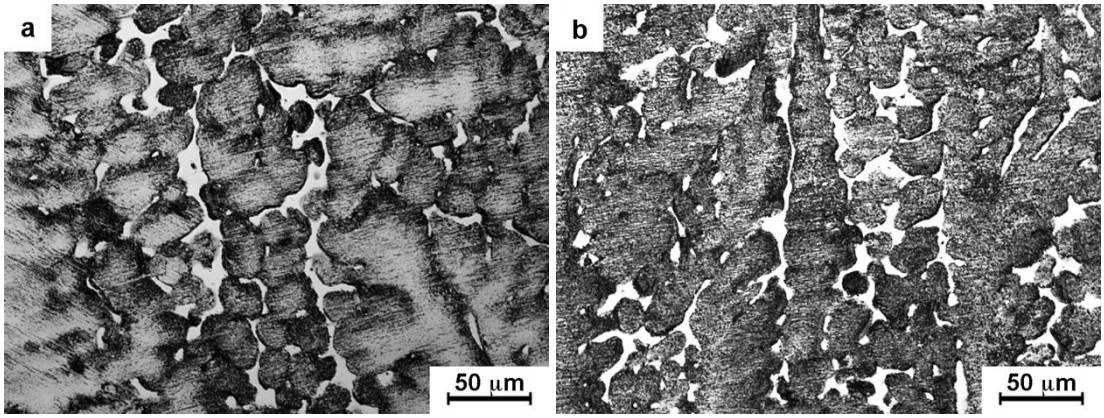

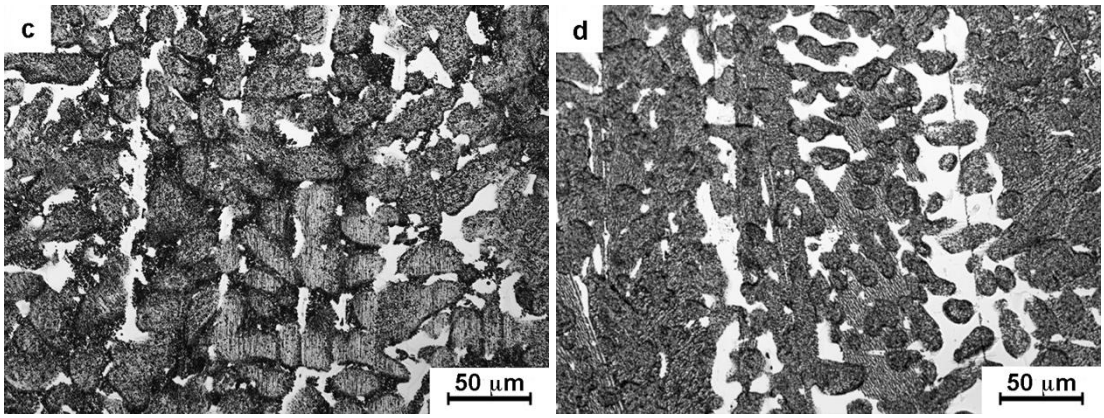

Figure 4.11 Representative microstructure in the top region of the GTAW-based ALM produced walls using different wire feed rate ratio, the white areas show the interdendritic γ phase: (a) 0.80, (b) 0.95, (c) 1.12, and (d) 1.30.

4.3.3 Effect of Processing Parameters on Chemical Composition and Phase Constitutions

4.3.3.1 Effect of Arc Current on Chemical Composition and Phase Constitutions

The compositional measurement results are shown in Figure 4.12. The average value of Al content is similar for the top regions of the three walls using different arc current. However, the near-substrate zones of all the walls have lower Al intensity than the top regions. This is attributed to the Ti dilution from the substrate as discussed earlier. Furthermore, the percentage of Al in the near-substrate zone can be considerably decreased by increasing the arc current. Only 21.2 at.% Al can be found in the near-substrate zone of the 160 A fabricated wall. A high arc current produces a larger welding pool and further increases Ti dilution, resulting in a reduced Al content. These results quantitatively confirm that increasing arc current tend to create more Ti dilution, as seen qualitatively in the cross-sections of Figure 4.3.

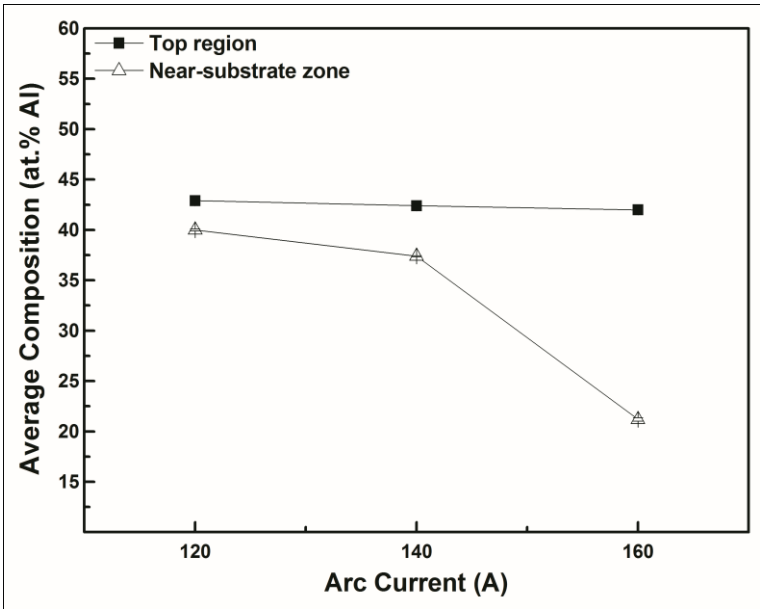

Figure 4.12 Average Al intensity of different regions obtained by EDS in the cross-sections of wall components produced by GTAW-based ALM process using different arc current.

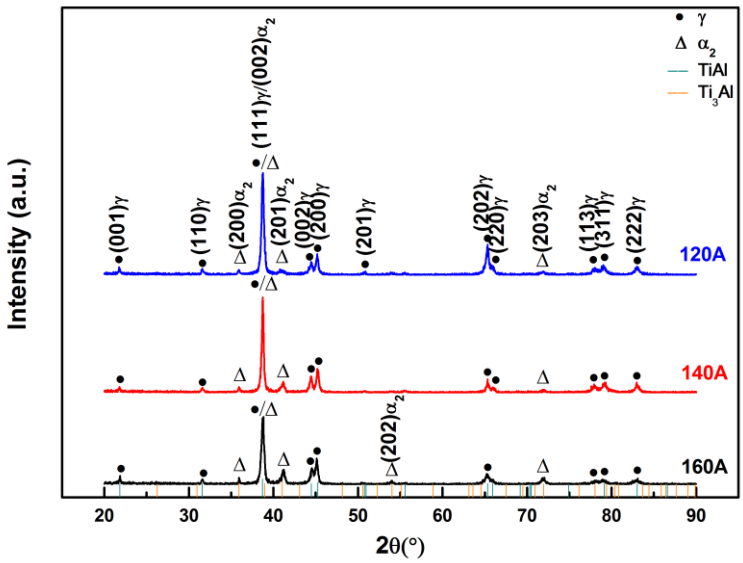

Figure 4.13 Phase constitutions in the wall components produced by GTAW-based ALM process using different arc current.

Correspondingly, the phases in the GTAW-based ALM produced walls using different arc currents were identified by XRD analyses, with the results being shown in Figure 4.13. All of the diffraction patterns indicate that the main constituent phases are γ-TiAl and α_2-Ti_3Al. The predominant γ phase peak of the wall built with 120 A arc current is

clearly stronger than those of the other walls. Increasing the arc current to 160 A can lead to higher cooling rate as discussed earlier (Section 4.3.1), which produces more α_2 phase.

4.3.3.2 Effect of Interpass Temperature on Chemical Composition and Phase Constitution

Quantitative EDS analysis was conducted to determine the elemental composition, as elucidated in Figure 4.14. A higher interpass temperature creates a larger near-substrate zone, which has much lower Al concentration than the other regions within each sample (Figure 4.14a). Nevertheless, the main section of the as-fabricated walls shows consistent aluminium content for the different interpass temperatures. The measurements are compared in Fig 4.14b, which shows the average value of the Al concentration for the majority region of each wall and the range of variation of the relative measurement points in Figure 4.14a. These results are consistent with the microstructural characteristics.

Figure 4.15 shows the X-ray diffraction patterns and corresponding phase fractions in the GTAW-based ALM produced γ-TiAl walls as a function of interpass temperature. All the components consist of γ-TiAl and α_2-Ti_3Al phases. No other phases are detected by XRD. Additionally, the amount of the two phases in the alloys is clearly different, as revealed in Figure 4.15b. The γ phase fraction clearly increases as the interpass temperature is increased to 400 °C, while the fraction of α_2 phase significantly decreases. If the interpass temperature is further increased to 500 °C, no significant change is obtained in the volume fraction of the two phases.

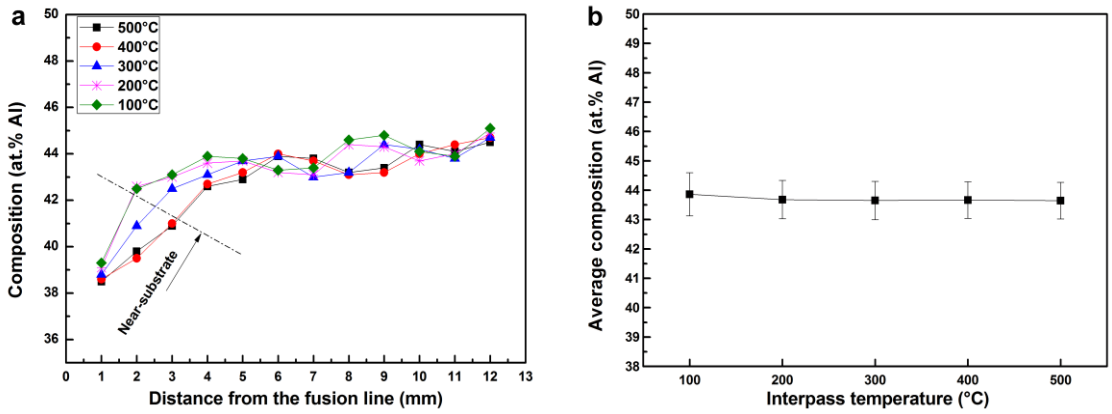

Figure 4.14 Quantitative EDS analysis on the cross-sections of the GTAW-based ALM produced walls experiencing different interpass temperature: (a) Quantitative Al concentration alongside the centreline, and (b) Mean Al intensity of the majority region except the near-substrate zone. Error bars show one standard deviation.

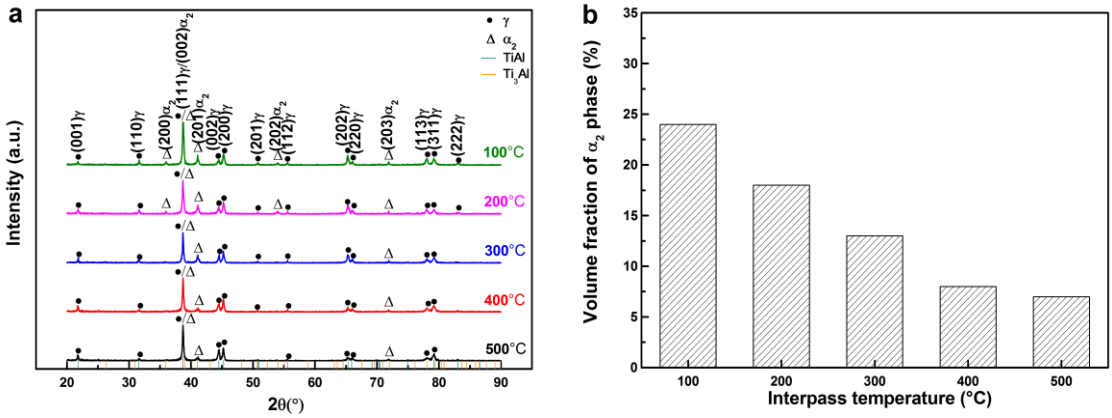

Figure 4.15 Phase constitutions in the GTAW-based ALM produced walls experiencing different interpass temperature: (a) XRD diffraction patterns, and (b) Volume fraction of α_2 phase obtained by Rietveld method.

4.3.3.3 Effect of Wire Feed Rate Ratio on Chemical Composition and Phase Constitution

The compositional measurement results are shown in Figure 4.16a. Only a small variation of Al distribution throughout the build height can be found, and the magnitude of the variation is similar for the four different wire feed conditions. The greatest deviation from average composition occurs near the substrate. This is expected because of dilution from the pure Ti substrate that is mixed into the weld pool during deposition of the first layer, where penetration of the weld pool into the substrate is over 2 mm.

This effect is reduced as the next few layers are added, since the weld pool penetrates layers that have progressively lower Ti content. In the majority region of the wall, the measurements indicate stable and uniform wire mixing.

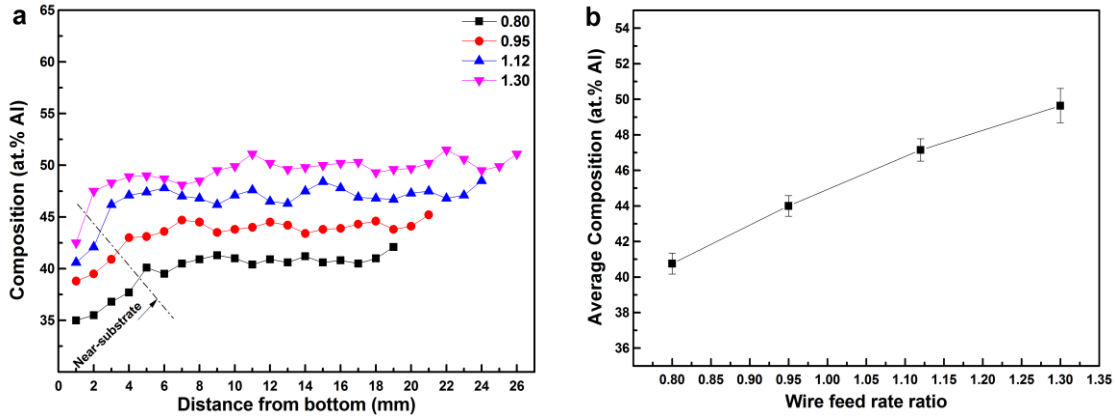

Figure 4.16 Microchemical analysis obtained by EDS from the cross-sections of wall components produced by GTAW-based ALM process under different wire feed conditions: (a) quantitative Al concentration alongside the centerline of the as-fabricated wall specimen, and (b) average Al intensity of the majority region except the near-substrate zone.

Figure 4.16b shows the average value of Al content for the majority region of each wall, and the range of variation of the relative measurement points in Figure 4.16a. The sample with the Al:Ti feed rate ratio of 1.30 has less homogeneous Al distribution, but the variation is only marginally more than that of the other ratios. Furthermore, it can be seen from Figure 4.16b that the average Al concentration can be considerably increased by increasing the ratio from 0.80 to 1.30.

The corresponding XRD diffraction results are shown in Figure 4.17. The predominant γ phase peak is in the (111) plane located at $2\theta \approx 39°$ for the walls built with the Al:Ti wire feed rate ratio of 0.80~1.12. In addition, increasing the ratio from 0.80 to 1.12 leads to more γ phase and less α_2 phase. However, there is no obvious change of the α_2 phase fraction when the wire feed rate ratio is further increased to 1.30.

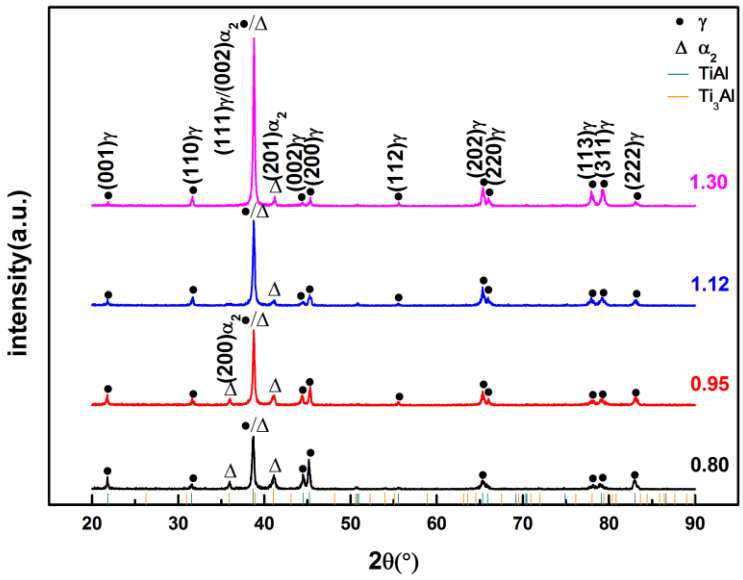

Figure 4.17 Phase constitutions in the wall components produced by GTAW-based ALM process under different wire feed conditions.

4.3.4 Effect of Processing Parameters on Microhardness

4.3.4.1 Effect of Arc Current on Microhardness

Figure 4.18 illustrates the mean microhardness value and standard deviation of the top region and near-substrate zone of the GTAW-based ALM produced walls using different values of arc current. It can be seen that consistently high microhardness values are recorded in the near-substrate zone for each wall specimen. Additionally, the results indicate that the average microhardness of the near-substrate zone is similar when built with arc currents ranging from 120 to 160 A, whereas increasing arc current can produce markedly harder material in the top region.

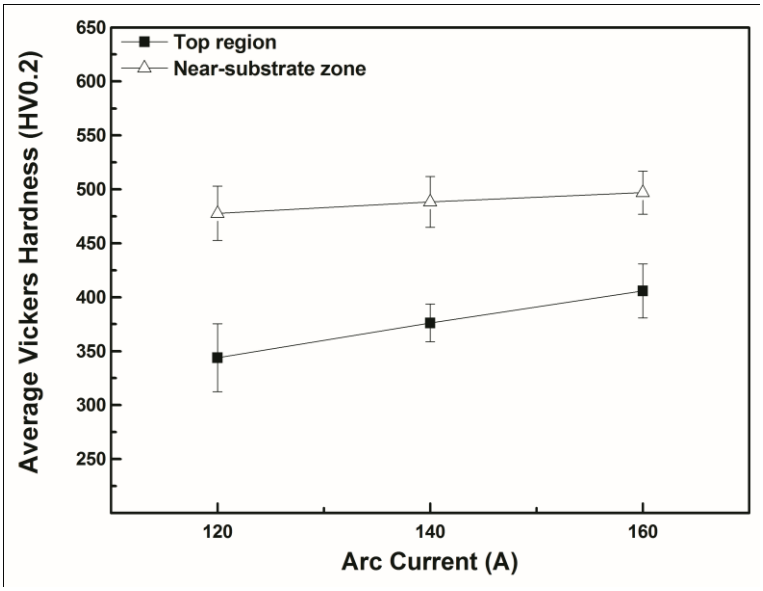

Figure 4.18 Mean microhardness values in different regions of wall components produced by GTAW-based ALM process using different arc current. Error bars show one standard deviation.

4.3.4.2 Effect of Interpass Temperature on Microhardness

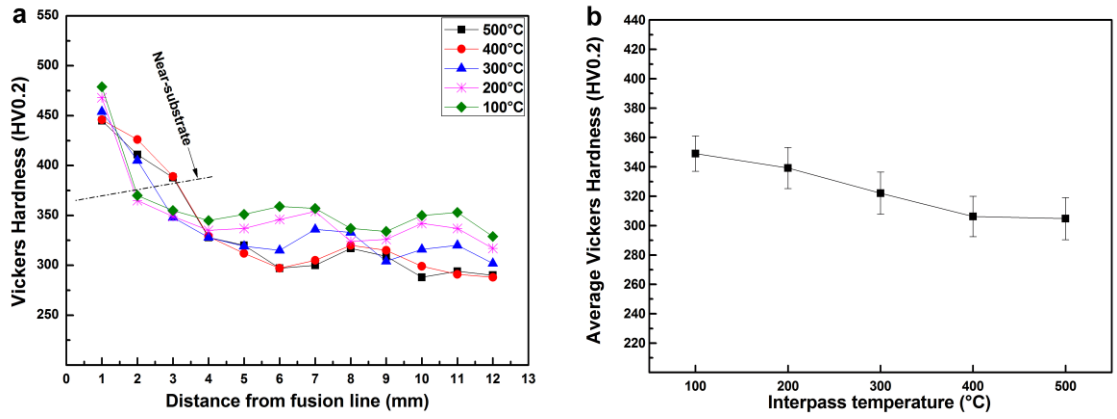

Figure 4.19 Microhardness values on the cross-sections of the GTAW-based ALM produced walls experiencing different interpass temperature: (a) Microhardness profiles as alongside the centreline, and (b) Mean microhardness values of the majority region except the near-substrate zone. Error bars show one standard deviation.

The microhardness profiles in the cross-sections and the average values in the majority region of all the GTAW-based ALM produced walls are presented in Figure 4.19. As shown in Figure 4.19a, all the specimens have similar microhardness distribution trends in relation to various interpass temperatures. The mean microhardness value (Figure

4.19b) of the majority region (i.e. excluding the near-substrate zone) reduces from 350 to 306 HV0.2 with increasing interpass temperature from 100 to 400 °C. There is no further decrease in microhardness as the interpass temperature is raised to 500 °C.

4.3.4.3 Effect of Wire Feed Rate Ratio on Microhardness

Figure 4.20 illustrates the microhardness profiles measured along the centreline of the GTAW-based ALM produced walls. It can be seen that high microhardness values are recorded in the near-substrate zone for each wall specimen. As the build-up continues, the microhardness is found to vary slightly depending on location. This is indicative of consistent wire feed ratio and uniform intermixing of elements during the build process. The exception to this occurs at the near-substrate zone, for the same reasons as described earlier.

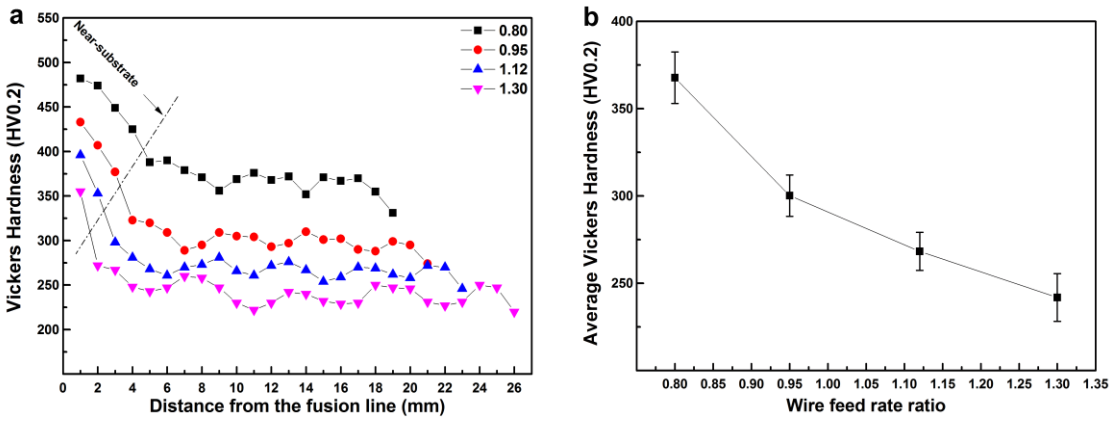

Figure 4.20 Microhardness values of wall components produced by GTAW-based ALM process under different wire feed conditions: (a) Microhardness profiles as a function of location on the cross-sections, and (b) Mean microhardness values of the majority region except the near-substrate zone. Error bars show one standard deviation.

In addition, the mean microhardness value and standard deviation of the majority region of the wall (except the near-substrate zone) for each GTAW-based ALM produced wall are shown in Figure 4.20b. The results indicate that reducing the Al:Ti wire feed rate ratio from 1.30 to 0.80 can produce significantly harder materials.

4.4 Discussion

Engineering titanium aluminide alloys based on the γ phase usually have 44~48 at.% Al. According to the binary Ti-Al phase diagram (Figure 2.2), these structural materials contain the γ phase with a tetragonal $L1_0$ structure and minor fractions of α_2 phase with the hexagonal $D0_{19}$ structure. The microstructure features can be directly attributed to the complex thermal history [170] that is implicit in the GTAW-based ALM process, rather than indirectly related to processing parameters such as arc current, interpass temperature and wire feed rate ratio.

The process used in this study has many similarities to a multipass arc welding process. Solidification microstructures during the initial welding passes generally exhibit epitaxial growth from the adjacent melted substrate. The preferential direction of grain growth is almost perpendicular to the solid/liquid interface, as this is the direction of the maximum temperature gradient during solidification. Meanwhile, a high cooling rate is expected due to chilling by conduction into the relatively colder substrate (even though it may be preheated). Therefore, the formation of α_2 grains in the near-substrate zone is not only the result of more Ti contents but also the consequence of the ordering transformation $\alpha \rightarrow \alpha_2$, while the high temperature transformation ($\alpha \rightarrow \alpha+\gamma \rightarrow \alpha_2+\gamma$) is suppressed by a high cooling rate [162]. Owing to the multiple heating and cooling cycles during the deposition of subsequent layers, the near-substrate zone is held at a higher temperature for a longer time due to heat flux from the recently deposited higher layers. In this case, the α_2 grains are coarsened and mostly equiaxied. As the build-up continues, the top region of the previous layer is partially remelted every time a new layer is deposited on top of the existing layer. In comparison to the equilibrium phase diagram, the rapid solidification proceeds according to the metastable extension of the α+L or γ+L phase boundaries as shown in Figure 4.21 [171]. The nucleation of primary phase must be suppressed by the second phase formation, which need only little undercooling. When cooling down to the peritectic temperature, the pro-peritectic phase

reacts with the melt L and forms the peritectic phase. Because the resulting peritectic phase envelops the pro-peritectic phase, further growth of peritectic phase is controlled by solid-state-diffusion. The enrichment of Al due to the incompleteness of the peritectic reactions is primarily distributed at the interdendritic regions, which then solidifies as the interdendritic γ phase at lower temperatures [172]. In addition, solid state phase transformations inevitably occur in the heat affected zone around the melt pool and ultimately lead to the formation of the fully lamellar microstructures together with interdendritic γ phases [129]. Since the near-surface zone of the as-fabricated wall is hardly affected by the heat, the much more and finer interdendritic γ grains are observable.

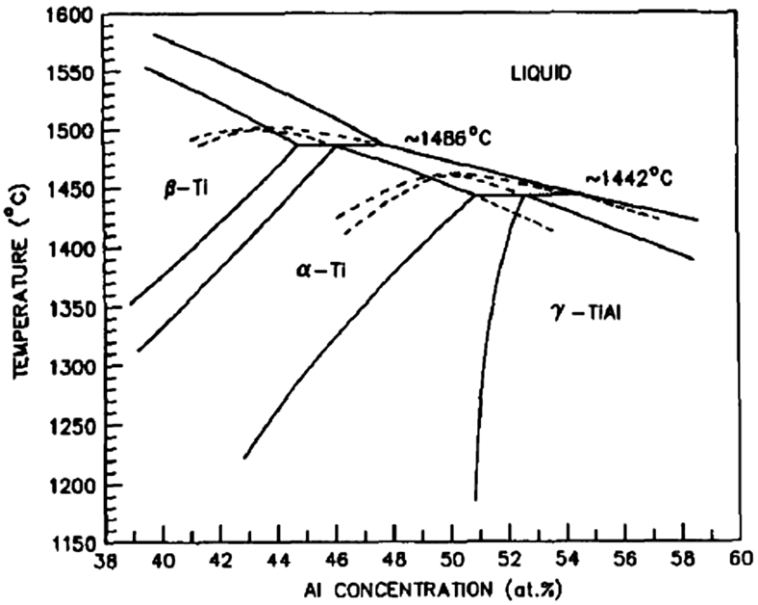

Figure 4.21 Partial equilibrium Ti-Al phase diagram including metastable extension of α+L and γ+L fields (dash lines) [171].

4.4.1 Effect of Arc Current

Based on the foregoing results, the arc current is an influential factor in changing the Al content in the near-substrate zone through changing the dilution area, and further affecting the phase fraction in the as-fabricated materials. As the arc current increases, the volume fraction of the α_2 phase increases in the near-substrate zones accompanied by a decrease in γ phase in the same zone due to the decreasing Al proportion.

Particularly on the 160 A produced materials, the extremely low Al content of the near-substrate zone is in pure α_2 phase field. It has been reported by Goken et al. [173] that the α_2 phase is considerably harder than the γ phase in the case of polysynthetically twinned (PST) crystals. As a consequence, the highest microhardness values are expected to be found in the near-substrate zone for the wall sample built with arc current 160 A. In addition, a slight microhardness variation is obtained in samples produced with different arc currents. Choi et al. [170] have stated that the volume fraction of different phases is controlled by the aluminium content and also strongly influenced by heat treatment and cooling rate, which is implicit in the GTAW-based ALM process. The molten metal is as known to be chilled by conduction into the colder substrate during initial weld passes. The resultant high cooling rate is another key factor that controls the high proportion of α_2 phase in the near-substrate zones. Therefore, the combinational effect of Al content and high cooling rate results in the similar microshardness values in the near-substrate zones, and further determines the microhardness variation as a function of different regions in each wall.

However, there is significant difference in the microhardness values in the top regions when increasing the arc current from 120 to 160 A, although the composition is similar. Generally, higher arc current leads to higher heat input and hence longer solidification time for the molten metal. Due to the lower cooling rate, the amount of microsegregation that is found in the alloy fabricated with higher arc current (160 A) is significantly less than that found in the alloy produced with lower arc current (120 A). Therefore, the strong increase in microhardness value when using 160 A arc current should be attributed to the reduced presence of interdendritic regions.

4.4.2 Effect of Interpass Temperature

The interpass temperature is related to the amount of energy that is still in the metal prior to the next layer being deposited. The assumption of the effect of a higher interpass temperature is similar to using a higher heat input. Consequently, a slightly

larger dilution area is expected due to higher interpass temperature. Although the microstructure features are dependent on the thermal cycle that the sample undergoes throughout the GTAW-based ALM process [126, 174], the interpass temperatures used in the present study are not high enough to change the solidification path for a given composition according to the phase diagram (Figure 2.2).

Additionally, changing the interpass temperature leads to a change in the phase fraction and further influences the microhardness values. Where the interpass temperature is greater it will allow more time for the sample to cool down to the required temperature for the next welding pass. As such, higher values of interpass temperature can provide a lower cooling rate. Generally, a high cooling rate encourages formation of α_2 phase [163, 175], which has a significantly higher hardness value than γ phase [173]. In engineering γ-TiAl alloys, a small α_2 phase fraction plays a beneficial role in the structure and properties. However, considerably more α_2 phase fraction has detrimental effects on the alloys [53]. In the present study, lower interpass temperatures of 100~300 °C produce significantly more α_2 phase fraction than higher interpass temperature (Figure 4.15b). In addition, lower interpass temperatures are expected to result in higher residual stresses within ALM components, particularly within large items. It is interesting to note that no significant difference in the volume fraction of phases and microhardness is found between the higher interpass temperature of 400 and 500 °C. This may be attributed to the diminishing effect on cooling rates that are produced at elevated interpass temperatures. If so, further increases in the interpass temperature will not significantly alter the α_2 phase content, but it will introduce more difficulties and costs in the manufacturing process due to the unnecessarily higher heat fluxes that need to be managed within the equipment. Therefore, 400 °C is chosen as a suitable interpass temperature for our future studies in applying the GTAW-based ALM process to titanium aluminide.

4.4.3 Effect of Wire Feed Rate Ratio

As would be expected, the wire feed ratio generally dictates the proportion of Al in the as-fabricated materials. But more interestingly, the wire feed ratio can produce an appreciable variation in the proportion of the two different phases. This phenomenon can be expected based on the phase diagram as discussed earlier. However, it is interesting that further increasing the ratio to 1.30 does not reduce the proportion of α_2 phase. It should be noted that the variations in the feeding rates of a filler metal applied to a weld might result in different arc lengths and, hence, different arc voltages. That variation directly affects the heat input. A higher total wire feed rate requires more energy to melt the filler metal, so less energy is available from the arc for melting of the weld pool and heating of the surrounding material. This effect should result in a relatively lower cooling rate. In this case, both the ordering transformation $\alpha \rightarrow \alpha_2$ and the high temperature transformation ($\alpha \rightarrow \alpha+\gamma \rightarrow \alpha_2+\gamma$) occur together. As a consequence, no visible change in volume fraction of α_2 phase can be expected with a significant increase in the total wire feed rate.

Correspondingly, the microhardness values of the as-fabricated materials are strongly dependent on the Al content, which is determined by the wire feed rate ratio. As the Al content increases, the volume fraction of the soft γ phase increases accompanied by a decrease in the much harder α_2 phase. Therefore, the increased microhardness values of the low Al content result from the increased α_2 phase content. With respect to the microhardness variation as a function of location in each wall, the cooling rate is the key factor that controls the proportion of α_2 phase and further influences the microhardness values.

4.5 Conclusions

An innovative and low cost additive layer manufacturing (ALM) process has been used to fabricate γ-TiAl based alloy wall components. Gas tungsten arc welding (GTAW) is used as the heat source for this new approach, combined with in-situ alloying through separate feeding of commercially pure titanium and aluminium elements. Since γ-TiAl alloys are thermally very sensitive and various cooling rates can have a large difference on the structural properties, the arc current, interpass temperature and wire feed rate ratio are considered as key parameters that must be optimised to obtain desired properties. Based on the results presented in this chapter, the following conclusions can be drawn:

1. Changing the arc current strongly affects the width and height of the as-fabricated walls. The width shows an increasing trend while the average height per pass decreases with an increase in the arc current from 120 to 160 A.

2. By increasing the arc current from 120 to 160 A, more Ti is diluted from the substrate. Therefore, the increase of α_2 phase in the near-substrate zone can be attributed to the decrease of Al content and a high cooling rate due to chilling by conduction into the substrate during initial weld passes. As expected, the microhardness of the near-substrate zone is correspondingly decreased. However, the arc current has little effect on the Al content in the top region, whereas the microhardness values exhibit an obvious increase with increasing the arc current due to the decrease of interdendritic γ phase.

3. Interpass temperatures of 100 through 500 °C have no significant effect on chemical composition. The walls produced by the new ALM technique are mainly composed of γ phase and α_2 phase with minor fraction. The volume fraction of α_2 phase is reduced by increasing the interpass temperature to 400 °C. However, it did not present a practical benefit on the decrease of α_2 phase

fraction when the interpass temperature was further increased to 500 °C. The variation of microhardness value can be explained by the change of α_2 phase fraction with the interpass temperature. Therefore, the most appropriate interpass temperature is 400 °C in the new manufacturing method for γ-TiAl alloys.

4. The effect of the ratio between the Al and Ti wire-feeding rate has been investigated. With increasing the wire feed rate ratio from 0.80 to 1.30, Al content and γ phase increase, and microhardness decreases as expected. However, little volume fraction change of the α_2 phase has been found when the wire feed rate ratio is increased further to 1.30. The slightly lower cooling rate due to the higher total wire-feeding rate is considered to be the cause of this effect.

5. The results also show that the chemical composition is generally uniform throughout the as-fabricated walls, apart from the near-substrate zone. Therefore, uniform weld and material properties throughout the height of each wall can be expected. A key factor in this manufacturing technique is to precisely control the Al and Ti wire feeding rates in order to obtain the desired composition in the final materials.

5 Effect of Location on γ-TiAl Alloys Produced by the GTAW-based ALM Process

5.1 Introduction

Processing parameters including arc current, interpass temperature and wire feed rate ratio have been investigated on microstructure and microhardness in Chapter 4. For the GTAW-based ALM process, it is also important to understand the microstructural evolution and the variation of mechanical properties within one build in order to achieve components of acceptable quality, repeatability and reproducibility. A number of previous studies have reported the effect of distance from the build plate on the microstructure and microhardness variation within additively manufactured Ti-6Al-4V components produced using electron beam melting [176], laser-based process [177] and wire and arc based techniques [165]. However, no previous literature can be found to specifically study the effect of location on additively manufactured titanium aluminide alloys.

The current investigation concentrates on an innovative additive layer manufacturing approach for titanium aluminides. Microstructural features and mechanical properties of the fabricated components as a function of location are investigated and discussed, to understand the effectiveness of GTAW-based ALM process in producing titanium aluminide components with the desired properties.

5.2 Experimental Procedure

5.2.1 Investigated Materials

Based on the study of GTAW-based ALM processing parameters in Chapter 4, a current of 120A and 400 °C interpass temperature were used to fabricate titanium aluminide components for the investigations in this chapter. The Ti and Al wire feed rates were selected as 750 mm/min and 870 mm/min, respectively. Other parameters were kept consistent.

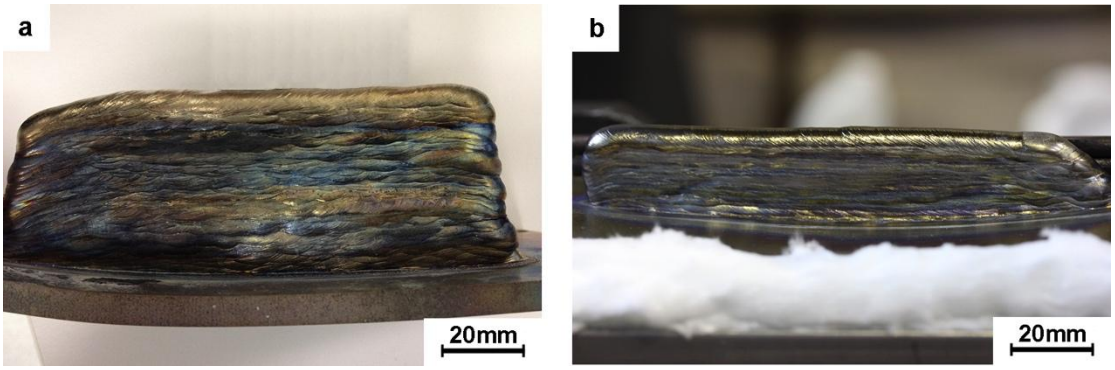

Figure 5.1 Examples of titanium aluminide components.

The deposited wall components (Figure 5.1) typically have a length of 100 mm and a width of 10 mm. Two build heights of 45 mm and 19 mm were produced, depending on the specimens required for testing.

(1) Set 1 refers to one component of 45mm height as shown in Figure 5.1a.

(2) Set 2 refers to three components of 19mm height as shown in Figure 5.1b.

All the deposited walls were wire-cut from the substrates, and the required specimens were subsequently wire-cut from the deposits.

5.2.2 Metallography

The metallographic specimens were prepared using standard procedures for titanium aluminides. The microstructure and element distribution in the different regions of the

etched specimens were investigated by SEM/EDS, operating at a voltage of 20 kV and working distance of 10 mm. The accuracy of EDS measurements is ± 0.5 at.%. XRD measurements were carried out to identify the phase constitutions.

5.2.3 Microhardness Testing

In order to investigate the possible influence of location on hardness within the component, the indentations were started from the interface between substrate and deposited wall, progressed along the vertical centre line parallel to the build direction (Z) in cross-section (X-Z plane), and continued to the top in the last layer of the deposited wall in 0.5 mm intervals. Hardness in the lateral direction (X) perpendicular to the centre line was also measured in the near-substrate zones, layer bands and top regions separately. In addition, microhardness measurements were performed parallel to the travel direction (Y) in the longitudinal section (Y-Z plane) of the deposited walls. The location of the indentations and orientation of the reference axes are shown in Figure 5.2.

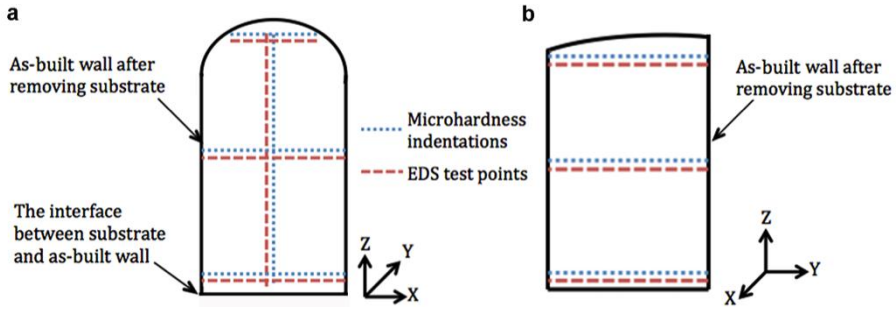

Figure 5.2 Schematic showing the locations of microhardness and EDS measurements in different sections of γ-TiAl based wall components produced by GTAW-based ALM process: (a) cross-section (X-Z plane), (b) longitudinal section (Y-Z plane).

5.2.4 Tensile Testing and Fracture Surface Analysis

Two sets of room-temperature tensile properties of the deposited materials were measured in order to evaluate how the direction and location influence the tensile properties. All tensile tests were performed on a MTS370 load unit at a strain rate of

0.05 s^{-1}. Fractography analysis of the broken tensile samples were conducted on SEM. Figure 5.3 indicates the direction and location of all the tensile specimens, with the shape and dimension of the specimen being shown in Figure 3.11.

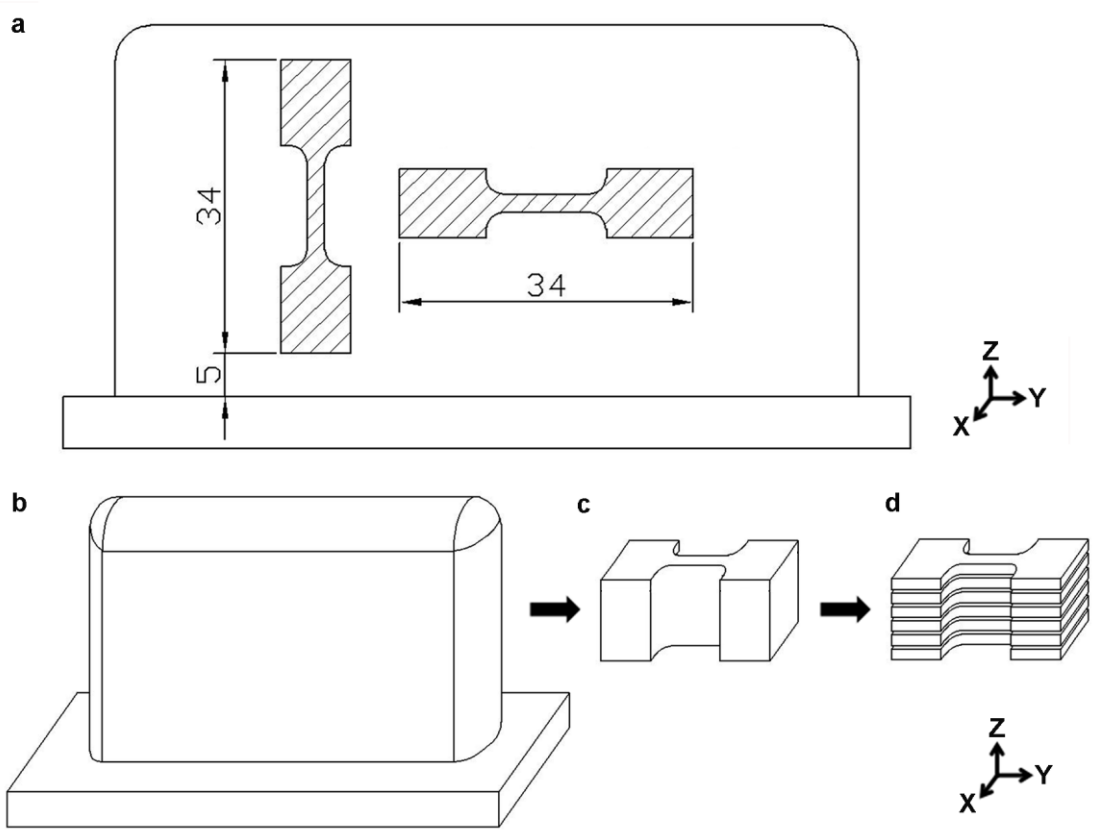

Figure 5.3 Sample orientations and dimensions for room temperature tensile tests: (a) sample orientation and designation of directions, units are in mm, (b) GTAW-based ALM deposited wall component, (c) bulk tensile sample cut from the centre of deposit, (d) tensile specimens after slicing bulk sample.

(1) In the first set of tests that perform a direct comparison between the properties in the two orientations (the vertical build direction (Z) and longitudinal direction (Y)), three specimens for each orientation were produced from Set 1 component as shown in Figure 5.3a.

(2) In the second set of tests to assess the consistency of mechanical properties throughout the height of the fabricated wall, 10 specimens were cut from each

component in Set 2 as shown in Figures 5.3b, 5.3c and 5.3d at controlled heights to produce a total of 30 specimens.

5.3 Results

5.3.1 Morphology and Microstructure

The typical macrostructure of a cross-section (X-Z plane) and a series of optical micrographs from different regions along the vertical centreline (Z direction) are shown in Figure 5.4. Apart from two small areas at the top and bottom of the component respectively, the macrostructure exhibits strong columnar grains oriented upwards, parallel to the build-up direction, which is the direction of heat flow. A series of layer bands can be readily observed in this region. This phenomenon is well documented in a number of studies on different ALM processes that have been referenced in section 1. The optical micrographs clearly show that there are significant changes of microstructure in different regions. Large equiaxed α_2 grains are found in the near-substrate zone, shown in Figure 5.4d. Some fine, irregularly shaped γ laths displaying more contrast variation precipitate at the grain boundaries. The diameters of the α_2 grains are in the range of 50~150 μm.

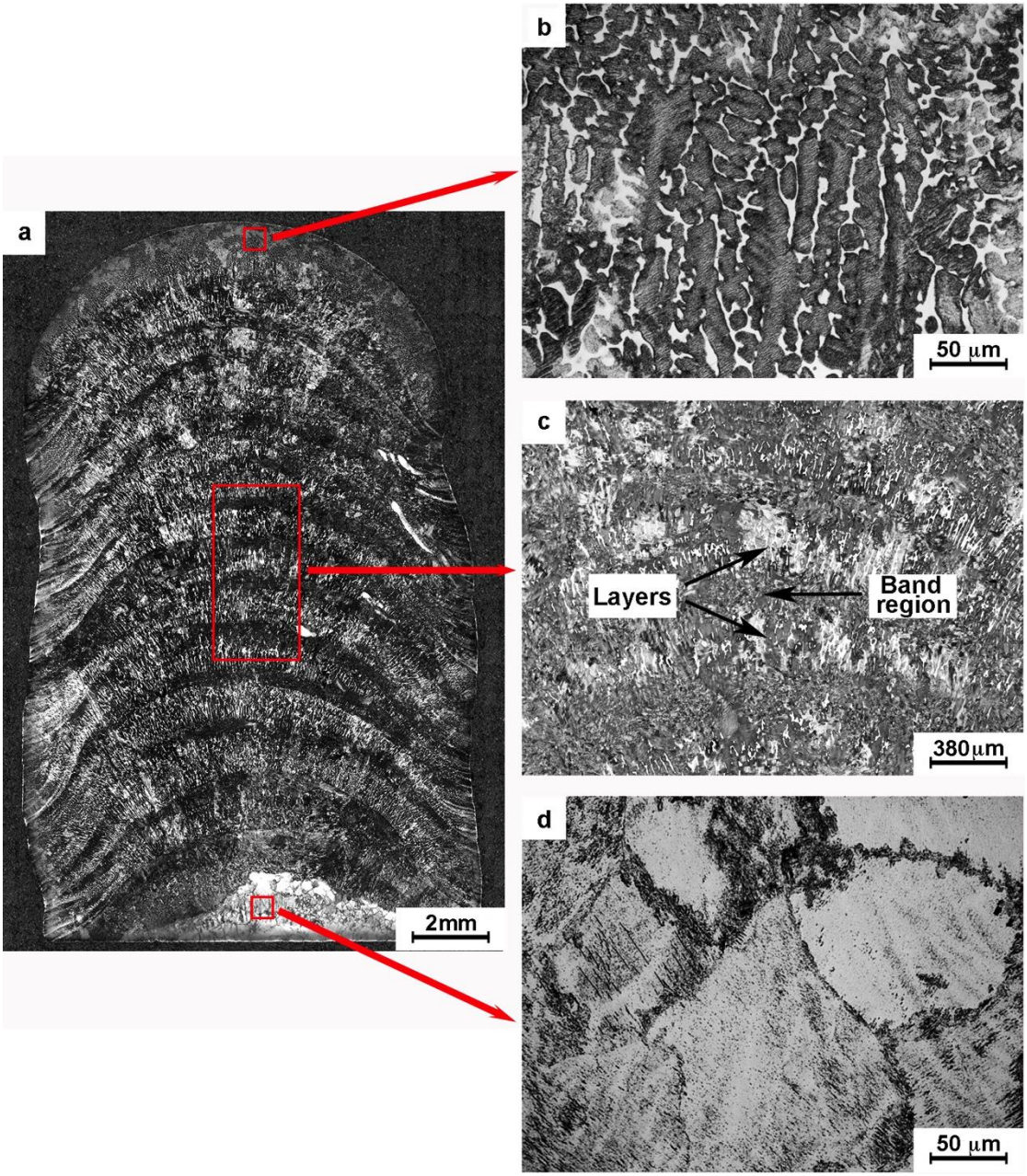

Figure 5.4 Morphology and microstructure in cross-section (X-Z plane) of γ-TiAl components produced by GTAW-based ALM process: (a) cross-section (X-Z plane) morphology, (b) representative microstructure in the top region (c) morphology of the layer bands, and (d) representative microstructure in the near-substrate zone.

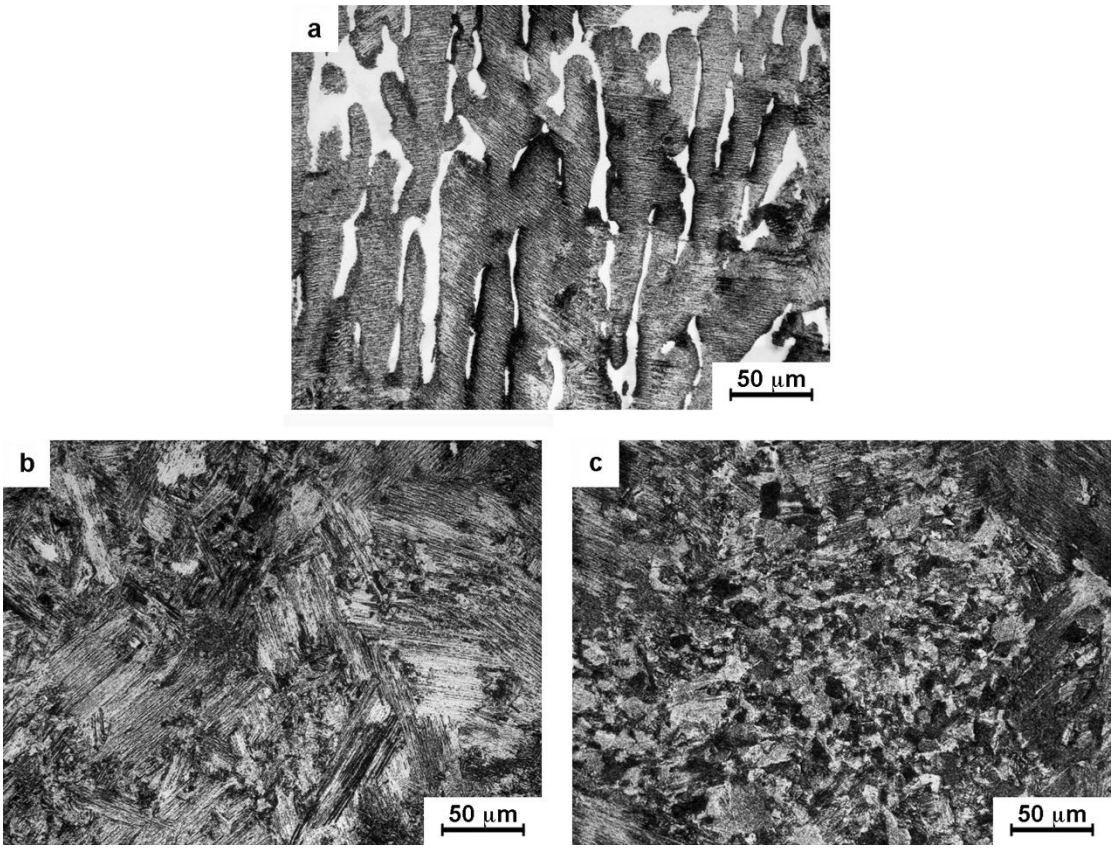

Figure 5.5 Representative microstructure of layer bands in cross-section (X-Z plane) of γ-TiAl components produced by GTAW-based ALM process: (a) microstructure observation in the layer (marked as "Layers" in Figure 5.4c), (b) and (c) microstructure observations in the band region (marked as "Band region" in Figure 5.4c).

Above the near-substrate zone, optical contrast caused by different microstructure shows the formation of layer bands (Figure 5.4c). The sequential layer bands appear to be perpendicular to the build direction (Z) owing to high temperature and heat conduction along the travel direction (Y). Brandl et al. (2012) [125] have stated that the layer bands do not coincide with the layers deposited. The number of layer bands is generally less than the number of layers deposited. In the case of components shown here, 20 layers have been deposited while approximately 13 layers can be identified. A band region of approximately 190 μm thickness can be found between any two layers. Detailed observation of the microstructure (Figure 5.5) shows that interdendritic phases surrounded by lamellar microstructure are observed in each layer (Figure 5.5a), while fully lamellar colonies with different colony sizes consisting of α_2 and γ lamellae

content are found in the band region (Figure 5.5b and 5.5c). Duarte et al. [178] describe similar microstructures in γ-based TiAl cast alloys.

The microstructure seen in the top region (Figure 5.4b) is relatively fine and consists of long dark dendrites and white interdendritic phases. Similar microstructures have been observed in titanium aluminide welds produced by both laser [179] and GTAW [162]. The lamellar character of the dendritic structure and the interdendritic regions are revealed at higher magnification (Figure 5.6).

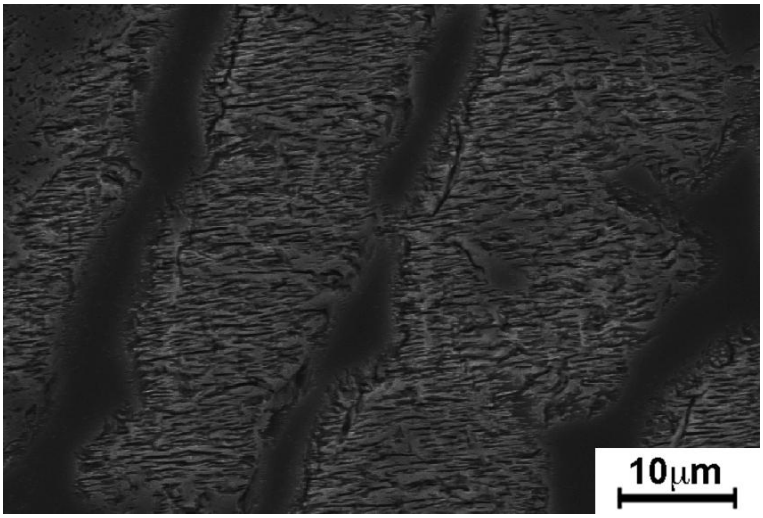

Figure 5.6 High magnification SEM image showing microstructure in the top region of cross-section (X-Z plane) of γ-TiAl components produced by GTAW-based ALM process.

5.3.2 EDS Analysis

The results of microchemical analysis at test locations specified by Figure 5.2 are summarised in Figure 5.7. All EDS measurements were performed either alongside or below the hardness measurement points at approximately 0.1 mm distance. It can be seen that the Al distribution is comparatively homogeneous in the layer bands, where there are small fluctuations in the measurements between 43 at.% and 46 at.% Al. However, among the layer bands, the Al content is slightly higher in the layers than the content in the band regions. Predictably, the Al concentration is lower in the near-

substrate zone adjacent to the pure Ti substrate. The particularly higher concentration of Ti in the central area of the near-substrate zone also appears as the bright microstructure in Figure 5.4d. In the top region, the highest Al concentrations are detected, and large deviations of Al concentration are observed. This can be attributed to Al segregation on solidification and no further heat treatment or temperature cycling, as no subsequent layers are deposited. A line profile (Figure 5.8) taken across three dendrite arms in the top region of one specimen shows the Al enrichment in the interdendritic phases.

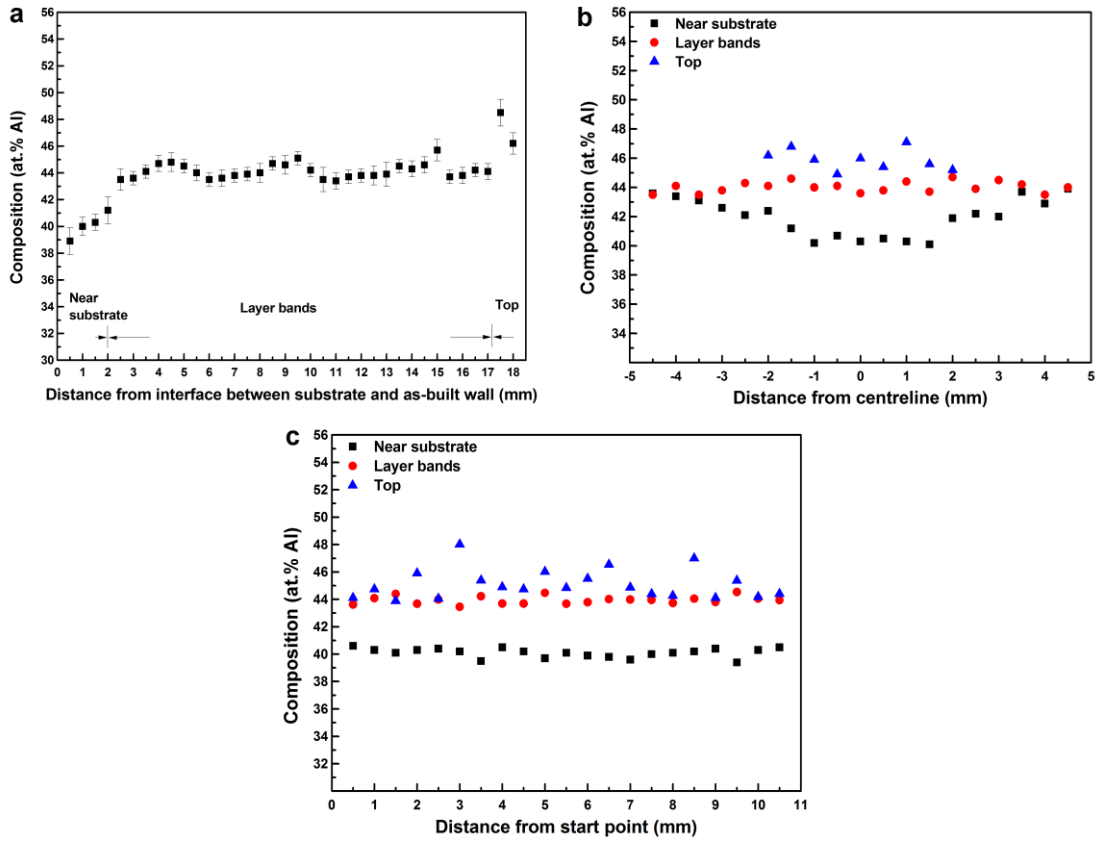

Figure 5.7 Quantitative concentration of Al obtained by EDS from cross-section (X-Z plane) and longitudinal section (Y-Z plane) of γ-TiAl components produced by GTAW-based ALM process: (a) along the build-up direction (Z) in cross-section, (b) across the build-up direction (X) in cross-section, and (c) along the travel direction (Y) in longitudinal section. Each data along different direction was averaged as a result of three measurements on 3 samples. Error bar means one standard deviation. The variation of 0.5~1 at.% in Al content for each point was obtained from the calculated standard deviation.

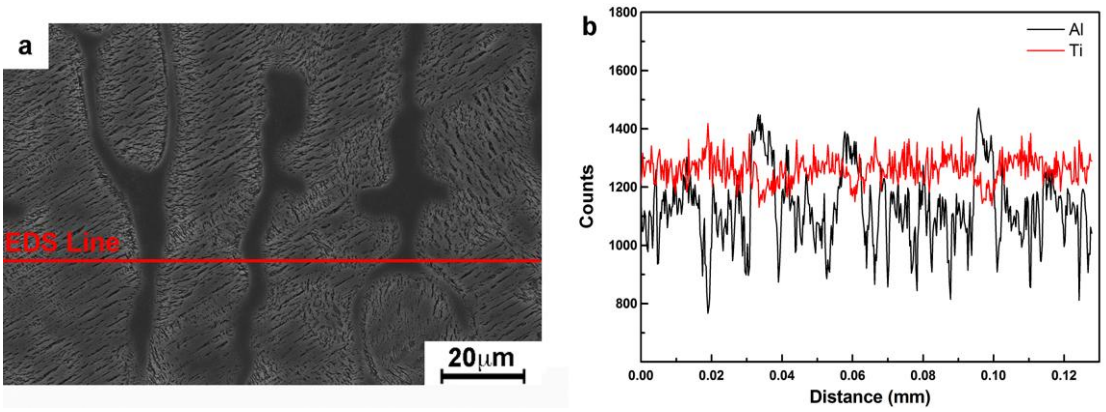

Figure 5.8 The distribution of in-situ alloyed elements in the top region: (a) the position of EDS line scan test, and (b) the corresponding line profile showing Al enrichment within interdendritic phases.

Correspondingly, the microchemical composition of various microstructures contained within the different regions was identified by EDS analysis, as recorded in Table 5.1 Lamellae in the top region have an average Al content of around 43.8 at.%, while a similar Al content can be found in lamellar structures within the layer bands. The interdendritic phase with higher Al content of around 48.7 at.% is found in the top region. In addition, the interdendritic phases have comparable Al distribution throughout the entire component.

Table 5.1 Microchemical composition of γ-TiAl components produced by GTAW-based ALM process, determined by EDS. The mean composition of different microstructure and their standard deviation were calculated by the results of five measurements for each structure in the same region.

Microstructure	Microchemical Composition, at.%	
	Ti	Al
Lamellae in the layer bands	56.2±0.3	43.8±0.3
Interdendrites in the top region	51.3±0.3	48.7±0.3
Lamellae in the layer bands	55.9±0.3	44.1±0.3
Interdendrites in the layer bands	52.1±0.2	47.9±0.2
Equiaxed α_2 grains in the near-substrate zone	59.8±0.2	40.2±0.2

5.3.3 Phase Identification

In order to identify the phase structure, an XRD analysis was conducted in cross-sections of components produced by the GTAW-based ALM process. A comparison of the XRD data from different regions of a cross-section is shown in Figure 5.9. All of the diffraction patterns are found to contain a prominence of γ phase at approximately 39°, which includes both the γ lamellae and the observed interdendritic γ grains. The γ phase peaks of the top region are markedly stronger than those of the other regions. The layer bands are characterised by peaks of γ and α_2, although only a very small amount of α_2 phase can be found. In comparison to the other areas, the volume fraction of γ phase decreases in the near-substrate zone accompanied by a dramatic increase of α_2 phase. This phenomenon is further confirmed by different amounts of α_2 phase in different regions (Figure 5.9b). The near-substrate zone has an extremely high α_2 phase volume fraction of 52±3 %.

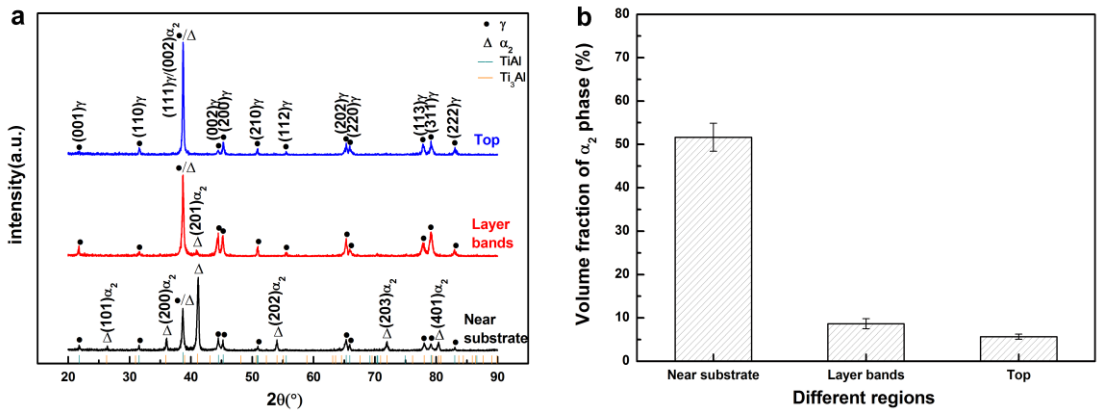

Figure 5.9 Phase constitutions of different regions in cross-section of γ-TiAl components produced by GTAW-based ALM process: (a) XRD diffraction patterns. Three experiments were performed on each region, and (b) Average volume fraction of α_2 phase. The results were obtained by Rietveld analysis on the three experiments in (a), and error bar shows one standard deviation.

5.3.4 Microhardness Measurements

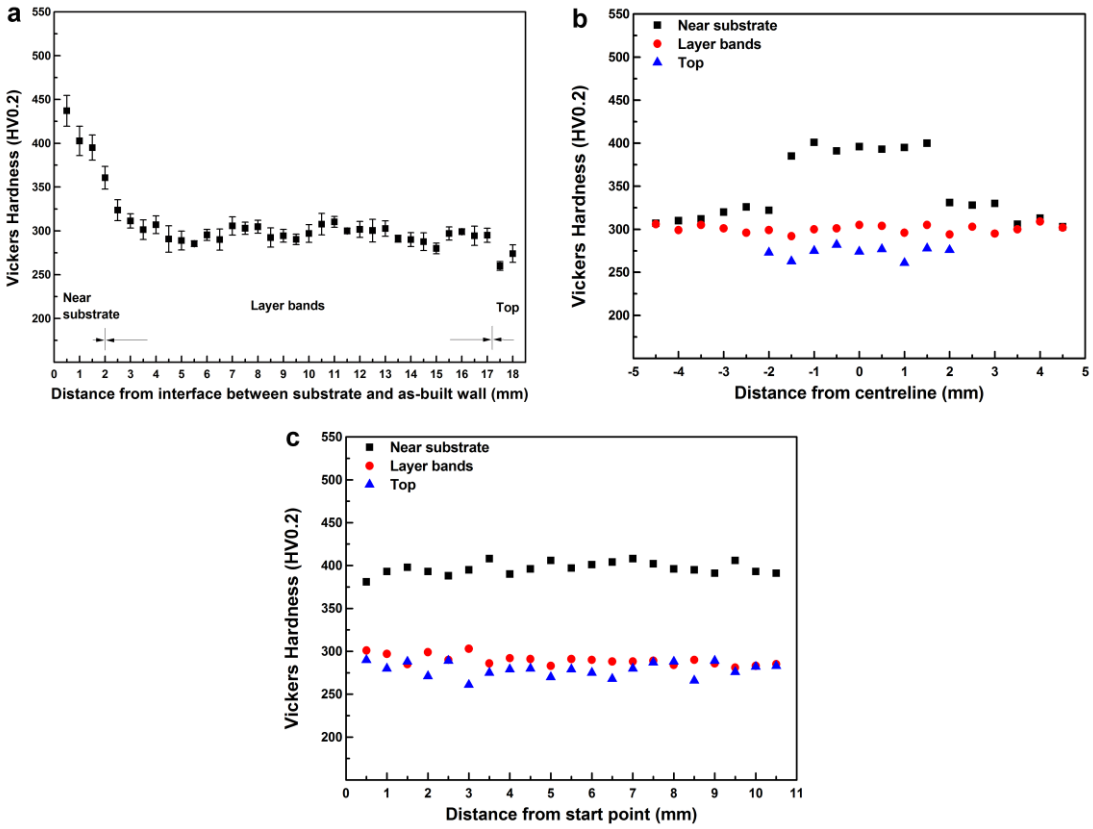

Figure 5.10 Microhardness profile as a function of location in cross-section (X-Z plane) and longitudinal section (Y-Z plane) of γ-TiAl components produced by GTAW-based ALM process: (a) along the build-up direction (Z) in cross-section, (b) across the build-up direction (X) in cross-section, and (c) along the travel direction (Y) in longitudinal section. The presented results for each direction are mean values calculated from 3 measurements of 3 samples. Error bar shows one standard deviation that is in the acceptable range of 3~13 HV0.2 for each data point, while the maximum deviation is found in the top region.

Microhardness (HV0.2) values versus location are plotted in Figure 5.10. The microhardness appears to be relatively homogeneous within the layer bands, ranging from 287 to 323 HV0.2. The mean microhardness value is 296 HV0.2 when measured in the layer bands together with the top region, despite the slight fluctuation in the top region due to segregation. The central area of the “inverted bowl shape” in the near-substrate zone (Figure 5.10b) is much harder than the outer areas near the wall surface. These results correlate with the microstructural observations and the microchemical

distribution measurements. It is interesting that the highest microhardness value of 437 HV0.2 is found in the first few layers of near-substrate zone, rather than in the centre of laser-melting deposited plates as described by Qu and Wang [129]. The difference could be attributed to different morphology and microstructure. This will be discussed further in section 5.4.1.

5.3.5 Tensile Properties

The room temperature tensile properties of the deposited material in the vertical build direction (Z) and longitudinal direction (Y) are summarised in Table 5.2. Three test specimens were used for each orientation. The specimens tested in the Y-direction are found to have higher ultimate tensile strength (UTS) and yield strength (YS) than those tested in Z-direction. However, there is no observable difference in Elongation (% EL).

Table 5.2 Comparison of the mechanical properties of γ-TiAl components produced by GTAW-based ALM process, tested along the build-up direction (Z) and the travel direction (Y). The results including the average value and their standard deviation were calculated from 3 specimens for each direction.

Direction	Ultimate tensile strength, MPa	Yield strength, MPa	Elongation, %
Longitudinal/travel direction (Y)	549±23	474±17	0.5
Vertical/build direction (Z)	488±50	424±30	0.5

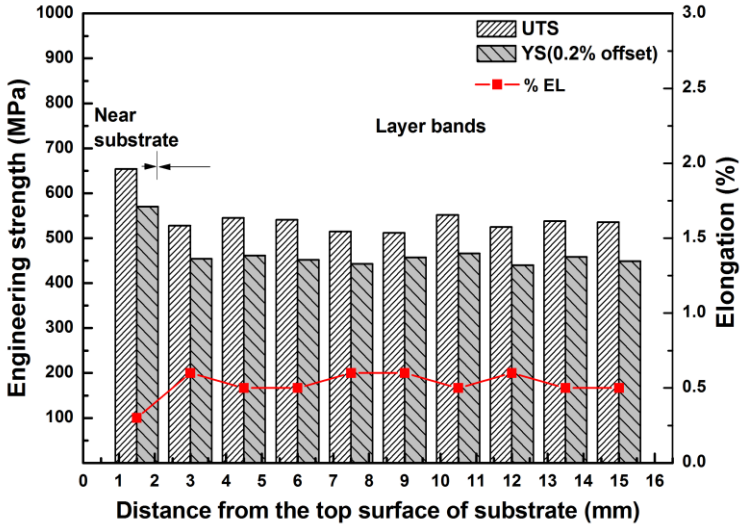

Figure 5.11 Location effect on mechanical properties of γ-TiAl components produced by GTAW-based ALM process. Testing performed in longitudinal/travel direction. Each data point represents the average of 3 tests, corresponding to the 3 wall samples that were produced. The variation in strength within each group of 3 does not exceed 20 MPa, while the variation in ductility is approximately ±0.1 %.

Figure 5.11 shows the effect of vertical location (in the build direction, Z) on the mechanical properties, as measured in the longitudinal (Y) direction. The near-substrate zone of the deposited wall exhibits the highest UTS and YS and the lowest ductility. However, no significant variation in tensile strength is found due to the location of a sample within the layer bands. The average values of UTS and YS in the layer bands span 512~552 MPa and 443~466 MPa, respectively. Additionally, the elongation is also almost identical within this area. The consistency of these test results is in agreement with the regularity of microhardness measurements according to the location in the Z-direction (Figure 5.10).

Representative fracture surfaces of the tensile samples are shown in Figure 5.12. The fracture morphologies of tensile tested samples are quite similar for different sampling regions. All samples show predominantly transgranular cleavage fracture over the entire fracture surface. The fracture surfaces of the samples from the near-substrate zone show some secondary cracks, which cannot be found in the samples from layer bands. In all cases, the fracture modes are brittle fracture, and no dimples are observed.

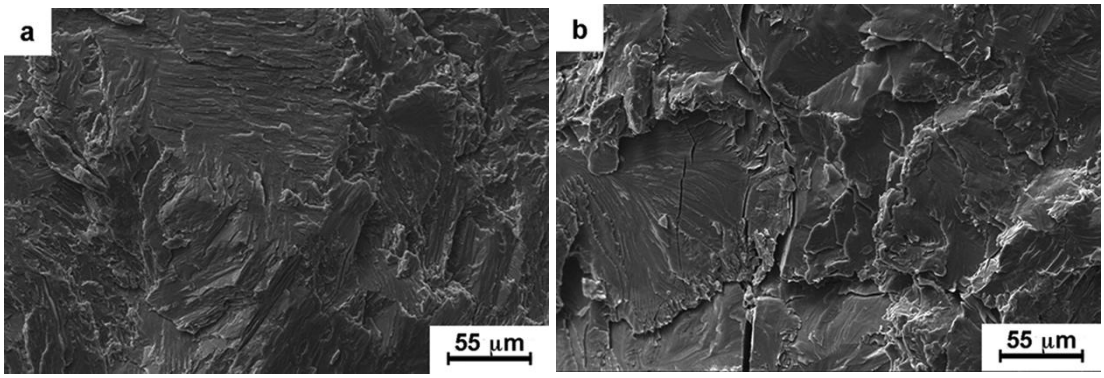

Figure 5.12 SEM fractographs in different regions of γ-TiAl components produced by GTAW-based ALM process: (a) layer bands, and (b) near-substrate zone.

5.4 Discussion

5.4.1 Morphology and Microstructure

The ALM fabrication technique used in this work has many similarities to a multipass arc welding process. During the initial welding pass, many processes take place simultaneously: (i) melting of the constituent ALM elements and also the surface of the substrate; (ii) formation of the main phases, that is, titanium aluminide; (iii) alloying of the main phases, such as TiAl; and (iv) solidification of the different phases. Therefore, immediately below the fusion zone, small β grains present in the pure Ti plate revert to a fully β structure and undergo rapid grain growth. The solidification front epitaxially grows back from these coarsened β grains, which act as nucleation sites at the edge of the fusion boundary, into the weld pool where each growing grain forms as a continuation of the grains that lie along the fusion boundary [126]. When solidification occurs following a moving melt pool, the preferential grain growth direction is perpendicular to the curved surface of the solid/liquid interface in order to follow the maximum temperature gradient. The steepest gradient provides the maximum driving force for solidification, as is commonly observed in ALM-produced Ti-6Al-4V products [124].

As the build-up progresses away from the substrate, the upper region of the previously deposited layer is partially remelted by the subsequent layer which is deposited on top of the existing layer. As a result, the grains in this region serve as nuclei in the subsequent layer and grow from the previously coarsened grains. When the build-up continues, the unidirectional heat flow characteristic of the additive layer manufacturing process contributes to the columnar grains that develop up through the entire sample. The formation of layer bands can also be attributed to the partial remelting of previously deposited layers and multiple thermal cycles that have occurred with each subsequent deposition pass. A detailed explanation of the layer bands can be found elsewhere. Kelly and Kampe [120] found that the layer bands and gradient morphologies are a result of the complex thermal history experienced by the build material and not a result of segregation or oxidation. The layer bands reflect the beta transus temperature T_β rather than the solidus temperature T_s or liquidus temperature $T_{L,}$ as proposed by Brandl et al. [125]. Liu et al. [180] have suggested that layer bands are heat-affected zones, which result from the sub-melting-point reheating treatment when a new layer is deposited.

Furthermore, solidification takes place solely through β phase for alloys containing less than 45 at.% Al based upon the phase diagram (Figure 2.2). Microsegregation for such alloys is significantly lower than predicted by the Gulliver-Scheil equation [181, 182]. This indicates backdiffusion in β phase and solidification relatively close to equilibrium. As illustrated in Figure 5.7a, the near-substrate zone has around 40 at.% Al because of dilution from the pure Ti substrate that is mixed into the weld pool during deposition of the first layer. This effect is reduced as the next few layers are added, since the weld pool penetrates layers that have progressively lower Ti content. Thus, materials within the near-substrate zone are able to experience $\beta \rightarrow \beta+\alpha \rightarrow \alpha+\gamma \rightarrow \alpha_2+\gamma$ phase transition during solid state cooling because of the expectedly lower Al concentration. However, the microstructure seen in the near-substrate zone with around 40 at.% Al is indicative of a transformation from α to α_2 followed by precipitation of γ at some lower

temperature, as evidenced by the thermal APBs in the α_2 that were continuous on either side of the γ plates [183]. It is well known that the volume fraction of different phases is controlled by Al content and also strongly influenced by heat treatment and cooling rate [170], which is implicit in the GTAW-based ALM building process. As such, the high temperature transformation ($\alpha \rightarrow \alpha+\gamma$) is suppressed by the relatively high cooling rate during initial weld passes, and only the ordering transformation $\alpha \rightarrow \alpha_2$ occurs [162] which plays an important role in the formation of α_2 phase in the near-substrate zone.

In contrast to the near-substrate zone, $L \rightarrow \beta$ is not the only solidification route for the top region and layer bands, which have higher Al content at around 44 at.% Al. Because the co-existence of heavy and light metals in the Ti-Al system can still easily cause dendrite segregation, the remaining liquid progressively enriches in Al and then solidifies through the peritectic reaction $L+\beta \rightarrow \alpha$ [184]. The crystallographically oriented α grains form at L/β interfaces with orientation according to the Burgers' relationship $\{110\}_\beta \parallel (0001)_\alpha$ and $\langle 111\rangle_\beta \parallel \langle 11\bar{2}0\rangle_\alpha$ [27]. However, limited diffusion and melt undercooling that impede the formation of the pro-peritectic solid phase normally cause the incompleteness of peritectic reaction. The formation of γ grains in the interdendritic areas is mainly ascribed to the occurrence of $\alpha \rightarrow \gamma$ transition or nucleation directly from the β phases [185]. After solidification has been completed, different phase transformations are possible depending on the Al content and cooling velocity on moving out of the single phase α field. As such, upon further cooling the alloys either pass through the phase transformation $\alpha \rightarrow \alpha+\gamma \rightarrow \alpha_2+\gamma$ or the path $\alpha \rightarrow \alpha_2 \rightarrow \alpha_2+\gamma$. All γ lamellae precipitate from α or α_2 grains to form a lamellar structure according to the Blackburn's orientation relationship $(0001)_{\alpha_2} \parallel \{111\}_\gamma$ and $\langle 11\bar{2}0\rangle_{\alpha_2} \parallel \langle 1\bar{1}0\rangle_\gamma$ [38, 186]. The solid state annealing of existing layers during the deposition of subsequent layers can result in further precipitation of γ laths in non-remelted areas, named as band region in this work. Therefore, a fully lamellar microstructure is obtained in the band regions, while the layers are indicative of

remelted material that consists of some interdendritic γ grains and coarse lamellar structure. Similar microstructure but more and finer interdendritic γ grains are consequently obtained in the top region that is not influenced by subsequent weld passes. It is interesting that the α_2 phase could not be readily found in the top region, especially the (201) main plane located at $2\theta \approx 41°$. However, it would be unreasonable to draw a conclusion that there is no α_2 phase in the top region. This is most probably caused by the limitations of X-ray diffraction. Usually XRD cannot detect a phase if it presents at less than 2~5 %. The weak intensity of α_2 peaks could be attributed to the ultrafine α_2 lamellae.

5.4.2 Mechanical Properties

It is well known that mechanical properties in metallic materials are strongly dependent on grain or colony size, dislocations and boundaries, solid solution elements and precipitates. In the case of titanium aluminides, there are several competing effects regarding the strength.

Firstly, hardening mechanisms in metallic materials are generally explained in terms of grain boundaries, domain boundaries and lamellae interface. The mean grain/lamellar colony size has been demonstrated to significantly control a range of mechanical properties in γ-based alloys [2]. However, in most investigations of TiAl alloys with α_2+γ lamellar structure, the strength is ordinarily described as a function of the mean interface spacing. The interaction between interfaces and dislocation motion can be used to interpret their dependency relationship [187]. Investigations by Dehm et al. [188] have shown that the movement of dislocations in the γ phase governs mechanical properties when mean interface spacing is more than 100 nm. The high interface density can distinctly improve the mechanical properties since the slip of dislocations can be hindered by interfaces comprising γ/α_2 and γ/γ.

Secondly, the Al level in binary alloys determines the initial phase to precipitate and the subsequent phase transformations that occur on solidification. The mechanical properties of γ-TiAl based alloys can be controlled not only by the γ phase but also by the α_2 phase. Consequently, the volume contents of the γ and α_2 lamellae and also their mean widths should be taken into account. In the case of polysynthetically twinned (PST) crystals [173], a significant difference in hardness has been found between γ and α_2 phases. The hardness of γ phase is almost half that of α_2 phase. The increased strength of the lower Al content titanium aluminide alloys is likely to result from the increased α_2 phase content.

Nevertheless, Cha et al. [189] have reported that in γ-based TiAl alloys with ultrafine α_2+γ lamellar structures, the strength is determined by both the volume fraction and lamellar thickness of the two phases. On the one hand, when the volume fraction of α_2 phase is dominating, the α_2 phase, especially the width of α_2 laths, is the primary factor affecting the strength of lamellar colonies. On the other hand, the strength of titanium aluminides having a lamellar structure can be enhanced under the significant influence of nanometre-sized γ laths and their volume fraction. Generally, if the width of the laths is too small to allow dislocations to move or even to be generated, the strength is expected to be extremely high and most likely constant [190]. Therefore, the small size of γ laths acts as the obstacle for dislocation movement, to make the ultrafine γ lamellae harder than the much wider α_2 lamellae. It should be noted that theoretical hardness of the individual γ and α_2 phase could be obtained in the nano-scale region, and the strength of lamellar structure in titanium aluminides accordingly depends on the volume contents of both the nanometre-sized γ and α_2 laths.

In addition, the different orientation of γ lamellae should be taken into account when discussing the obtained strength. Strength variations were observed by Sato et al. [191] between γ lamellae of different orientation with relatively large thickness. Very thin γ lamellae do not show reproducible strength variations.

With respect to the fabricated γ-based TiAl alloys in the current study, anisotropic tensile properties are expected for both directions owing to anisotropic microstructure. Crack nucleation sites tend to locate at the interface of layered microstructure. This leads to poorer tensile properties in the Z-direction. However, less interface and more homogenous microstructure along the Y-direction are conducive to superior mechanical properties in this direction. Considering the location effect in the Z-direction, Al content is the key factor that influences the strength. One hypothesis involves the change of stacking fault energy with composition. Calculations of interatomic potential and charge distribution have indicated that stacking fault decreases with decreasing Al content [192]. Besides, the volume fraction of γ phase decreases accompanied by an increase in α_2 phase when the Al content decreases. The critical resolved shear stresses for dislocations to glide in the α_2-Ti_3Al phase are considerably larger than those for activation of slip in γ-TiAl phase [193]. Furthermore, the higher cooling rates in components produced by the GTAW-based ALM process lead to more microstructures (α_2 phases), which have higher strength and hardness than in the case of lower cooling rates. Based upon this discussion, it is believed that higher volume fraction of α_2 structures (Figure 5.9b) results in considerably higher microhardness values, UTS and YS in the near-substrate zone. Although larger grains normally have lower strength because of the reduced number of boundaries and/or dislocations in the large-scale microstructure, the fine γ laths precipitated from the large α_2 grains could be obstacles to dislocation slip and hence the strength in the near-substrate zone could be improved.

Additionally, the temperature in the layer bands and top region of the fabricated wall is higher and more homogeneously distributed than that in the near-substrate zone, and hence, a softer and less heterogeneous material is obtained in these areas. However, the impact of multiple deposition cycles (i.e. multiple annealing cycles) on the strength of each layer and the band region between them cannot be seen clearly. A generally monotonic microhardness gradient throughout the vertical (Z) axis of the deposit might generally be expected, as each layer has a different thermal history [194]. This is not

evident in the microhardness measurements (Figure 5.10a) of the layer bands and top region of the fabricated wall components in the current work. The variation of microhardness in these regions probably results from different microstructure characterisation. From the above discussion, critical factors could be the lamellae thickness and interfaces, especially the lamellar spacing. Generally, high cooling rates can result in a decrease of lamellar spacing, which significantly affects translamellar microcracking and the size of shear ligaments. A small lamellae spacing hinders translamellar microcracking, and linkage of the main crack with interlamellar microcracks thus becomes difficult, leading to larger ligament sizes and higher shear ligament toughening [195]. Nevertheless, it is interesting to note that in the case of the GTAW-based ALM process, despite different lamellae spacing in the top region and the layer bands, the hardness is not significantly affected. Lamellar spacing does not appear to be responsible for the different mechanical performance of these materials. Most probably, the distribution and volume fraction of α_2 and γ phases determine the strength for different areas of the fabricated wall.

5.5 Conclusions

In this chapter, the γ-TiAl deposits fabricated by the GTAW-based ALM process can be divided into three distinct regions along the vertical build direction for the purposes of material characterisation. The microstructure evolution and mechanical properties variation were evaluated as a function of location. Several valuable findings can be summarised as follows:

1. In the near-substrate zone which extends approximately 2mm above the substrate surface, equiaxed α_2 grains with sizes ranging from 50 μm to 150 μm are significantly populated by γ lamellae, which precipitate from the grain boundaries.

2. In the top region that comprises the final 2mm of the additive deposit, the microstructure contains long dendrites interspersed with interdendritic γ phases having a lamellar structure.

3. Between these two relatively narrow bounding regions, the typical morphology exhibits columnar grains that grow epitaxially across a series of layer bands in the build direction. The deposited material is mostly comprised of these layer bands. Fully lamellar colonies consisting of α_2 and γ lamellae are present in the band region, whereas each layer exhibits much coarser interdendritic γ phases surrounded by lamellar microstructure compared with top region.

4. Within the band region, the tensile properties differ by approximately 11 % in the build and travel directions as a result of the anisotropic microstructure in these orientations, although there is no appreciable difference in average microhardness measurements along the two directions.

5. When looking more widely throughout the entire height of the deposited wall component, there are also variations in microhardness, ultimate tensile strength (UTS) and yield strength (YS) that can be ascribed to Al content and the multiple annealing characteristics of GTAW-based ALM process. In the near-substrate zone, considerable increases in microhardness, UTS and YS are a result of the relatively lower Al concentration and higher volume fractions of α_2 phase caused by significantly higher cooling rates in comparison to those experienced by the middle and upper layers. The very fine γ lamellae may be another contributing factor. In the layer bands and top region, a higher Al concentration, a more homogenous Al distribution and comparatively low cooling rates result in lower values of microhardness, UTS and YS. The distribution and volume fraction of α_2 and γ phases are the most likely influences for the measured differences in microhardness and strength between layers and band regions.

6 Effect of Post Production Heat Treatment on γ-TiAl Alloys Produced by the GTAW-based ALM Process

6.1 Introduction

As discussed in Chapters 4 and 5, the GTAW-based ALM process offers several advantages compared to other production techniques for γ-TiAl alloys, including high material use efficiency, high performance full density deposition, and the capability to economically produce large components. However, the unique conditions during the GTAW-based ALM process generate some problems. Firstly, steep temperature gradients are caused by the highly localised heat input and short reaction time of the elemental materials. The thermal expansion coefficient of γ-TiAl is approximately $9.8\times10^{-6}\,K^{-1}$. Therefore, large thermal stresses exist in the as-fabricated build-up. As the formability of intermetallics is poor, the induced residual stresses are responsible for the high probability of cracking or distortion, leading to non-conformance rejection or reduced service life [196]. Secondly, there are segregation phenomena and a large amount of non-equilibrium phases in the as-fabricated materials because of the rapid solidification and subsequent rapid cooling during the process. As a consequence, it is necessary to relieve the residual stresses, and modify the microstructure within the as-fabricated γ-TiAl alloys in order to obtain the required mechanical properties. Generally, heat treatment is one of the common techniques employed for residual stresses relief and modification of microstructure and properties [197, 198]. However, in some cases heat treatment can yield some detrimental effects on the material properties, including increase of residual stresses, degradation of microstructures, and decrease in fracture toughness [199].

Based on the literature review, heat treatments of γ-TiAl alloys have been investigated extensively. Significant efforts have been made to study the nature of the decomposition

of the high temperature α phase, the decomposition of α_2 and γ phases, and the discontinuous coarsening of the α_2+γ and α+γ structures in order to create continuous cooling transformation (CCT) diagrams [183, 200, 201]. The phase transformation and structural morphologies evolution during heat treatment have been given much attention [175, 202-204]. Also, attempts have been made to refine grain size of γ-TiAl alloys through designed heat treatment [205, 206]. However, the parent materials normally used are obtained from ingots that have experienced homogenisation heat treatment and hot isostatic pressing or have been subjected to some degree of previous deformation (i.e. extrusion).

Additionally, in order to control the intrinsic brittleness of the material, post weld heat treatment has been performed in some research work to modify the microstructure and hence improve the mechanical properties. Arenas and Acoff [163] have found that post weld heat treatment at 1000°C and 1200°C on GTA welded γ-TiAl alloy can effectively reduce the brittle α_2 phase in the weld zone. The effect of post weld heat treatment on microstructure and microtexture transformation has been also investigated by Liu et al. [207, 208], and the mechanical properties have been improved as well after heat treatment.

In the present chapter, emphasis has been placed on the response of additive layer manufactured γ-TiAl to post production heat treatment. The residual stresses in both as-fabricated materials and heat-treated materials are measured to validate the effectiveness of stress relief heat treatment at relatively low temperature. The effect of variables involved in the post production heat treatment, such as duration and temperature, on the phase transformation and microstructure evolution are investigated. The relationship between the post production heat-treated microstructures and mechanical properties is also examined.

6.2 Experimental Procedure

6.2.1 Investigated Materials

The inspected γ-TiAl alloys were sectioned from the same wall components that were fabricated in Chapter 5. The starting materials in this chapter were also fabricated using the GTAW-based ALM process with the same process parameters in order to achieve identical components. Three sets of samples were sectioned from the as-fabricated components:

(1) Three bulk samples, referred to as Set 1, were cut from three walls (as-fabricated dimensions approximately 25 mm height, 120 mm length and 10 mm width) following the same cutting sequence. The dimension of the three samples is shown in Figure 6.1.

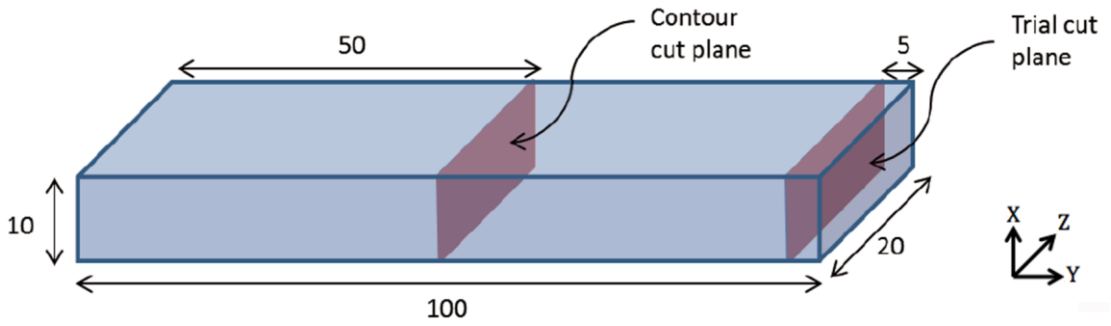

Figure 6.1 Schematic illustration of the location for the trial and main contour cut transverse planes, units are in mm.

(2) Four small samples, referred to as Set 2, were also sectioned from the middle of the wall with as-fabricated dimensions of 19 mm height, 100 mm length and 10 mm width. Figure 6.2 indicates the extraction locations of the samples and their size.

(3) Four bulk samples with two directions, referred to as Set 3, were cut from one large wall with as-fabricated dimensions of 45 mm height, 120 mm length and

10 mm width. The direction, location and size of the samples are shown in Figure 6.3.

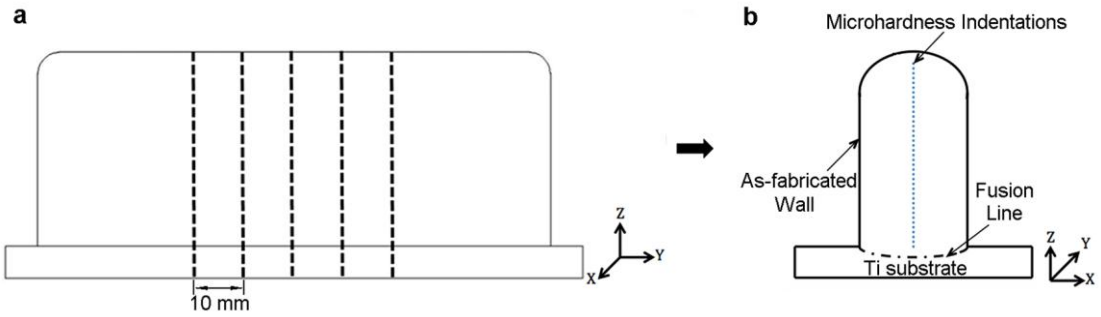

Figure 6.2 The extraction locations of the samples and their size in Set 2, units are in mm.

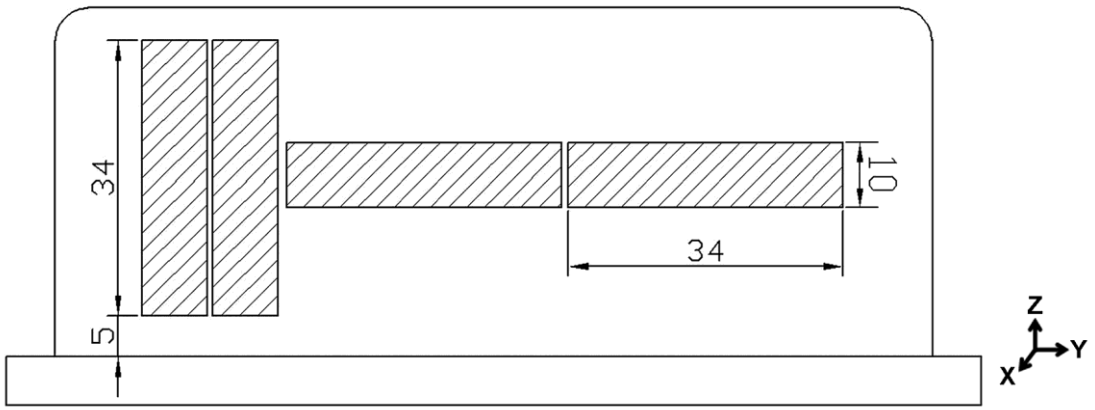

Figure 6.3 The extraction directions, locations of the samples and their size in Set 3, units are in mm.

6.2.2 Post Production Heat Treatment

Two types of heat treatment were performed to investigate the change of residual stress and the evolution of microstructure and mechanical properties, respectively.

(1) Low temperature stress relief heat treatment were conducted on two samples of Set 1 involving uniformly heating up to 400 °C and 500 °C respectively, holding for a period of 2 hours (h) and cooling back to room temperature.

(2) Set 2 samples were heat-treated at two temperatures 1060 °C and 1200 °C for two different times 12 h and 24 h followed by furnace cooling to room temperature. These temperatures were chosen so that the as-built microstructures could be transformed above and below the eutectoid temperature (Te).

(3) Set 3 samples were divided into two groups. Each group has two samples with both Z and Y directions. Post production heat treatments were also performed on the two groups of samples at 1060 °C and 1200 °C separately. All the samples experienced 24 h heating duration with furnace cooling.

6.2.3 Contour Method

The contour method developed by Prime in 2001 [209] was used to measure the longitudinal stresses in Set 1 samples for investigating the influence of stress relief heating at relative low temperature. Based upon solid mechanics, the residual stress is determined by the contour method by cutting a specimen into two pieces in the plane where stress is to be determined, and measuring the resulting deformation due to residual stress redistribution. A finite element model of the specimen is established to account for the stiffness of the material and part geometry, providing a unique result. The residual stresses are then calculated using the measured displacement data. As a result, a 2D map of residual stress normal to the measurement plane can be obtained as the output. This method allows the visualisation of residual stress within the whole section of the assembly.

In this chapter, several steps were taken to achieve high quality contour cuts. Firstly, cutting trials were conducted on one of the heat-treated samples to optimise the wire electrical discharge machine (EDM) cutting parameters. Then, sacrificial materials were bonded to the blocks in the vicinity of the proposed cut plane (mid-length) to prevent cutting artefacts close to the edges of the component. The main contour cut was then

conducted on a plane at the mid-length of the blocks using a Fanuc (α-C600iA) wire EDM with a 150 μm diameter brass wire.

The deformation contours of the created cut surfaces were measured using a Zeiss Eclipse coordinate measuring machine (CMM), fitted with a Micro-Epsilon laser probe and a 4 mm diameter ruby-tipped Renishaw touch trigger probe. The measurement point grid spacing was set to 0.1 mm. The measured deformations were then processed and applied as surface boundary conditions to an elastic finite element model of the cut component.

6.2.4 Metallography

The Set 2 samples were sectioned into metallographic specimens according to standard metallographic procedures. Optical micrographs were taken of the polished and etched cross-sections using the Kroll's reagent. A GBC MMA X-ray diffractometer (XRD) with Cu Kα radiation (λ = 1.5418 Å) was used to measure the phase diffraction profiles for all of the heat-treated samples.

6.2.5 Neutron Diffraction

Ordering phenomena are expected to strongly affect the mechanical behaviour of γ-TiAl alloys due to the change of existing phases upon ordering. However, it is only possible to observe the ordering reaction at its occurring temperature, because the disordered phase is not preserved at room temperature. The fast kinetics of the ordering reactions presents a challenge for investigating the intrinsic properties of titanium aluminide intermetallics. Neutron diffraction is particularly well suited for investigating the ordering behaviour of titanium aluminide alloys, since the diffraction patterns can be acquired at any temperature, as long as the temperature remains constant during the measurement process [210]. It is well known that the scattering lengths of Ti (-3.770 fm) and Al (3.449 fm) are very similar but of opposite sign for neutrons. As a result, a structure factor of close to zero and small intensities are obtained for the main

reflections, while the structure factors for superstructure reflections are large and the observed intensities are therefore rather high.

To study the ordering behaviour of α_2 phase, the WOMBAT instrument at the OPAL reactor of ANSTO was used to conduct neutron diffraction experiments in this work. This instrument is a two-axis powder diffractometer, using a Ge 115 monochromator at 100 ° takeoff angle to acquire neutrons. The facility hosts a true, cylindrical 2D position sensitive detector of 968 × 128 pixels^2 covering 120 ° in the scattering plane and approximately 15 ° out of plane. The neutron wavelength used was λ = 1.67 Å. Depending on the counting statistics, the diffraction pattern can be obtained within a counting time of 18.2 seconds per frame. This frame rate is sufficiently high for determining the order-to-disorder transition temperatures with adequate accuracy.

6.2.6 Microhardness Testing

Vickers microhardness profiles were measured on cross-sections of the Set 2 samples at a load of 200 g (HV0.2). In order to investigate the homogeneity of heat treatment on the as-fabricated materials, indentations were conducted along the centreline from the fusion line to the top of the walls at 1mm intervals. A comparison of the results between the as-fabricated samples and heat-treated samples is presented later in this chapter.

6.2.7 Tensile Testing and Fracture Surface Analysis

Three tensile test specimens with dimensions specified in Figure 3.11 were cut from each bulk sample in Set 3, and hence, there were three specimens tested for each direction of each heat treatment (1200 °C / 24 h and 1060 °C / 24 h), respectively. The room temperature tensile tests were carried out on a MTS370 load unit using uniaxial load with a strain rate of 0.05 s^{-1}. The fracture surfaces of the broken samples were inspected using SEM.

6.3 Results

6.3.1 Residual Stress

Figure 6.4 shows the distribution of longitudinal stresses at mid-length of the as-fabricated sample as well as the low-temperature heat-treated samples, determined by using the contour method. The relative residual stress line profiles across the height are presented in Figure 6.5. It can be seen that the longitudinal stress at mid-length of the wall changes from compressive in the centre to strongly tensile at the top and the bottom of the wall. The highest compressive stress occurs in the middle height of the as-fabricated wall, and there are balancing zones of tensile stress around this area.

These graphs show the effectiveness of low temperature stress relieving heat treatment on the upper section of the walls. The effectiveness is increased when the heating temperature is raised from 400 to 500 °C. However, it appears that heat treatments at 400 °C / 2h and 500 °C / 2h are not particularly effective in reducing the longitudinal stresses in the central and lower section of the walls. For the 400 °C / 2h heat treatment, there is only a small redistribution of stress in the central section, but a more substantial reduction of tensile stress at the lower extremity (Z = 19~20mm). For the 500 °C / 2h heat treatment, there is a more significant redistribution of stresses in the central section, although the peak value of compressive stress is still not significantly changed but instead shifted closer to the bottom of the wall. However, unlike the 400 C treatment, the tensile stress at the lower extremity of the wall has not been relieved by the 500 °C treatment. These somewhat unusual results are discussed further in section 6.4.1.

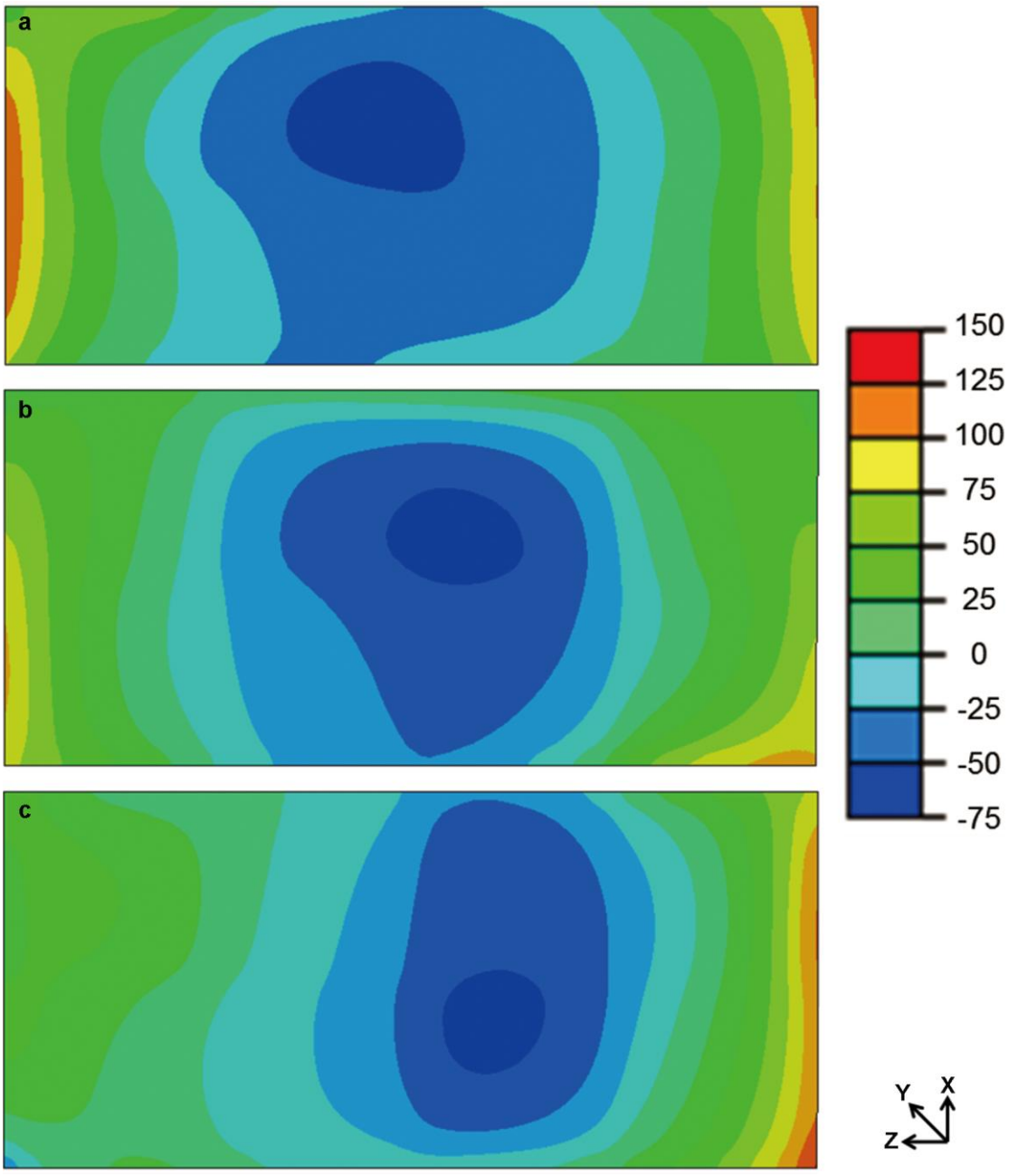

Figure 6.4 Longitudinal stresses distribution measured using the Contour Method in different samples, units are in MPa: (a) GTAW-based ALM produced sample, (b) GTAW-based ALM produced sample after low temperature stress relief heat treatment for 400 °C / 2h, and (c) GTAW-based ALM produced sample after low temperature stress relief heat treatment for 500 °C / 2h.

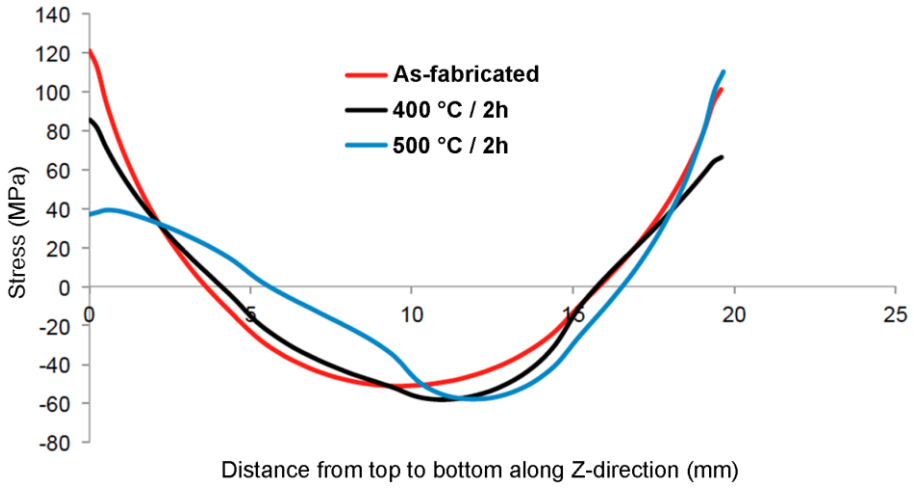

Figure 6.5 Comparison of longitudinal stress line profiles before and after different heat treatment.

6.3.2 Microstructure

Optical micrographs of the GTAW-based ALM built material after high temperature heat treatment at different conditions are shown in Figures 6.6~6.7. The response to heat treatment is a more homogenous microstructure in the majority (middle and upper) region of the heat-treated wall in comparison to the as-built wall. The near-substrate zone exhibits a totally different microstructure because of the significantly different composition when compared to the composition of the majority region, as described in Chapter 5.

The microstructure in the majority region of the heat-treated wall after 12 h at 1200 °C exhibits a near γ microstructure with an average grain size of around 50 μm (Figure 6.6a). The γ grains show different contrast due to different grain orientations. The dendritic structure is no longer present, indicating that a full microstructural transformation has occurred. Relative small lamellar grains are also visible. Instead, the microstructure in near-substrate zone is composed mainly of fully lamellar grains (Figure 6.6b). As expected, when the duration of heat treatment is increased to 24 h, a much coarser microstructure is evident in the majority region, as seen in Figure 6.6c.

The lamellar colony size and lamellae width are also found to be much coarser in the near-substrate zone, as shown in Figure 6.6d.

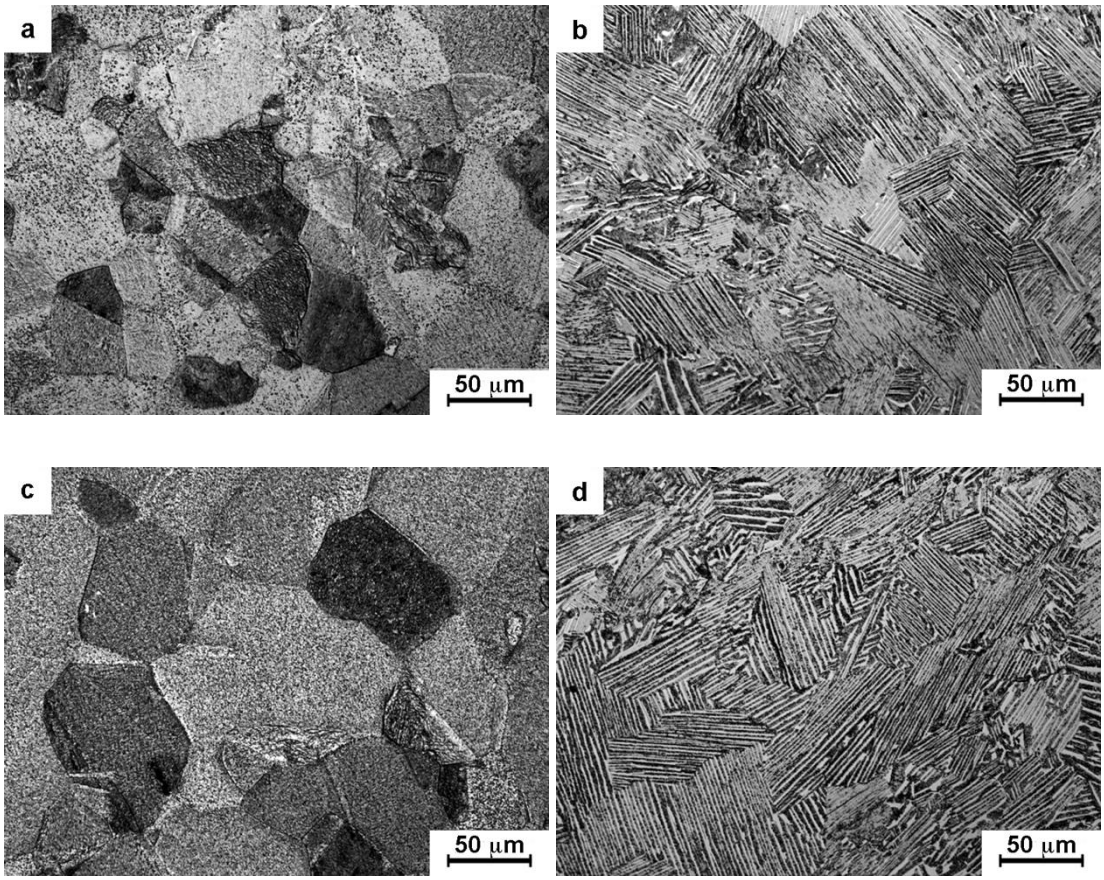

Figure 6.6 Representative microstructure of different regions in cross-section (X-Z plane) of GTAW-based ALM produced γ-TiAl alloys after heat treatment at 1200 °C for different holding times: (a) the majority region and (b) the near-substrate zone after 12 h heating, (c) the majority region and (d) the near-substrate zone after 24 h heating.

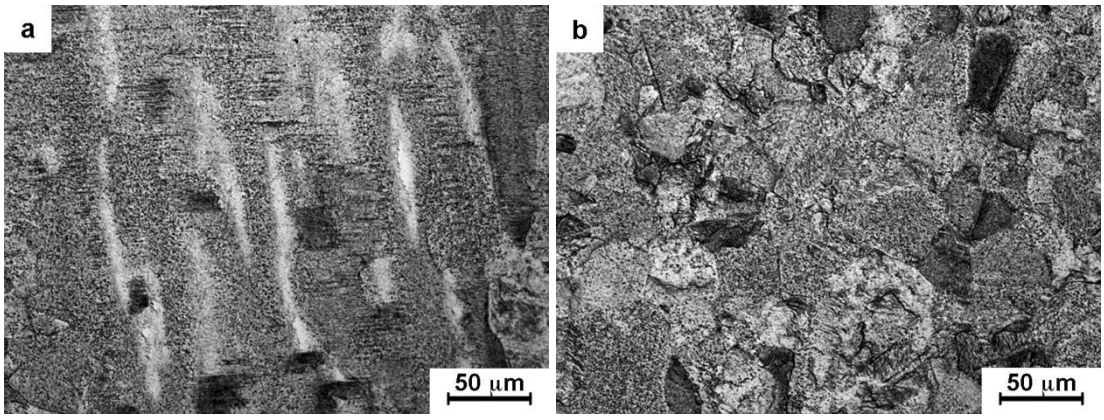

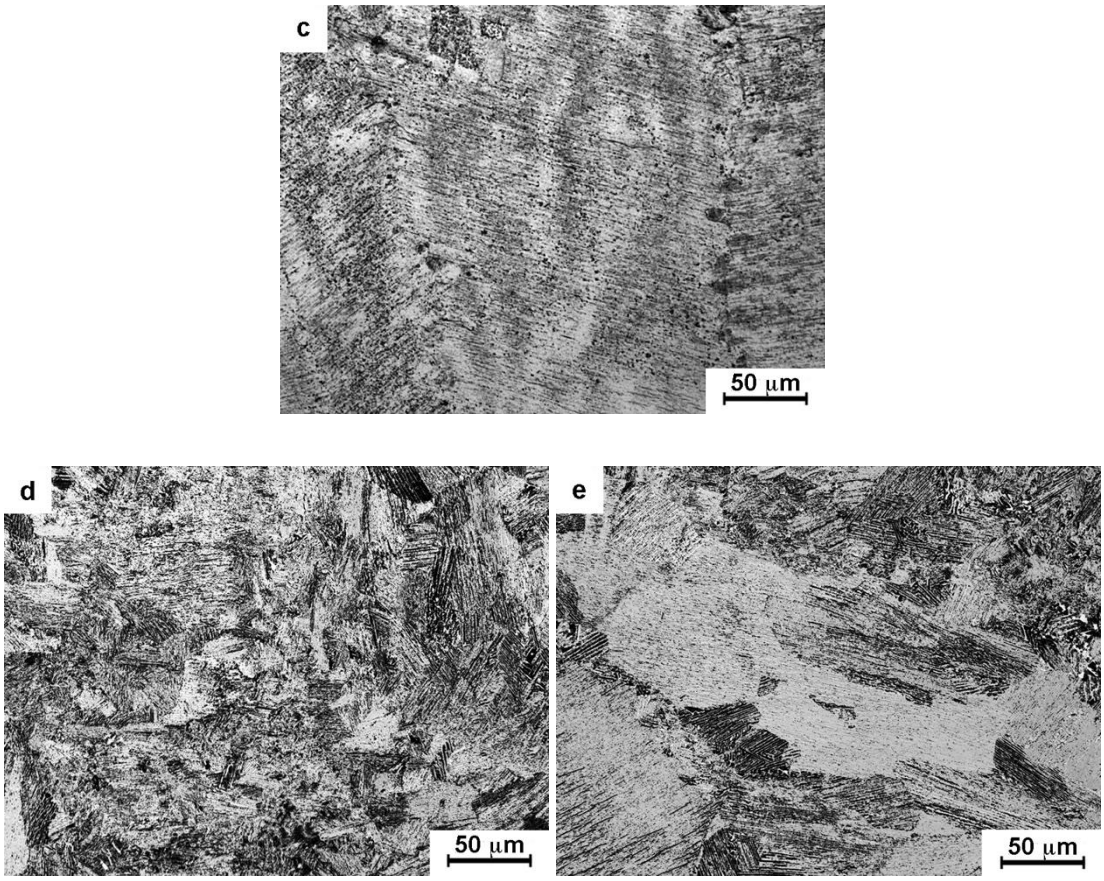

Figure 6.7 Representative microstructure of different regions in cross-section (X-Z plane) of GTAW-based ALM produced γ-TiAl alloys after heat treatment at 1060 °C for different holding times: (a) and (b) the majority region and (c) the near-substrate zone after 12 h heating, (d) the majority region and (e) the near-substrate zone after 24 h heating.

When heat treatment is performed at 1060 °C, which is below the eutectoid temperature Te, there is a significant difference in grain morphology in comparison with the samples treated at 1200 °C, which is above Te. The columnar dendritic structure is partially transformed into a lamellar structure in the majority region after 12 h. It can be seen in Figure 6.7a that the interdendritic structure is still visible. Small and banded lamellar grains are present in the majority region (Figure 6.7b). However, fine γ laths within the coarse α_2 matrix are obtained in the near-substrate zone (Figure 6.7c). After 24 h, the majority region of the GTAW-based ALM built wall exhibits a fully lamellar structure with an average colony size of around 20 μm shown in Figure 6.7d. In the near-substrate zone, the microstructure in Figure 6.7e consists of large equiaxed α_2 grains containing

fine, irregularly spaced γ plates. Nevertheless, the colony size distribution is quite inhomogeneous. The coarsening of some lamellar structure is evident.

6.3.3 Phase Constitution

The majority regions of post production heat-treated alloys obtained in this work were analysed using XRD in order to identify the phases present in those regions. It is of special importance to observe any variation in the intensity of both γ and α_2 peaks in the XRD spectrum, which can reveal changes in volume fraction of each microstructural constituent in the GTAW-based ALM fabricated materials. Figure 6.8 presents the XRD analysis results for the heat-treated samples and as-fabricated ones. The results show that the γ peak intensity of the strongest peak (111) is increased by the 12 h heat treatment at 1200 °C, but remains constant when the duration is increased to 24 h. Conversely, the peak intensity of the α_2 phase consecutively reduces as the duration increases. This is indicative of a reduction in α_2 structure as a result of post production heat treatment. In particular, no observable α_2 phase peak is detected by XRD when the holding time is increased to 24 h, which indicates that the percentage of α_2 phase decreases below the detection limit.

For the heat treatment performed at 1060 °C, the α_2 peak intensity is slightly reduced after 12 h heating, while there is no obvious change for the peak intensity of γ phase. However, increasing the duration from 12 h to 24 h results in a completely different development of both γ and α_2 phases. Firstly, the considerable reduction of γ peak (111) intensity is ascribed to the dissolution of interdendritic γ phase. Furthermore, the much stronger α_2 peak (201) suggests a significantly increase in α_2 phase volume fraction due to the formation of fully lamellar colonies consisting of α_2 and γ lamellae. All the above results agree with the microstructural analysis.

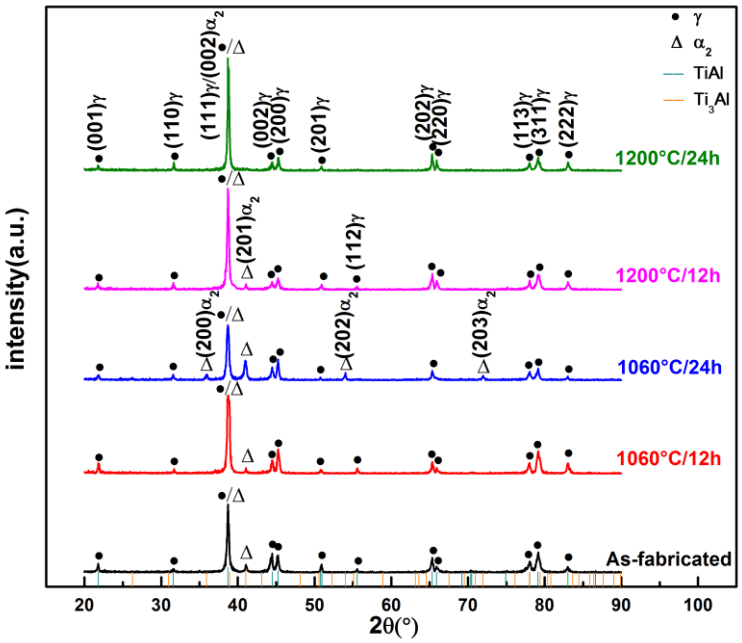

Figure 6.8 Comparison of phase constitutions in cross-section (X-Z plane) of GTAW-based ALM as-fabricated γ-TiAl alloys and heat-treated alloys at different conditions.

6.3.4 In-situ Neutron Diffraction

Figure 6.9 shows the reflection patterns of both γ and α_2 phases acquired from an as-fabricated sample that has been placed in the neutron beam line and progressively scanned at temperatures of 1000 °C, 1060 °C and 1200 °C. The results are indicative of the phase constitutions and their corresponding fraction at these three temperatures. The phase transformations undergone within a single as-fabricated alloy sample can therefore be studied. It is clear that only the superstructure reflection of γ phase is visible at 1200 °C. The α_2 reflection starts to diminish from 1000 °C to 1060 °C, and is completely absent by 1200 °C. Only 1% volume fraction of α_2 phase remains at 1060 °C. The vanishing of the superstructure reflections indicates the loss of order α_2 phase due to the average scattering length of the disordered material being close to zero [210].

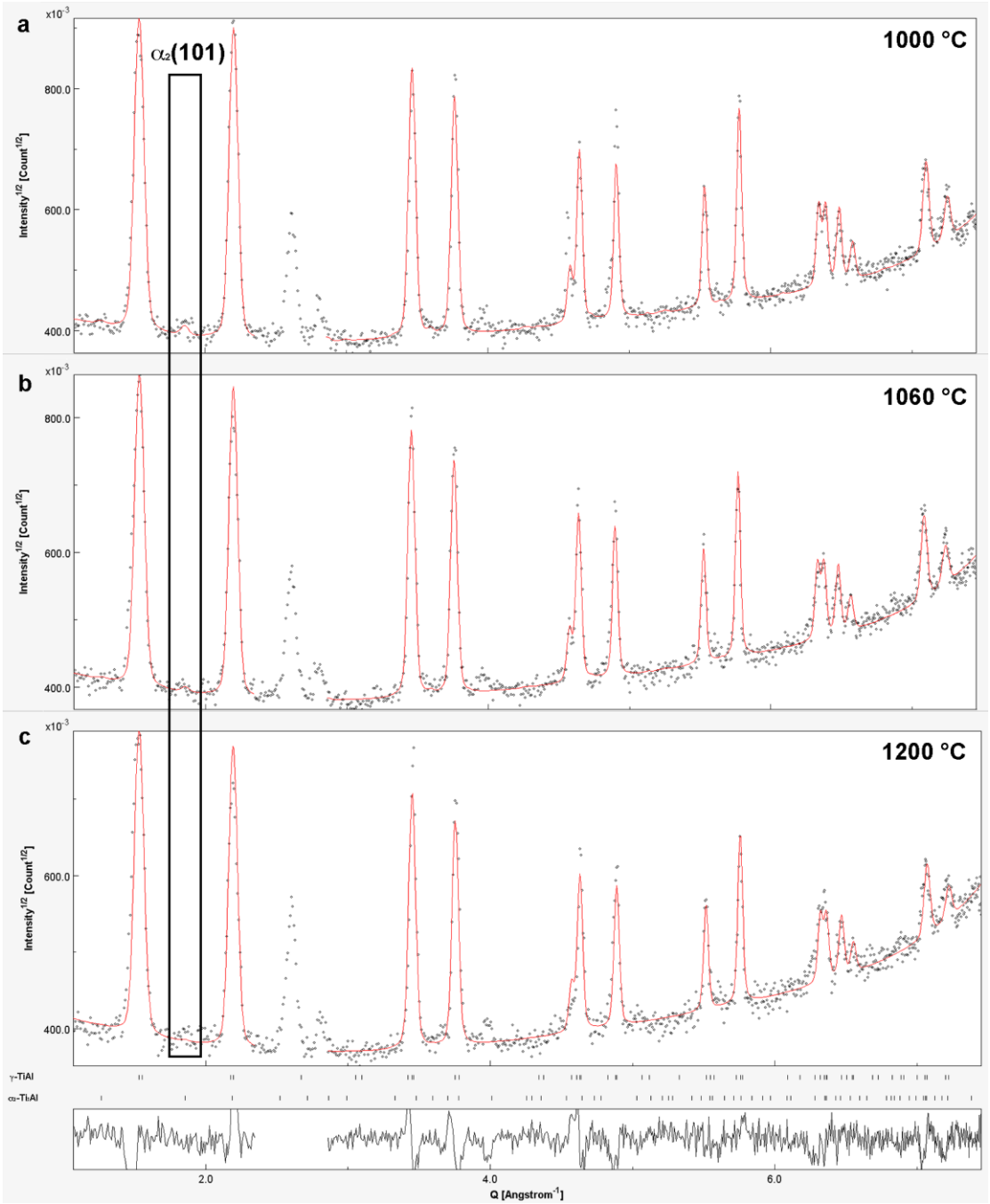

Figure 6.9 Neutron diffraction patterns at different temperatures for GTAW-based ALM produced γ-TiAl alloys: (a) 1000 °C, (b) 1060 °C, and (c) 1200 °C.

6.3.5 Microhardness Measurements

The microhardness profiles for alloy samples that have been heat treated at different temperatures for different holding times are plotted as a function of distance from the fusion line in Figure 6.10. The results are superimposed onto the profile for the as-

fabricated condition. For all samples, there is a large deviation in microhardness values between the near-substrate zone and the majority region. This is expected due to the Al concentration difference between the near-substrate zone and the majority region for every sample, as previously discussed in Chapter 5.

The heat-treated samples at 1200 °C exhibit a considerable reduction in microhardness for both the majority region and the near-substrate zone compared to the as-fabricated condition. The decrease of microhardness in the majority region occurs in a more dramatic manner than that in the near-substrate zone. As the duration is increased from 12 h to 24 h, microhardness values further decrease and reach a minimum mean value 206 HV0.2 in the majority region.

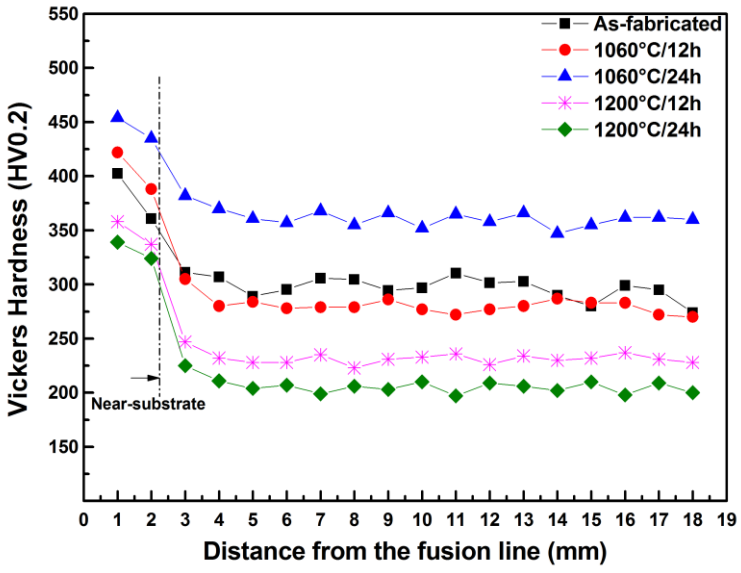

Figure 6.10 Microhardness profiles as a function of location in cross-section (X-Z plane) of GTAW-based ALM as-fabricated γ-TiAl alloys and heat-treated alloys at different conditions.

However, heat treatment at 1060 °C results in totally different microhardness results. A slight decrease in microhardness is obtained in the majority region of 1060 °C / 12 h heat-treated specimens, while microhardness values in the near-substrate zone are slightly higher than those in the as-fabricated specimens. In addition, a comparison of the hardness profile of the 1060 °C / 24 h heat treatment to the other specimens shows

that an overall higher microhardness is obtained for the 1060 °C / 24 h heat treatment. Furthermore, it is interesting that increasing the duration to 24 h at 1060 °C leads to a significant increase in microhardness, instead of further decreasing the microhardness in the majority region as occurs at 1200 °C. Simultaneously, the near-substrate zone in the 1060 °C / 24 h specimen exhibits a much higher microhardness relative to the 1060 °C / 12 h specimen, following the same general trend exhibited by the majority region.

6.3.6 Tensile Properties

The room-temperature tensile properties of both the as-fabricated and heat-treated materials are shown in Figure 6.11. The tensile samples were obtained from the majority region with homogeneous microstructure, as this is the region of major interest. As can be seen, post production heat treatment can effectively eliminate the strength deviation between the travel direction (Y) and build direction (Z), whereas the tensile elongations do not seem to significantly differ for the different directions irrespective of whether heat treatment has been performed. The difference between ultimate tensile strength (UTS) values for the Y-direction and Z-direction, which is more than 60 MPa for the as-fabricated materials, is reduced to approximately 20 MPa and 10 MPa after heat treatment at 1060 °C / 24 h and 1200 °C / 24 h, respectively.

Furthermore, the tensile properties differ greatly between the various heat treatments. The 1200 °C / 24 h heat-treated samples are markedly softer than the as-fabricated samples. The UTS and yield strength (YS) values along the Y-direction decrease to 471 ± 14 MPa and 421 ± 11 MPa respectively after the 1200 °C / 24 h heat treatment, while the YS does not change appreciably in the Z-direction. The tensile elongation increases to 1.1 % after the 1200 °C / 24 h heat treatment.

Heat treatment at 1060 °C / 24 h leads to an increased UTS of 590 ± 4 MPa along the Y-direction and 569 ± 12 MPa along the Z-direction, which are 7 % and 17 % higher than the as-fabricated samples along the corresponding directions. There is no significant

change in the YS along the Y-direction, while the YS along the Z-direction by more than 50 MPa higher YS so that comparable YS values are produced along both directions. A tensile elongation of approximately 0.4 % is obtained for the 1060 °C / 24 h heat treatment, slightly lower than the 0.5% value for the as-fabricated material.

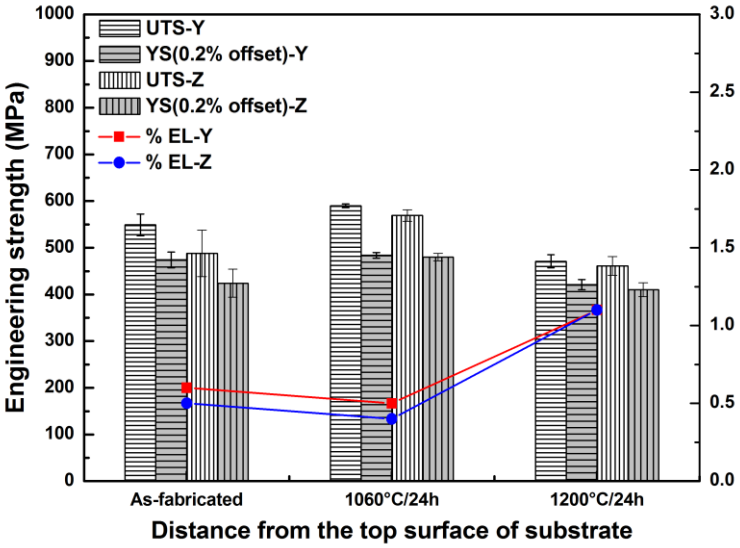

Figure 6.11 Comparison of the room-temperature mechanical properties of GTAW-based ALM as-fabricated γ-TiAl alloys and heat-treated alloys at different 24h heat treatment temperatures, tested along both the build direction (Z) and the travel direction (Y) for each condition.

The fracture surfaces of heat-treated samples are shown in Figure 6.12. The fracture morphologies after tensile testing are quite similar for the two microstructures with differing heat treatment temperatures. The predominantly transgranular cleavage fracture is present over the entire fracture surface. The fracture modes are brittle fracture, and no dimples could be observed in all cases.

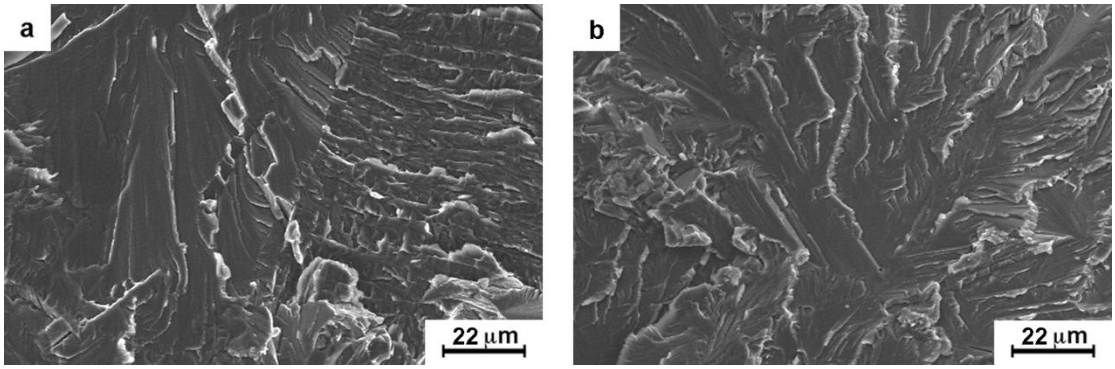

Figure 6.12 SEM fractographs GTAW-based ALM produced γ-TiAl alloys after heat treatment at different temperature for 24 h: (a) 1200 °C, and (b) 1060 °C.

6.4 Discussion

6.4.1 Residual Stress

According to the geometry of the manufacturing process, the longitudinal direction is expected to exhibit the largest residual stresses because of the longitudinal expansion and contraction during deposition [211]. Typically, the maximum stress is close to the weld zone and decreases with the distance from the deposit [212]. As discussed in Chapter 5, the last layer is deposited on the previous layers without further heat treatment. Due to the different thermal expansion coefficients of Ti and Al, the as-fabricated materials are usually stressed residually by curing contraction [213]. The occurrence of shrinkage hindrance by the deposited materials below the last layer, as well as the subsequent non-uniform cooling could result in the highest stress below the last layer. On the other hand, every layer in the middle region has been partly melted during the deposition of its subsequent layer. The volumetric expansion during remelting is translated into a compressive state of stress due to the constraint of the underlying material. However, the melting time of this area is very short. The excessive amount of heat input in each layer promotes the dislocation movement and relieves the internal stress. In addition, the materials near the substrate have considerably lower Al

content (~ 40 at.%), and the cooling rate is higher compared with the materials that are deposited in other areas. Therefore, high stress remains in this area due to the high volume fraction of α_2 phase with a limited number of dislocations systems. Although this area experiences multi-cycle heat treatment by the subsequent deposition of many layers, the extremely short heating time (approximately 10 s) is not sufficient to reduce the stress level.

It is well know that stress relief heat treatment is used to reduce the stresses that remain locked in a structure as a consequence of manufacturing processes [214, 215]. In this work, low temperature heat treatment from 400 to 500 °C was effective in increasing the activity of dislocations and hence relaxing the residual stresses in the upper section of the as-fabricated components. Conversely, the residual stresses in the central and lower sections of the wall showed abnormal variation by stress relief heat treatment. This interesting phenomenon could be attributed to the mismatch in thermal expansion coefficients of the γ and α_2 phases. The volume contraction of γ phase in the upper and central sections of the wall generates a certain amount of stress on the lower section of the wall where the α_2 phase is the principal phase composition. As such, some of the area just below the centreline (Z = 10 ~16 mm in Figure 6.5) exhibited slightly higher stresses after 400 °C / 2h heat treatment despite the lower stresses obtained in the lower extremity of the wall (Z = 17 ~20mm). When the heating temperature was increased to 500 °C, the volume change was more significant due to the increased thermal expansion coefficients with temperature [216]. Hence, even higher stresses were measured in the lower half of the wall (Z = 12 ~20 mm), while the stresses above the centreline are markedly reduced, particularly at the top extremity of the wall.

6.4.2 Microstructure and Phase Transformation

Microstructure and phase volume fraction of as-built γ-TiAl based alloys were strongly modified by post production heat treatment. The as-built material is composed of coarse lamellar dendrites with fine lamellar spacing. These metastable structures that are

developed during the GTAW-based ALM process contain many kinds of imperfections such as stacking faults, edges and grain boundaries. These imperfections play a key role in initiating instability of the lamellar structure during heat treatment. Since both of the phases that are present in the lamellar structure have thin, long plate morphology, there appear to be no curvature effects, which implies that the chemical potentials of the atoms are the same everywhere except for growth faults and edges. Small perturbations in the shape of an infinite perfect plate are expected to decay, as in the case of a flat surface, so that reducing imperfections by heat treatment would enhance their stability [217].

Heat treatment at 1200 °C in α+γ phase field for the majority region of the GTAW-based ALM fabricated wall results in a complete change of microstructure. The dissolution of the γ lamellae and disordering of α_2 phase occur during heating, while γ lamellae precipitate within the α matrix during the treatment holding time. According to previous studies [218], the γ plates nucleate on stacking faults. After a fully lamellar structure has developed, the γ width then increases continuously at the expense of the nucleation ratio decreasing within the remaining time, so that the only further reaction is coarsening of the existing γ laths. Also, additional titanium diffuses out of the α phase into the surroundings when the duration of heat treatment is increased, which is beneficial to the lamellar phase. This has been seen to occur for TiAl-based alloys prepared using powder metallurgy [219]. Both the γ and α phase tend to coarsen when a longer heat treatment time is used, but hinder each other, hereby limiting grain growth. However, as pointed out by [220] these lamellar colonies that are formed in the vicinity of the α-transus temperature are not actually stabilised and tend to gradually disappear upon furnace cooling, which offers sufficient time for the γ phase to grow as individual γ grains. Meanwhile, the ordering transformation $\alpha \rightarrow \alpha_2$ occurs in the retained lamellar structure as well.

In contrast to the majority region, the near-substrate zone undergoes heat treatment at 1200 °C in the α phase field due to the lower Al content (~40 at.%). Fully lamellar structures form in the α_2 matrix through the phase transformation path $\alpha \rightarrow \alpha_2 \rightarrow \alpha_2+\gamma$ during furnace cooling.

The microstructural analysis for heat treatment at 1060 °C shows a progressive transformation from dendritic to fully lamellar structure as the duration of the heat treatment is increased from 12 h to 24 h. When the GTAW-based ALM fabricated alloys are reheated to 1060 °C, which is slightly above the metastable α_2 / $\alpha_2+\gamma$ phase boundary in the $\alpha_2+\gamma$ phase field, the non-equilibrium interdendritic structure begins to dissolve together with the disordering of α_2. Meanwhile the gamma laths partially transform back to alpha, further refining the grain size. Because the primary lamellae are very stable and the decomposition of the lamellar structure is very slow, the 12 h heating at 1060 °C can only promote an incipient transformation and the microstructure remains non-equilibrium. As a result, the longer holding time of 24 h is required for the disappearance of the interdendritic structure and primary lamellar dendrites. During the subsequent cooling, the $\alpha \rightarrow \alpha_2$ occurs first followed by precipitation of γ laths in α_2 matrix as described in CCT curves [183]. In addition, discontinuous coarsening (DC) also occurs in the majority region of heat-treated alloys at 1060 °C. DC is a reaction during which a two-phase structure with high density of interfaces is transformed into a coarser lamellar structure by grain boundary diffusion along the transformation front [221]. The driving force is provided by the reduction of both the interface energy and the chemical free energy, which corresponds to a change in the matrix composition as well as in the volume fraction of each phase of the lamellar structure before and after the discontinuous coarsening [222]. However, based upon the study of Jung et al. [223], the elastic strain energy appears to act as the driving force for the migration of grain boundaries rather than the interfacial or chemical energy. The reason is that there is no apparent geometrical angular relationship between the primary lamellar interface and the migrating grain boundary plane. Despite this controversial issue, it is accepted that

the DC cells normally nucleate at original colony boundaries and grow into the adjacent lamellar colony by consuming its primary fine α_2/γ lamellae [224]. However, the growth rate of DC structures has been demonstrated to be extremely slow in Ti42Al alloys [225], where the length of DC cells only extended 5 um from 1 h to 100 h. The low coarsening rate is attributed to the low density of ledges at the interphase interface, which contain very few Shockley partial dislocations [226]. Moreover, such a coarsening gradually slows down and becomes progressively difficult because of a decrease in ledge mobility associated with the decrease of solute supersaturation [222]. As a consequence, the overall structure of the majority region can be replaced by relatively coarse α_2/γ lamellae within fine lamellar colonies. In considering the near-substrate zone with 40 at.% Al, DC plays a dominant role in controlling the microstructural variation.

6.4.3 Mechanical Properties

The microstructural characteristics including type of microstructure, phase distribution and grain size have been shown to strongly control the mechanical properties of γ-TiAl alloys, and therefore microstructural modifications produced by post production heat treatment can make significant changes to the mechanical properties.

Firstly, the variation of microhardness and tensile properties is strongly affected by the types of microstructure. In general, the interface of layered microstructure provides locations for crack nucleation sites and yields highly anisotropic and non-uniform deformation [34, 52]. Accordingly, the lamellar grains made of two phases are expected to be the representative multilayer system, and their poor tensile properties at room temperature have been well documented in the literature [227-231]. Equiaxed γ grains have been recognised to be softer than lamellae [29, 38]. Also, the type of microstructure has a direct effect on the change of tensile elongation. This is due to the fact that the nature of dislocations and the ease of slip or twinning in specimens with the same composition are known to have a similar influence on deformation [192]. It is well

known that near-γ grains show the highest ductility compared with other microstructure types for alloys with a given composition, while the fully lamellar structure exhibits the lowest ductility [54].

Additionally, the volume fraction of different phases, especially the α_2 phase fraction, is correlated with the mechanical properties of dual phase titanium aluminides. It has been demonstrated that the dislocations to glide in the α_2-Ti_3Al phase needs significantly larger critical resolved shear stresses compared to the activation of slip in γ-TiAl phase [193]. Therefore, higher strength can be obtained in materials with a larger amount of α_2 phase. However, an excessive amount of brittle α_2 phase can eliminate the beneficial effect of refined microstructure and hence lead to poor ductility. The maximum tensile elongation usually appears in materials with an α_2/γ phase ratio of 3 % to 15 % owing to the pronounced growth of grains above this range [53]. As a result, the amount of α_2 phase should be controlled accordingly, to achieve, an appropriate balance between strength and ductility.

Moreover, the mechanical properties are inversely proportional to the grain size for each type of microstructure on basis of the Hall-Petch relationship [55]. As the grain size decreases, the volume of defects such as grain boundaries increases, which in turn aids in the deformation mechanisms. Consequently, the strength and ductility of coarse grained microstructure are normally lower than those of microstructure with fine grain size.

Based upon the above discussion, the response of the as-fabricated material to the various applied heat treatments is completely different. The equiaxed γ microstructure as a result of heat treatment at 1200 °C / 24 h plays a crucial role in reducing the microhardness and tensile strength but enhancing the tensile ductility. This is not surprising because the deformation of equiaxed γ grains can be facilitated by easy glide of dislocations ($\frac{1}{2}\langle 110]$ slip and $(111)\langle 11\bar{2}]$ twinning) during the localised plastic

deformation that is generated during microhardness and tensile testing [232]. Besides, the extremely low volume fraction of α_2 phase is also responsible for the reduction in microhardness and tensile strength and the increase in ductility. Conversely, heat treatment at 1060 °C / 24 h results in a fully lamellar structure as well as large amount of α_2 phase, which effectively increase the strength but decrease the ductility of the alloy. The grain size should be considered as another key issue to change the mechanical properties. Although the reduction of lamellar colony size contributes to the highest tensile strength of heat-treated samples at 1060 °C / 24 h, it is a less important factor in enhancing the ductility compared to the amount of γ grains when the microstructure is mainly composed of lamellar grains. As such, the resultant microstructure exhibits the lowest tensile ductility after 1060 °C / 24 h heat treatment.

6.5 Conclusions

In this chapter, two types of post production heat treatment were performed on the γ-TiAl alloys fabricated by the GTAW-based ALM process. The influence of temperature and holding time has been assessed. Particular attention has been given to the analysis of residual stress distribution, microstructure evolution (especially the behaviour of ordered α_2 phase) and the resulting mechanical properties. The most important conclusions are summarised as follows:

1. The longitudinal stress in the as-fabricated component changes from tensile in the top of the wall to compressive in the middle of the wall. After low temperature heat treatment at 400 °C and 500 °C for 2 h, the residual stresses are significantly reduced in the upper half of the wall, where the microstructure is dominated by γ phase. The stress relief is much more pronounced for the 500 °C treatment. However, the presence of α_2 phase in the lower section of the wall, due to lower Al content, results in only minor changes in residual stress conditions around this area. These results show that the effectiveness of low

temperature stress relief heat treatment can be difficult to predict for components that have significant variations in Al content throughout their geometries.

2. Post production heat treatment at 1200 °C resulted in equiaxed γ grains in the majority region of the as-fabricated materials. Grain coarsening occurred with an increase of heating duration from 12 h to 24 h. The near-substrate zone exhibited a different fully lamellar structure due to the low Al content in this area.

3. Post production heat treatment at 1060 °C produced a fully lamellar structure with different size in different regions. The dendritic structure in the majority region of the as-fabricated materials was partially transformed after 12 h heating, and then fully transformed into lamellar structure when heated for 24 h through both continuous and discontinuous reaction. However, the microstructure evolution in the near-substrate zone was primarily controlled by discontinuous reaction.

4. Mechanical properties were closely dependent on the microstructural characteristics resulted from different heat treatment temperatures. Post production heat treatment can generate homogenous microstructure in the majority region, and hence effectively reduce the differences in mechanical properties between the build direction (Z) and travel direction (Y). For a 1200 °C / 24 h heat treatment, the UTS and microhardness decrease while the tensile ductility rises, because of the decomposition of α_2 phase accompanied by the formation of equiaxed γ grains. Conversely, for heat treatment at 1060 °C / 24 h the resultant fine fully lamellar structure and a large amount of α_2 phase contribute to an increase of UTS and decreased ductility.

7 Preliminary Study of Functionally Graded Ti-Al Alloys Produced by the GTAW-based ALM Process

7.1 Introduction

Functionally graded materials (FGMs) are defined as heterogeneous materials exhibiting a controlled spatial variation of their chemical compositions and/or microstructures along at least one direction [233]. Recently, FGMs have attracted much attention because of their unique multifunctional behaviour. The development of FGMs is expected to have a strong impact on the design and development of new components and structures with better performance for widespread applications in aerospace, automotive, defence, electronics, biomedical and power engineering sectors [234].

The term “functionally graded materials” was first introduced in Japan in 1984. These materials were initially designed as thermal barrier materials for aerospace structural applications and fusion reactors [235]. In some of these applications, extremely high temperatures are imposed only at certain regions of a component. A gradient of chemical, physical and mechanical properties are required through the component to withstand operation under these conditions and FGMs are often more appropriate than mono-composition alloys in high temperature environments [236]. Typically, FGMs are made from a mixture of ceramic and a metal or a combination of different metals. A number of studies have been conducted on the functionally graded metal matrix composites (FGMMC) that comprise FGMs with metal and ceramic constituents [237] and on conventional metal alloys based FGMs, for instance; stainless steels [238], titanium alloys [239, 240], and nickel-based super alloys [241]. However, limited research covering intermetallic-based FGMs can be found in open literature. It is reported that intermetallic Al-based FGMs have been successfully fabricated by the centrifugal casting method [242-249]. A variety of different production methods have

been employed for the synthesis of FGMs [250] and intermetallic titanium aluminides [75]. The manufacturing processes for FGMs vary from novel material processing routes, such as laser surface cladding, to well established industrial material processes such as case carburisation for steel [250, 251]. The preferred methods are generally based on the solidification route due to their economics and ability to make large components. Recently, a major part of FGM research has been dedicated to additive manufacturing of these materials. Laser deposition has been employed to fabricate graded Ti-Rene88DT superalloy [236], graded Ti-V and Ti-Mo alloys [252]. Niendorf et al. [238] used selective laser melting to produce functionally graded stainless steel and have investigated the resulting microstructure characterisation.

This chapter will investigate the feasibility of using the GTAW-based ALM process to fabricate functionally graded Ti-Al alloys. Although titanium aluminides are widely recognised as promising structural materials, their brittle nature limits their application. These limitations may be overcome by using titanium aluminides as a basis for metal-intermetallic FGMs or functionally graded composites, thereby providing attractive properties for certain engineering applications. This study of functionally graded Ti-Al alloys proposes an innovative approach for the development of high temperature structural materials in aerospace and automotive applications. The core issue is to understand the location dependence of phase evolution and the mechanical performance of the deposited component.

7.2 Experimental Procedure

7.2.1 Investigated Materials

The same ALM system that was used to produce intermetallic titanium aluminides presented in the previous chapters is used to deposit functionally graded Ti-Al alloys. A pure titanium substrate was used as the base for deposition. The GTAW torch was

directed onto the substrate to create a molten pool into which two elemental wires were injected. The wires were melted and subsequently re-solidified to form the consecutive layers. A dual wire feeding system was used to deliver both pure Ti and pure Al wires. The compositional gradation along the height of the deposited material was achieved by controlling the feeding rate ratio of both wires in order to achieve the predesigned graded structure. The first 5 layers were expected to contain 20 at.% Al. The expected composition of the deposit was then changed every 5 layers from 20 at.% Al to 50 at.% Al. The process parameters were selected according to the previous study on γ-TiAl alloys in Chapter 4 using 120 A current and 400 °C interpass temperature. The detailed wire feed rates for both Ti and Al wires are summarised in Table 7.1.

Table 7.1 Wire feed rates to produce Ti-Al FGMs.

	Layers	Wire feed rate for Ti wire, mm/min	Wire feed rate for Al wire, mm/min
Set 1	1 ~ 5	1060	330
Set 2	6 ~ 10	1005	430
Set 3	11 ~ 15	950	510
Set 4	16 ~ 20	900	600
Set 5	21 ~ 25	850	700
Set 6	26 ~ 30	800	810
Set 7	31 ~ 35	750	930

7.2.2 Metallography

The as-fabricated graded material was sectioned along the deposition direction (vertical XZ plane). The samples were polished according to the standard metallography method for γ-TiAl based alloy, and then etched in Kroll's reagent for metallographic characterisation by optical microscopy (OM). A series of micrographs from typical regions were captured.

7.2.3 Composition and Microhardness Testing

The composition along the gradient direction was determined using energy dispersive spectroscopy (EDS) fitted to a scanning electron microscope (SEM).

To mark the locations for the EDS analysis, microhardness measurements were recorded by a Vickers microhardness indenter vertically along the compositional gradient with 0.5 mm indentation intervals and 200 g load.

7.3 Results

7.3.1 Composition Gradient

Figure 7.1 shows the results of EDS analysis along the vertical direction of the graded deposit. The composition along the entire height of 34 mm varies from Ti-8 at.% Al to Ti-50 at.% Al. The elements Ti and Al show a certain degree of linearity along the compositional gradient. It is interesting to note that although the wire feed rates used for the graded alloy were varied in a step-wise manner every 5 layers, the resulting alloy exhibits a continuously changing composition for each deposition set. The exception occurs when using the last three deposition sets (Set 5, Set 6 and Set 7 in Figure 7.1), which tended to produce Ti-40 at.% Al, Ti-45 at.% Al and Ti-50 at.% Al alloys, respectively, in a more step-wise manner in accordance with the change of wire feeding ratio. Clearly, regions with more constant composition can be obtained for higher Al content. This is particularly apparent in the uppermost 3 mm of the deposit having approximately 50 at.% Al. Interestingly, the rate of change in Al content is highest when the wire feeding ratio is altered at the beginning of each set, particularly for Al contents less than 35%. This trend tends to disappear for higher Al content, where the Al content ramps up smoothly in the first 2 layers and then rapidly reaches an equilibrium value that is dictated by the wire feeding ratio. Furthermore, deposition sets 6 and 7 produce a

relatively small abrupt increase in the composition range produced by the deposition from previous sets.

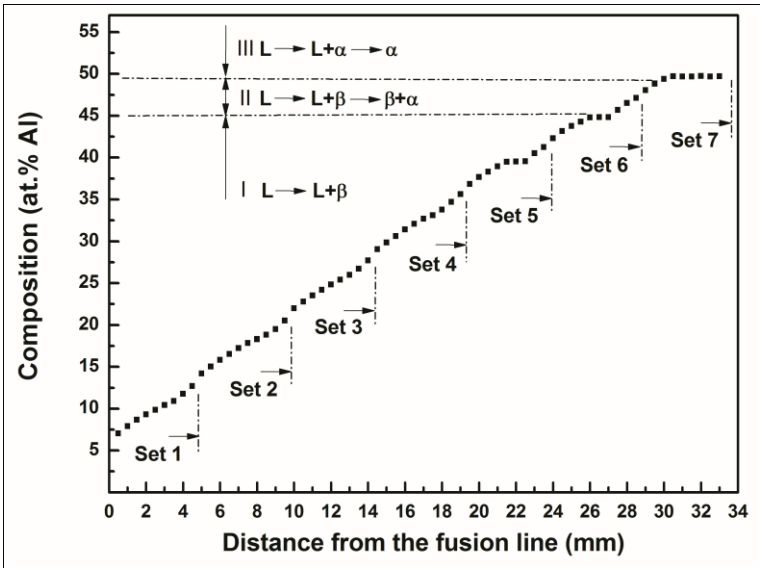

Figure 7.1 The compositional gradient in the Ti-Al FGMs fabricated by GTAW-based ALM process.

7.3.2 Microstructure Evolution

A series of optical micrograph from regions of successively increasing Al content are shown in Figure 7.2. All the images have been recorded at the same magnification across the compositional gradient.

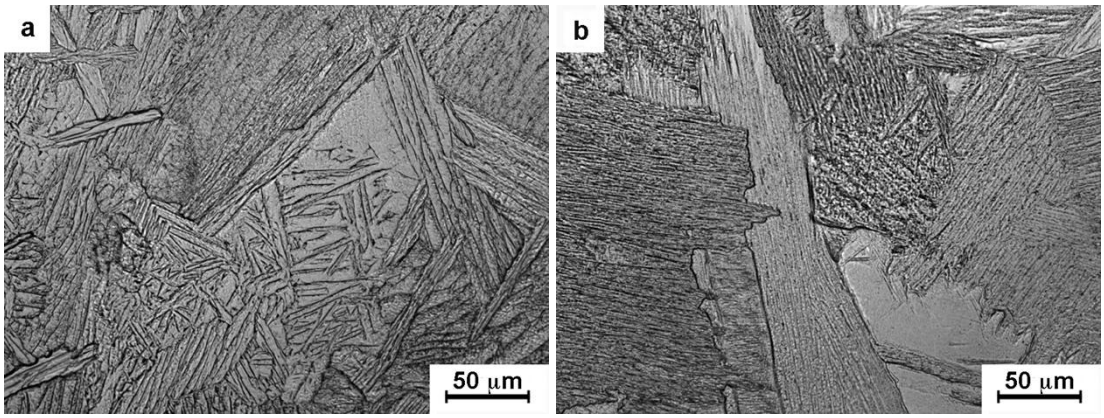

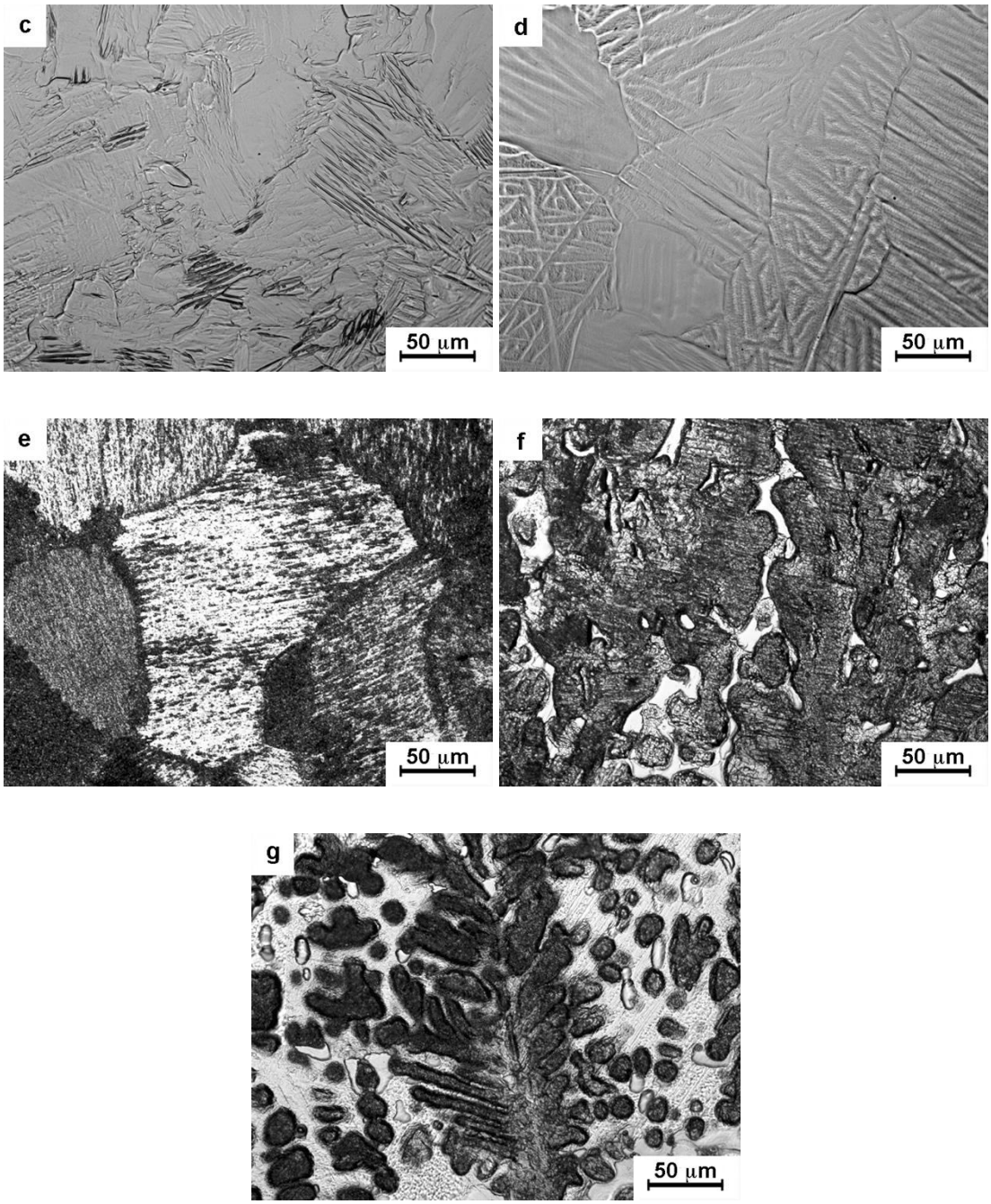

Figure 7.2 (a ~ g) A series of OM images from regions with progressively higher Al content in GTAW-based ALM produced Ti-Al FGMs.

Set 1 has produced conventional type Ti alloys, and their representative microstructure in Figure 7.2a exhibits a typical Widmanstätten lath-like morphology with more laths appearing to originate from the grain boundary α layer. Also, the α laths appear to be of the same size scale.

In Figure 7.2b, corresponding to an average local composition of Ti-15 at.% Al, the microstructure consists primarily of fine lamellae and some needle-like phase in the α matrix.

The Ti-25 at.% Al alloy in Figure 7.2c exhibits crooked grain boundaries as well as fine plates within grain interiors. A similar characteristic microstructure is found in Ti-35 at.% Al alloys (Figure 7.2d), showing a network of ragged grain boundaries with several acicular plates inside the grains. This feature has also been observed in a button-shaped ingot [253]. Figure 7.2e represents the microstructure in Ti-40 at.% Al alloys. The γ lamellae grow along one direction in a grain and develop fairly periodically in the α_2 matrix.

A typical representative lamellar structure in dendrites and white interdendritic γ regions for Ti-45 at.% Al alloy is shown in Figure 7.2f. The study in previous chapters on additive manufactured γ-TiAl alloys has presented similar microstructure. Increasing the Al composition leads to a Ti-50 at.% Al alloy at the uppermost region of the functionally graded deposit. The dendrites with branches pointing at ~60 ° angles can be seen in Figure 7.2g. Similar hexagonal dendrites have been observed by Duarte et al. [178] in the as-cast titanium aluminides with the same composition.

7.3.3 Microhardness Measurements

Figure 7.3 shows the microhardness variation throughout the as-fabricated Ti-Al FGMs as a function of the local Al composition. Initially, there is a considerable increase in microhardness with increasing the Al composition up to around 17 at.%. Thereafter, adding more Al leads to a relatively slow increase in microhardness following a predominantly non-linear function. The microhardness then goes up sharply to a peak value of 516 HV0.2, which corresponds to a 27~28 at.% Al content. After that, there is only a small change in the microhardness value until the Al content reaches 35 at.%. A

sharp decrease in microhardness is then observed with increasing Al content, decreasing significantly until the maximum Al content of 50 at.% is reached.

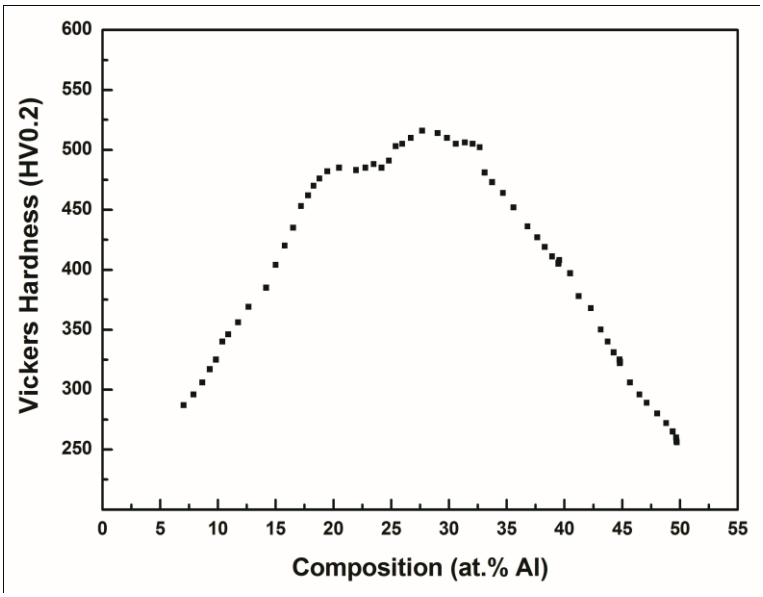

Figure 7.3 The microhardness value measured along the compositional gradient in the Ti-Al FGMs fabricated by GTAW-based ALM process.

7.4 Discussion

7.4.1 Microstructure and Phase Evolution

Based on the above results, the deposited alloys exhibit a systematic change in Al content as intended by the experimental design, and there is an alloy type transition from conventional Ti alloy to Ti-Al intermetallic compounds.

The evolution of microstructures along the composition gradient can be explained in terms of the Ti-Al binary phase diagram (Figure 2.2). For the present Ti-Al graded material, the main phases present are the Ti-rich solid solution and (Ti, Al) compounds. Ideally, the Ti-rich part of the system contains three invariant reactions involving the liquid phase, i.e., $L \rightarrow \beta$, $L+\beta \rightarrow \alpha$, and $L+\alpha \rightarrow \gamma$. Figure 7.4 clearly shows that for alloys containing less than 45 at.% Al, solidification takes place solely through the β

phase. For Al concentrations of 45 ~ 49 at.%, primary β dendrites form first followed by the peritectic formation of the α phase. However, above 49 at.% Al the hexagonal α phase is the first phase to form that later transforms to the γ phase through a peritectic reaction. In Figure 7.1, these three solidification processes are identified with their corresponding composition ranges as I (L → L+β → β), II (L → L+β → β+α) and III (L → L+α → α).

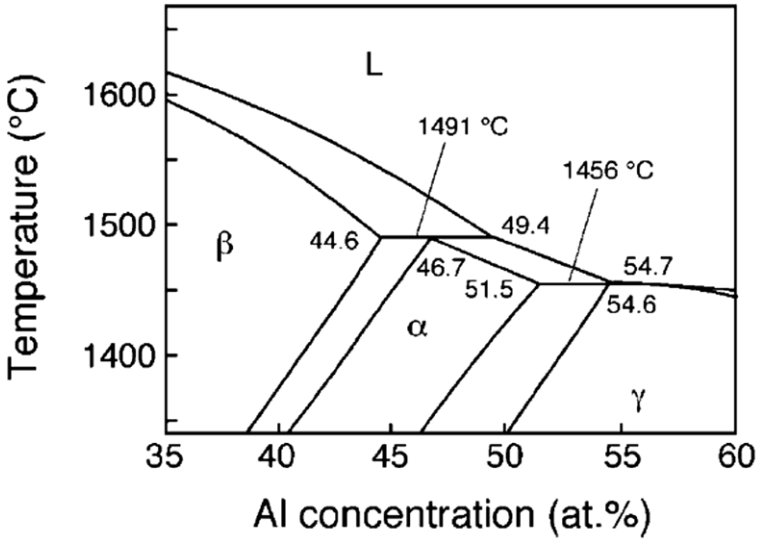

Figure 7.4 Section near the peritectic reaction of binary Ti-Al phase diagram [31].

After solidification, different solid state reactions occur in the different composition ranges. Subsequently, the deposition of a new layer remelts the upper region of the previous layer and reheats the retained part, which undergoes secondary solid state phase transformation during the subsequent periodical heat treatment. For alloys with 12-17 at.% Al, the solidified β phase experiences transformation path β → α → α+α_2, and forms a dominant acicular martensitic microstructure together with minor ordered α_2 phase. When the Al concentration is gradually increased, more α_2 phase can be obtained. The composition of Ti-(17~34) at.% Al alloy lies in a single α_2 phase field, where different types of alloys can be found on the basis of their respective site occupancy. The reason is that two different Wyckoff positions in the stoichiometric Ti_3Al phase can be occupied by aluminium and titanium atoms in two situations,

respectively [254]. It should also be noted that although similar microstructure is obtained in this composition range, the final α_2 phase forms following different transformation path. In Ti-(17~24) at.% Al alloys, the formation of α_2 phase through $\alpha \rightarrow \alpha+\alpha_2 \rightarrow \alpha_2$ is comparable with that in Ti-(12~17) at.% Al alloys. Interestingly, the α_2 phase is formed in the solid state by the peritectoid reaction $\beta+\alpha \rightarrow \alpha_2$ in Ti-(27.5~34) at.% Al alloys, but not by $\alpha+\gamma \rightarrow \alpha_2$ or $\alpha \rightarrow \alpha_2$. As such, a second peritectoid reaction $\beta+\alpha_2 \rightarrow \alpha$ occurs when Al content is in the range of 25~27.5 at.% [20]. However, both of the two peritectoid reactions hardly complete due to the limited diffusion during the non-equilibrium process. Consequently, the coarse grains are obtained ultimately in the single α_2 phase field. As Al is increasingly added into the melt pool, the $\alpha_2+\gamma$ dual phase alloys can be obtained. According to the phase diagram, the α_2 phase forms first, followed by the γ lamellae nucleation at the grain boundaries within Ti-(34~39) at.% Al alloys. The lamellar structure in these hypo-eutectoid alloys has been demonstrated to form in the same sequence as that in the eutectoid alloy in addition to the appearance of the amorphous state [255].

The materials with ~40 at.% Al concentration are expected to undergo $\beta \rightarrow \beta+\alpha \rightarrow \alpha+\gamma \rightarrow \alpha_2+\gamma$ phase transition. However, the high temperature transformation ($\alpha \rightarrow \alpha+\gamma$) is suppressed by the relatively high cooling rate in the deposition process, and only the ordering transformation $\alpha \rightarrow \alpha_2$ occurs [22]. The γ laths precipitate at the γ allotriomorph / α_2 matrix interface with Blackburn's orientation relationship $(0001)_{\alpha_2} \parallel \{111\}_{\gamma}$ and $\langle 11\bar{2}0\rangle_{\alpha_2} \parallel \langle 1\bar{1}0\rangle_{\gamma}$ [30-31]. The formation mechanism of lamellar γ phase in Ti-40 at.% Al alloy has been thoroughly investigated by Nakai et al [256]. As a result, the α_2 microstructure with more γ laths inside the grains can be found in Ti-40 at.% Al alloys as compared with Ti-(34~39) at.% Al alloys.

With an increase in Al concentration to less than 49 at.%, the ordering of α phase always occurs following with the precipitation of γ phase. Long-range diffusion of atoms plays an essential role in controlling the development of lamellar structure in

these hyper-eutectoid alloys [257]. The formation of interdendritic grains can be attributed to Al segregation [184]. The investigation in Chapter 5 has shown the solidification behaviour and phase evolution in this composition range. Further increasing Al contents can result in single γ phase materials with around 50 at.% Al. It should be clear that hexagonal α dendrites are the primary solidified phases [258]. The primary α dendrites are later surrounded by γ phase due to the peritectic reaction $\alpha \rightarrow \alpha+\gamma$. During further cooling, the interdendritic γ structure is more stable than α dendrites, which decompose into a lath structure consisting of α and γ plates. The growth of interdendritic γ back into the primary dendrites is in a cellular pattern (γ_c) in order to optimize the diffusion-controlled solute redistribution between α and γ_c [259]. When the temperature is decreased to the $\alpha \rightarrow \alpha_2$ transus, an ordering transformation starts to occur in the remaining α phase. In addition, the inhomogeneous composition in every five layers deposited by each set is not a surprising phenomenon because of diffusion at remelting during the fabrication. When depositing the first layer, the pure Ti substrate is mixed into the weld pool to form a large dilution region. Every time a new layer is deposited on the existing layer, the partially remelted top region of the previously deposited layer constitutes the dilution area for next layer. This dilution area is reduced, and hence more homogenous alloys are achieved as more Al wire is added, since the weld pool penetrates layers that have progressively lower Ti content based on the investigation in Chapter 4. Furthermore, the composition of the dilution zone is different from the proposed composition of each set. This also contributes to the abrupt composition change between different deposition sets.

7.4.2 Microhardness

Based upon the previous discussion, the trend in microhardness as a function of Al composition is expected. As demonstrated in Chapter 5, Al concentration is of vital importance in changing the microhardness. With an increase in Al addition, the volume fraction of the α_2 phase increases in a systematic manner accompanied by a decrease in

α volume fraction, and hence the microhardness increases to a maximum value when the Al content reaches into single α_2 phase field. It is interesting to note that the maximum microhardness value corresponds to a composition range of 25~33 at.% Al. The microstructure that originates from the peritectoid reaction $\beta+\alpha \rightarrow \alpha_2$ and a second peritectoid reaction $\beta+\alpha_2 \rightarrow \alpha$ in this composition range can account for this phenomenon. The slight fluctuation of microhardness in this composition range can be ascribed to the different scale of the microstructure. Conversely, the subsequent increase in Al content leads to a decrease in microhardness. The underlying cause for this trend is the decrease in volume fraction of α_2 phase with the increase in volume fraction of γ phase. The hardness of α_2 phase is almost twice that of γ phase [173] because of the considerably larger critical resolved shear stresses for dislocations to glide in the α_2-Ti_3Al phase as compared with those for activation of slip in γ-TiAl phase [193]. Furthermore, the reduction of stacking fault energy with decreasing Al concentration [192] should be considered as another influential factor on the microhardness variation. On the basis of the foregoing analysis, different combination of α, α_2 and γ phase and their volume fraction contributes to the abrupt change in microhardness.

7.5 Conclusions

In this chapter, functionally graded TiAl in situ alloys were successfully produced using the GTAW-based ALM process and separately adjusting the additive feeding speeds of pure Ti and pure Al wires to produce the desired composition. The microstructural characterisation and microhardness of the as-fabricated materials were investigated. Based on these results, the following conclusions are drawn:

1. Through proportionally increasing the Al wire feed rate, the as-fabricated component is initially composed of conventional Ti alloy and finally Ti-Al

intermetallic compounds. A smooth composition gradient from Ti to Ti-50 at.% Al is formed along the height of the component.

2. Three types of reaction L → L+β → β, L → L+β → β+α and L → L+α → α occurred in the molten metal during solidification, depending on the Al concentration. The subsequent solid state phase transformations led to the variation in the volume fraction and the morphology of the α, α_2 and γ phases, and hence the formation of complex microstructure within the final component for increasing Al content.

3. The microhardness of Ti-Al FGMs displayed a significant increase to a maximum value, and subsequently decreased after reaching a stable maximum plateau. The maximum microhardness values in the as-fabricated materials were found to occur within the composition range of 25~33 at.% Al having single α_2 phase. A combination of several factors, particularly the amount of α_2 phase and its morphology, was confirmed to govern the microhardness variation in terms of composition gradient.

8 Summary and Outlook

8.1 General Summary

In this thesis, titanium aluminide alloys were successfully fabricated using a novel approach through the combination of in-situ alloying and additive manufacturing with gas tungsten arc welding. The effect of different process parameters, such as arc current, interpass temperature and wire feed rate, on the as-fabricated materials were analysed and successful production parameters have been established. The change of as-fabricated microstructural characteristics and mechanical performance with location in the fabricated material, and the response to different post production heat treatment, were also investigated. The same process was also employed to produce functionally graded Ti-Al alloys with success. The general conclusions from this research are summarised as follows:

1. Process parameters including arc current, interpass temperature and wire feed rate did not have an observable influence on the regional distribution of microstructure in the as-fabricated materials. However, the resultant variation of α_2 phase fraction was the key factor that influenced the microhardness values.

2. The arc current strongly affected the geometry and dilution area of the as-fabricated materials. With an increase in the arc current from 120 to 160 A, more diluted Ti from the substrate resulted in a decrease of Al composition in the near-substrate zone and hence an increased presence of the more brittle α_2 phase. For this reason, an arc current of 120 A was selected as the most suitable setting for subsequent experimentation. The major effect of increasing interpass temperature was to reduce the cooling rate, which led to the change of α_2 phase fraction. When interpass temperatures was increased from 100 to 400 °C, the volume fraction of α_2 phase reduced considerably, while further increasing

interpass temperature to 500 °C had no obvious contribution. Therefore, 400 °C was considered as the most appropriate interpass temperature. Additionally, the chemical composition of the as-fabricated materials was generally uniform through the as-fabricated walls, apart from the near-substrate zone. This was primarily determined by the ratio between the Al and Ti wire-feeding rate, which further contributed to the amount change of α_2 phase.

3. Because the resulting microstructure was found to vary along the build direction, for the purposes of analysis the deposited material could be categorised into three distinct regions along the vertical build direction. The near-substrate zone exhibited equiaxed α_2 grains populated by γ lamellae, while the microstructure in the top region contained long dendrites interspersed with interdendritic γ phases having a lamellar structure. Between these two relatively narrow bounding regions, the deposited material in the middle region is mostly comprised of a series of layer bands. Fully lamellar colonies consisting of α_2 and γ lamellae were present in the band region, whereas each layer showed much coarser interdendritic γ phases surrounded by lamellar microstructure compared with top region.

4. In the middle region of the deposited material, no appreciable variation in average microhardness was found along either the build or travel directions. However, a difference of tensile properties between these two orientations was observed due to the anisotropic microstructure. However, obvious differences in microhardness and tensile properties were found throughout the entire height of the as-fabricated component. This phenomenon was ascribed to variations in Al concentration and the multiple annealing characteristics of GTAW-based ALM process.

5. By using the contour method for residual stress measurement, it was established that the residual stresses in the upper half of the fabricated components were

significantly reduced by applying low temperature stress relief heat treatment of 400 to 500 °C for 2h, with the higher treatment temperature providing a markedly improved result. However, the results also demonstrated that the effects of the low temperature stress relief heat treatment at various locations within a given component can be difficult to predict when there are significant variations in Al content throughout its geometry, producing varying microstructures that respond differently to the applied heat treatment.

6. The microstructure in majority region of as-fabricated deposits consisted of equiaxed γ grains, which coarsening after post production heat treatment at 1200 °C from 12 to 24 h, while a fully lamellar structure formed in the near-substrate zone. The response of as-fabricated deposits to post production heat treatment at 1060 °C was totally different. Discontinuous reaction occurred at this temperature. Heat treatment for 12 h resulted in partial transformation, while the majority region exhibited fine lamellar structure after 24 h heating. The microstructure in the near-substrate zone was primarily composed of discontinuous coarsening grains. These various microstructural characteristics determined the mechanical properties of the heat-treated samples. Due to the homogenous microstructure in the majority region after each post production heat treatment, the tensile properties were comparable between the build direction (Z) and travel direction (Y), whereas the anisotropic microstructure of the as-deposited samples before heat treatment resulted in significant differences in tensile properties in these same directions. In addition, the heat-treated samples at 1200 °C / 24 h exhibited lower UTS and microhardness values but higher ductility than the as-fabricated samples before heat treatment, while the 1060 °C / 24 h heat treatment resulted a much higher UTS and microhardness values but lower ductility.

7. Functionally graded Ti-Al alloys were successfully fabricated using the GTAW-based ALM process. A smooth composition gradient from Ti to Ti-50 at.% Al along the height was achieved in the as-fabricated component, corresponding to a predictable transition from conventional Ti alloy to Ti-Al intermetallic compounds.

8. For the functionally graded Ti-Al alloys, there was a dramatic increase in microhardness up to the peak value followed by a relatively stable stage in the samples with 25~33 at.% Al content range, although a slight fluctuation was found within this stage. As the Al content was further increased up to 50%, the microhardness value decreased progressively and significantly.

8.2 Future Work

This research has developed a new manufacturing process for titanium aluminide alloys and demonstrated its potential for commercial use. However, an understanding of mechanisms at work in the GTAW-based ALM process and the relationship between the resulting microstructure and mechanical properties (especially the high temperature properties) is still incomplete. Future studies are required to develop a commercial GTAW-based ALM process to fabricate Ti-Al alloy components for practical applications. The details of proposed future work are described as follows.

1. **TEM analysis of the intermetallic γ and α_2 structure in both as-fabricated and heat-treated samples.** The detailed characteristics for both compounds need to be examined for a better understanding of their formation and evolution mechanism in the ALM processed samples. Additional TEM work is required to observe dislocation morphology and its distribution in order to determine the dislocation type.

2. **In-situ studies of the high temperature phase evolution.** The phase transformation in titanium aluminide alloys can be altered by controlling the cooling rate. The intergranular and interlamellar stresses strongly influence the mechanical and thermodynamic properties of the material. Experimental work is needed to investigate the evolution of each intermetallic compound during heating and cooling and quantify its effect on the mechanical properties.

3. **Investigation of high temperature mechanical properties including creep and fatigue properties.** Because titanium aluminide alloys are promising structural materials for high temperature applications. Where components are subjected to cyclic thermomechanical loading, the creep resistance and fatigue characteristics have important implications on life expectancy and design. Future work is required to investigate the microstructure-property relationship and understand the mechanical behaviour of the ALM fabricated components at high temperature for specific application.

4. **Evaluation of residual stresses after high temperature stress relief heat treatment.** Generally, the temperature applied for standard stress relief heat treatment is always higher than the service temperature of alloys. Therefore, it is also necessary to study the residual stress evolution using high temperature heat treatment and identify the critical temperature for ALM produced components.

5. **Manufacturing functionally graded Ti-Al alloys and other intermetallics.** The preliminary study described in chapter 7 has demonstrated the feasibility of fabricating functionally graded Ti-Al alloy components, and the basic characteristics of the material have been investigated. Further studies are needed to investigate the phase transformation mechanisms, kinetics and thermodynamics, etc. Experimental work is needed to assess its unique mechanical properties at elevated temperature. Also, it would be interesting to

observe the performance of the GTAW-based ALM process in fabricating other intermetallics and binary functionally graded alloys. Such studies would contribute to a better understanding of the underpinning physics of equilibrium and non-equilibrium intermetallics, as well as the design and development of new materials using the GTAW-based ALM process.

References

1. J.H. Westbrook, *Intermetallic Compounds.* 2002.
2. M.O. F. Appel, R. Wagner, *Novel design concepts for gamma-base titanium aluminide alloys.* ntermetallics, Volume 8, Issues 9–11, 2000. 8(9-11): p. 1283-1312.
3. D.M. Dimiduk, *Gamma titanium aluminide alloys—an assessment within the competition of aerospace structural materials.* Materials Science and Engineering: A, 1999. 263(2): p. 281-288.
4. X. Wu, *Review of alloy and process development of TiAl alloy.* Intermetallics, 2006. 14(10-11): p. 1114-1122.
5. G. Sauthoff, *Multiphase intermetallic alloys for structural applications* Intermetallics, 2000. 8(9-11): p. 1101-1109.
6. D. Cormier, O. Harrysson, T. Mahale, and H. West, *Freeform fabrication of titanium aluminide via electron beam melting using prealloyed and blended powders.* Advances in Materials Science and Engineering, 2008. 2007.
7. H. Clemens and H. Kestler, *Processing and Applications of Intermetallic γ-TiAl-Based Alloys.* Advanced Engineering Materials, 2000. 2(9): p. 551-570.
8. Phill Doorbar, M.Dixon, and A. Chatterjee, *Aero-engine Titanium From Alloys To Composites.* Light Metals Technology 2009 Materials Science Forum, 2009. 618-619: p. 127-134.
9. T.J. Horn, and O. L.A. Harrysson, *Overview of current additive manufacturing technologies and selected applications.* Science Progress, 2012. 95: p. 255-282.
10. K.V. Wong, and A. Hernandez, *A Review of Additive Manufacturing.* ISRN Mechanical Engineering, 2012. 2012: p. 10.
11. V. Raghavan, *Al-Ti (Aluminum-Titanium).* Journal of Phase Equilibria and Diffusion, 2005. 26(2): p. 171-172.

12. S.V. Djanarthany, J.C. Viala, and J. Bouix, *An overview of monolithic titanium aluminides based on Ti3Al and TiAl.* Materials Chemistry and Physics, 2001. 72(3): p. 301-309.

13. S. Sarkar, S. Datta, S. Das, and D. Basu, *Oxidation protection of gamma-titanium aluminide using glass–ceramic coatings.* Surface and Coatings Technology, 2009. 203(13): p. 1797-1805.

14. R.K. Bird, T.A. Wallace, and S.N. Sankaran, *Development of protective coatings for high-temperature metallic materials.* Journal of spacecraft and rockets, 2004. 41(2): p. 213-220.

15. F. Appel, P. Beaven, and R. Wagner, *Deformation processes related to interfacial boundaries in two-phase γ-titanium aluminides.* Acta metallurgica et materialia, 1993. 41(6): p. 1721-1732.

16. E. Bumps, H. Kessler, and M. Hansen, *Titanium-aluminum system.* J. Metals (NY), 1952. 4.

17. I. Ohnuma, Y. Fujita, H. Mitsui, K. Ishikawa, R. Kainuma, and K. Ishida, *Phase Equilibria in the Ti-Al System.* Acta Materialia, 2000. 48(12): p. 3113-3123.

18. J. Braun and M. Ellner, *Phase Equilibria Investigations on the Aluminum-Rich Part of the Binary System Ti-Al.* Metallurgical and Materials Transactions A, 2001. 32(5): p. 1037-1047.

19. H. Inui and M. Haruyuki, *Structure and Deformation of Al-Rich TiAl Single Crystals.* Properties of Complex Inorganic Solids, 1997: p. 309-320.

20. J.C. Schuster and M. Palm, *Reassessment of the binary aluminum-titanium phase diagram.* Journal of phase equilibria and diffusion, 2006. 27(3): p. 255-277.

21. Y.W. Kim and D.M. Dimiduk, *Progress in the understanding of gamma titanium aluminides.* JOM, 1991. 43(8): p. 40-47.

22. F. Appel, M. Oehring, J. Paul, C. Klinkenberg, and T. Carneiro, *Physical aspects of hot-working gamma-based titanium aluminides.* Intermetallics, 2004. 12(7): p. 791-802.

23. J. Chrapoński, W. Szkliniarz, A. Kościelna, and B. Serek, *Microstructure and chemical composition of phases in Ti–48Al–2Cr–2Nb intermetallic alloy.* Materials chemistry and physics, 2003. 81(2): p. 438-442.

24. Y.L. Hao, R. Yang, Y.Y. Cui, and D. Li, *The influence of alloying on the $\alpha 2/(\alpha 2+\gamma)/\gamma$ phase boundaries in TiAl based systems.* Acta Materialia, 2000. 48(6): p. 1313-1324.

25. D.M. Dimiduk, P.L. Martin, and Y.W. Kim, *Microstructure development in gamma TiAl alloy mill products by thermomechanical processing.* Materials Science and Engineering: A, 1998. 243(1): p. 66-76.

26. H. Clemens, W. Wallgram, S. Kremmer, V. Güther, A. Otto, and A. Bartels, *Design of Novel β- Solidifying TiAl Alloys with Adjustable β/B2- Phase Fraction and Excellent Hot- Workability.* Advanced Engineering Materials, 2008. 10(8): p. 707-713.

27. R. Imayev, V. Imayev, M. Oehring, and F. Appel, *Alloy design concepts for refined gamma titanium aluminide based alloys.* Intermetallics, 2007. 15(4): p. 451-460.

28. C. Leyens and M. Peters, *Titanium and titanium alloys*. 2003: Wiley Online Library.

29. Y.W. Kim, *Microstructural evolution and mechanical properties of a forged gamma titanium aluminide alloy.* Acta Metallurgica Et Materialia, 1992. 40(6): p. 1121-1134.

30. W. Sha, *The evolution of microstructure during the processing of gamma Ti-Al alloys.* JOM, 2006. 58(9): p. 64-66.

31. F. Appel, J.D.H. Paul, and M. Oehring, *Gamma titanium aluminide alloys: science and technology*. 2011: Wiley. com.

32. S. Dey, A. Hazotte, E. Bouzy, and S. Naka, *Development of Widmanstätten laths in a near-γ TiAl alloy.* Acta materialia, 2005. 53(14): p. 3783-3794.

33. D. Hu, A. Huang, and X. Wu, *On the massive phase transformation regime in TiAl alloys: The alloying effect on massive/lamellar competition.* Intermetallics, 2007. 15(3): p. 327-332.

34. Y.W. Kim, *Effects of microstructure on the deformation and fracture of γ-TiAl alloys.* Materials Science and Engineering: A, 1995. 192: p. 519-533.

35. C. Choi, H.J. Kim, Y.T. Lee, Y.W. Kim, C.S. Lee, *Effects of microstructural parameters on the fatigue crack growth of fully lamellar γ-TiAl alloys.* Materials Science and Engineering: A, 2002. 329: p. 545-556.

36. M. Hasegawa and H. Fukutomi, *Lamellar orientation control in TiAl base alloys by a two-step compression process at high temperature.* Materials Science and Engineering: A, 2009. 508(1): p. 106-113.

37. W.O. Soboyejo, F. Ye, and T.S. Srivatsan, *The fatigue and fracture behavior of a gamma-titanium aluminide intermetallic: Influence of ductile phase reinforcement.* Engineering Fracture Mechanics, 1996. 56(3): p. 379-395.

38. F. Appel and R. Wagner, *Microstructure and deformation of two-phase γ-titanium aluminides.* Materials Science and Engineering: R, 1998. 22(5): p. 187-268.

39. S. Court, V. Vasudevan, and H. Fraser, *Deformation mechanisms in the intermetallic compound TiAl.* Philosophical Magazine A, 1990. 61(1): p. 141-158.

40. M. Yamaguchi, H. Inui, and K. Ito, *High-temperature structural intermetallics.* Acta Materialia, 2000. 48(1): p. 307-322.

41. R. Porizek, S. Znam, D. Nguyen-Manh, V. Vitek, and D. Pettifor. *Atomistic studies of dislocation glide in gamma-TiAl*. in *Materials Research Society Symposium Proceedings*. 2003. Warrendale, Pa.; Materials Research Society; 1999.

42. W. Marketz, F. Fischer, and H. Clemens, *Deformation mechanisms in TiAl intermetallics—experiments and modeling.* International Journal of Plasticity, 2003. 19(3): p. 281-321.

43. M. Legros, A. Corn, and D. Caillard, *Prismatic and basal slip in Ti_3Al I. Frictional forces on dislocations.* Philosophical Magazine A, 1996. 73(1): p. 61-80.

44. M. Legros, A. Couret, and D. Caillard, *Prismatic and basal slip in Ti_3Al II. Dislocation interactions and cross-slip processes.* Philosophical Magazine A, 1996. 73(1): p. 81-99.

45. M. Legros, Y. Minonishi, and D. Caillard, *An in-situ transmission electron microscopy study of pyramidal slip in Ti_3Al: I. Geometry and Kinetics of glide.* Philosophical Magazine A, 1997. 76(5): p. 995-1011.

46. M. Legros, Y. Minonishi, and D. Caillard, *An in-situ transmission electron microscopy study of pyramidal slip in Ti_3Al: II. Fine structure of dislocations and dislocation loops.* Philosophical Magazine A, 1997. 76(5): p. 1013-1032.

47. Y. Minonishi, *Plastic deformation of single crystals of Ti_3Al with $D0_{19}$ structure.* Philosophical Magazine A, 1991. 63(5): p. 1085-1093.

48. T. Kawabata, T. Tamura, and O. Izumi. *Parameters for Ductility Improvement in TiAl*. in *MRS Proceedings*. 1988. Cambridge Univ Press.

49. F. Meisenkothen, *Engineering the Alpha Two Phase Morphology in Gamma TiAl Based Alloys*. 2003, The Ohio State University.

50. C.Y. Jones, W.E. Luecke, and E. Copland, *Neutron Diffraction Study Oxygen Dissolution Alpha2-Ti3Al.* 2005.

51. V. Vasudevan, M. Stucke, S. Court, and H. Fraser, *The influence of second phase Ti_3Al on the deformation mechanisms in TiAl.* Philosophical magazine letters, 1989. 59(6): p. 299-307.

52. Y.W. Kim, *Strength and ductility in TiAl alloys.* Intermetallics, 1998. 6(7): p. 623-628.

53. K. Kothari, R. Radhakrishnan, and N.M. Wereley, *Advances in gamma titanium aluminides and their manufacturing techniques.* Progress in Aerospace Sciences, 2012. 55: p. 1-16.

54. M. Takeyama, *Microstructural evolution and tensile properties of titanium-rich TiAl alloy.* Materials Science and Engineering: A, 1992. 152(1): p. 269-276.

55. C. Mercer and W.O. Soboyejo, *Hall-petch relationships in gamma titanium aluminides.* Scripta Materialia, 1996. 35(1): p. 17-22.

56. C. Liu, J. Schneibel, P. Maziasz, J. Wright, and D. Easton, *Tensile properties and fracture toughness of TiAl alloys with controlled microstructures.* Intermetallics, 1996. 4(6): p. 429-440.

57. H.A. Lipsitt, D. Shechtman, and R.E. Schafrik, *The deformation and fracture of TiAl at elevated temperatures.* Metallurgical Transactions A, 1975. 6(11): p. 1991-1996.

58. T. Noda, *Application of cast gamma TiAl for automobiles.* Intermetallics, 1998. 6(7): p. 709-713.

59. T. Tetsui, *Application of TiAl in a turbocharger for passenger vehicles.* Advanced Engineering Materials, 2001. 3(5): p. 307-310.

60. Y.W. Kim and D.M. Dimiduk, *Designing gamma TiAl alloys- Fundamentals, strategy and production.* ISSI: Structural intermetallics 1997, 1997: p. 531-543.

61. K. Gebauer, *Performance, tolerance and cost of TiAl passenger car valves.* Intermetallics, 2006. 14(4): p. 355-360.

62. A. Kartavykh, S. Kaloshkin, V. Cherdyntsev, M. Gorshenkov, T. Sviridova, Y.V. Borisova, F. Senatov, and A. Maksimkin, *Application of microstructured intermetallides in turbine manufacture. Part 1: Present state and prospects (a review).* Inorganic Materials: Applied Research, 2013. 4(1): p. 12-20.

63. J. Aguilar, A. Schievenbusch, and O. Kättlitz, *Investment casting technology for production of TiAl low pressure turbine blades–process engineering and parameter analysis.* Intermetallics, 2011. 19(6): p. 757-761.

64. W. Voice, *The future use of gamma titanium aluminides by Rolls-Royce.* Aircraft Engineering and Aerospace Technology, 1999. 71(4): p. 337-340.

65. H. Clemens and W. Smarsly, *Light-weight intermetallic titanium aluminides–Status of research and development.* Advanced materials research, 2011. 278: p. 551-556.

66. S.L. Draper, B.A. Lerch, J.M. Pereira, K. Miyoshi, V.K. Arya, and W. Zhuang, *Durability Assessment of Gamma TiAl.* 2004.

67. S. Draper, D. Krause, B. Lerch, I. Locci, B. Doehnert, R. Nigam, G. Das, P. Sickles, B. Tabernig, and N. Reger, *Development and evaluation of TiAl sheet structures for hypersonic applications.* Materials Science and Engineering: A, 2007. 464(1): p. 330-342.

68. E.A. Loria, *Gamma titanium aluminides as prospective structural materials.* Intermetallics, 2000. 8(9): p. 1339-1345.

69. J.-S. Huang, B. Liu, Y.-H. Zhang, W. Zhang, X.-Y. He, Y. Liu, Y.-H. He, and B.-Y. Huang, *Microstructural Revolution of TiAl by Different Casting Method.* Journal of Materials Science and Engineering, 2009. 3(3): p. 16-21.

70. J. Bryant and S. Semiatin, *Segregation in multicomponent ingot metallurgy gamma titanium aluminides.* Scripta metallurgica et materialia, 1991. 25(2): p. 449-453.

71. M. Thomas, J. Raviart, and F. Popoff, *Cast and PM processing development in gamma aluminides.* Intermetallics, 2005. 13(9): p. 944-951.

72. L.E. Murr, S.M. Gaytan, A. Ceylan, E. Martinez, J.L. Martinez, D.H. Hernandez, B.I. Machado, D.A. Ramirez, F. Medina, S. Collins, and R.B. Wicker, *Characterization of titanium aluminide alloy components fabricated by additive manufacturing using electron beam melting.* Acta Materialia 2010. 58(5): p. 1887-1894.

73. Z.M. Sun and H. Hashimoto, *Fabrication of TiAl alloys by MA-PDS process and the mechanical properties.* Intermetallics, 2003. 11(8): p. 825-834.

74. F. Appel, U. Brossmann, U. Christoph, S. Eggert, P. Janschek, U. Lorenz, J. Müllauer, M. Oehring, and J. D. H. Paul, *Recent Progress in the Development of Gamma Titanium Aluminide Alloys.* Advanced Engineering Materials, 2000. 2(11): p. 699-720.

75. H. Clemens and S. Mayer, *Design, Processing, Microstructure, Properties, and Applications of Advanced Intermetallic TiAl Alloys.* Advanced Engineering Materials, 2013.

76. Z.C. Liu, J.P. Lin, S.J. Li, and G.L. Chen, *Effects of Nb and Al on the microstructures and mechanical properties of high Nb containing TiAl base alloys.* Intermetallics, 2002. 10(7): p. 653-659.

77. U. Prasad and M.C. Chaturvedi, *Grain coarsening in Ti–45Al based titanium aluminides at supertransus temperature and subsequent lamellar structure formation.* Materials Science and Technology, 2004. 20: p. 87-92.

78. Y.Y. Chen, Y.F.Chen, S.L. Xiao, F.T. Kong, J. Tian, and L.J. Xu, *Research on the hot precision processing of TiAl alloys.* Materials Science Forum, 2009. 620-622: p. 407-412.

79. F. Kong, Y. Chen, and F. Yang, *Effect of heat treatment on microstructures and tensile properties of as-forged Ti-45Al-5Nb-0.3Y alloy.* Intermetallics, 2011. 19(2): p. 212-216.

80. T. Lee, E. Mosunov, and S. Hwang, *Consolidation of a gamma TiAl–Mn–Mo alloy by elemental powder metallurgy.* Materials Science and Engineering: A, 1997. 239: p. 540-545.

81. W. Zhang, Y. Liu, B. Liu, and B.Y. Huang, *Comparative assessment of microstructure and compressive behaviours of PM TiAl alloy prepared by HIP and pseudo- HIP technology.* Powder Metallurgy, 2011. 54: p. 133-141.

82. Y.L. Chen, M. Yan, Y.M. Sun, B.C. Mei, and J.Q. Zhu, *The phase transformation and microstructure of TiAl/Ti_2AlC composites caused by hot pressing.* Ceramics International, 2009. 35(5): p. 1807-1812.

83. U. Habel and B.J. McTiernan, *HIP temperature and properties of a gas-atomized γ-titanium aluminide alloy.* Intermetallics, 2004. 12(1): p. 63-68.

84. R. Gerling, A. Bartels. H. Clemens, H. Kestler, and F.P. Schimansky, *Structural characterization and tensile properties of a high Nb containing gamma TiAl sheet obtained by powder metallurgical processing.* Intermetallics, 2004. 12(3): p. 275-280.

85. R. Gerling, H. Clemens, and F. Schimansky, *Powder metallurgical processing of intermetallic gamma titanium aluminides.* Advanced Engineering Materials, 2004. 6(1- 2): p. 23-38.

86. L. Hsiung and T. Nieh, *Microstructures and properties of powder metallurgy TiAl alloys.* Materials Science and Engineering: A, 2004. 364(1): p. 1-10.

87. G. Wegmann, R. Gering, F.P. Schimansky, *Temperature induced porosity in hot isostatically pressed gamma titanium aluminide alloy powders.* Acta Materialia, 2003. 51(3): p. 741-752.

88. J.-P. Kruth, M.-C. Leu, and T. Nakagawa, *Progress in additive manufacturing and rapid prototyping.* CIRP Annals-Manufacturing Technology, 1998. 47(2): p. 525-540.

89. V. Petrovica, J.V.H. Gonzalez, O.J. Ferrandoa, J.D. Gordilloa, J.R.B. Puchadesa, and L.P. Griñana, *Additive layered manufacturing sectors of industrial application shown through case studies.* International Journal of Production Research, 2011. 49(4): p. 1061-1079.

90. J.-P. Kruth, *Material incress manufacturing by rapid prototyping techniques.* CIRP Annals-Manufacturing Technology, 1991. 40(2): p. 603-614.

91. I. Campbell, D. Bourell, and I. Gibson, *Additive manufacturing: rapid prototyping comes of age.* Rapid Prototyping Journal, 2012. 18(4): p. 255-258.

92. T. Wohlers, *Developments in additive manufacturing.* Manufacturing Engineering, 2010. 144(1): p. 54-59.

93. T. Wohlers, *Additive Manufacturing Advances.* Manufacturing Engineering, 2012. 148(4): p. 55-56.

94. W.E. Frazier, *Metal additive manufacturing: A review.* Journal of Materials Engineering and Performance, 2014. 23(6): p. 1917-1928.

95. P.M.S. Almeda and S. Williams, *Innovative process model of Ti–6Al–4V additive layer manufacturing using cold metal transfer (CMT)*, in Proccedings of the 21st Annual International Solid Freeform Fabrication Symposium, University of Texas at Austin, Austin, TX, USA, August 2010.

96. I.D. Harris and A. Director, *Development and Implementation of Metals Additive Manufacturing.* DOT International, New Orleans, 2011.

97. S. Rawal, J. Brantley, and N. Karabudak. *Additive manufacturing of Ti-6Al-4V alloy components for spacecraft applications*. in *Recent Advances in Space Technologies (RAST), 2013 6th International Conference on*. 2013. IEEE.

98. S. Berumen, F. Bechmann, S. Lindner, J.-P. Kruth, and T. Craeghs, *Quality control of laser-and powder bed-based Additive Manufacturing (AM) technologies.* Physics procedia, 2010. 5: p. 617-622.

99. X. Gong, B. Cheng, S. Price, and K. Chou. *Powder-bed electron-beam-melting additive manufacturing: powder characterization, process simulation and metrology*. in *2013 ASME Early Career Technical Conference, ASME ECTC*. 2013.

100. B. Dutta, S. Palaniswamy, J. Choi, L. Song, and J. Mazumder, *Additive manufacturing by direct metal deposition.* Advanced Materials & Processes, 2011. 169(5): p. 33-36.

101. K.M. Taminger and R.A. Hafley, *Electron beam freeform fabrication for cost effective near-net shape manufacturing.* 2006.

102. D. White and D.E. Carmein, *Ultrasonic object consolidation system and method*. 2002, Google Patents.

103. Y.M. Zhang, P. Li, Y. Chen, and A.T. Male, *Automated system for welding-based rapid prototyping.* Mechatronics, 2002. 12(1): p. 37-53.

104. Y. Zhang, Y. Chen, P. Li, and A.T. Male, *Weld deposition-based rapid prototyping: a preliminary study.* Journal of Materials Processing Technology, 2003. 135(2): p. 347-357.

105. L.E. Murr, S.M. Gaytan, D.A. Ramirez, E. Martinez, J. Hernandez, K.N. Amato, P.W. Shindo, F.R. Medina, and R.B. Wicker, *Metal fabrication by additive manufacturing using laser and electron beam melting technologies.* Journal of Materials Science & Technology, 2012. 28(1): p. 1-14.

106. F. Martina, J. Mehnen, S.W. Williams, P. Colegrove, and F. Wang, *Investigation of the benefits of plasma deposition for the additive layer manufacture of Ti–6Al–4V.* Journal of Materials Processing Technology, 2012. 212(6): p. 1377-1386.

107. E. Brandl, C. Leyens, and F. Palm. *Mechanical properties of additive manufactured Ti-6Al-4V using wire and powder based processes*. in *IOP Conference Series: Materials Science and Engineering*. 2011. IOP Publishing.

108. P. Kazanas, P. Deherkar, P. Almeida, H. Lockett, and S. Williams, *Fabrication of geometrical features using wire and arc additive manufacture.* Proceedings of the Institution of Mechanical Engineers, Part B: Journal of Engineering Manufacture, 2012. 226(6): p. 1042-1051.

109. E. Brandl and D. Greitemeier, *Microstructure of additive layer manufactured Ti–6Al–4V after exceptional post heat treatments.* Materials Letters, 2012. 81: p. 84-87.

110. W.U.H. Syed, A.J. Pinkerton, and L. Li, *Combining wire and coaxial powder feeding in laser direct metal deposition for rapid prototyping.* Applied Surface Science, 2006. 252(13): p. 4803-4808.

111. N. Guo and M.C. Leu, *Additive manufacturing: technology, applications and research needs.* Frontiers of Mechanical Engineering, 2013. 8(3): p. 215-243.

112. F.P. Melchels, M.A. Domingos, T.J. Klein, J. Malda, P.J. Bartolo, and D.W. Hutmacher, *Additive manufacturing of tissues and organs.* Progress in Polymer Science, 2012. 37(8): p. 1079-1104.

113. S. Lim, R.A. Buswell, T.T. Le, S.A. Austin, A.G. Gibb, and T. Thorpe, *Developments in construction-scale additive manufacturing processes.* Automation in construction, 2012. 21: p. 262-268.

114. P. Kobryn, N. Ontko, L. Perkins, and J. Tiley, *Additive manufacturing of aerospace alloys for aircraft structures*. 2006, DTIC Document.

115. E. Louvis, P. Fox, and C.J. Sutcliffe, *Selective laser melting of aluminium components.* Journal of Materials Processing Technology, 2011. 211(2): p. 275-284.

116. E. Brandl, U. Heckenberger, V. Holzinger, and D. Buchbinder, *Additive manufactured AlSi10Mg samples using Selective Laser Melting (SLM): Microstructure, high cycle fatigue, and fracture behavior.* Materials & Design, 2012. 34: p. 159-169.

117. F. Wang, *Mechanical property study on rapid additive layer manufacture Hastelloy® X alloy by selective laser melting technology.* The International Journal of Advanced Manufacturing Technology, 2012. 58(5-8): p. 545-551.

118. Q. Jia and D. Gu, *Selective laser melting additive manufacturing of Inconel 718 superalloy parts: Densification, microstructure and properties.* Journal of Alloys and Compounds, 2014. 585: p. 713-721.

119. B. Dutta and F.H.S. Froes, *Additive manufacturing of Titanium Alloys.* Advanced Materials and Processes, 2014. 172(2): p. 18-23.

120. S. Kelly and S. Kampe, *Microstructural evolution in laser-deposited multilayer Ti-6Al-4V builds: Part I. Microstructural characterization.* Metallurgical and Materials Transactions A, 2004. 35(6): p. 1861-1867.

121. S. Kelly and S. Kampe, *Microstructural evolution in laser-deposited multilayer Ti-6Al-4V builds: Part II. Thermal modeling.* Metallurgical and Materials Transactions A, 2004. 35(6): p. 1869-1879.

122. S.H. Mok, G. Bi, J. Folkes, I. Pashby, and J. Segal, *Deposition of Ti–6Al–4V using a high power diode laser and wire, Part II: Investigation on the mechanical properties.* Surface and Coatings Technology, 2008. 202(19): p. 4613-4619.

123. S.H. Mok, G. Bi, J. Folkes, and I. Pashby, *Deposition of Ti–6Al–4V using a high power diode laser and wire, Part I: Investigation on the process characteristics.* Surface and Coatings Technology, 2008. 202(16): p. 3933-3939.

124. B. Baufeld, E. Brandl, and O.V.D. Biest, *Wire based additive layer manufacturing: Comparison of microstructure and mechanical properties of Ti-6Al-4V components fabricated by laser-beam deposition and shaped metal deposition.* Journal of Materials Processing Technology, 2011. 211(6): p. 1146-1158.

125. E. Brandl, A. Schoberth, C. Leyens, *Morphology, microstructure, and hardness of titanium (Ti-6Al-4V) blocks deposited by wire-feed additive layer manufacturing (ALM).* Materials Science and Engineering: A, 2012. 532: p. 295-307.

126. F. Wang, S. Williams, P. Colegrove, and A.A. Antonysamy, *Microstructure and Mechanical Properties of Wire and Arc Additive Manufactured Ti-6Al-4V.* Metallurgical and Materials Transactions A, 2013. 44(2): p. 968-977.

127. D. Srivastava, I. Chang, and M. Loretto, *The optimisation of processing parameters and characterisation of microstructure of direct laser fabricated TiAl alloy components.* Materials & Design, 2000. 21(4): p. 425-433.

128. D. Srivastava, I. Chang, and M. Loretto, *The effect of process parameters and heat treatment on the microstructure of direct laser fabricated TiAl alloy samples.* Intermetallics, 2001. 9(12): p. 1003-1013.

129. H. Qu and H. Wang, *Microstructure and mechanical properties of laser melting deposited γ-TiAl intermetallic alloys.* Materials Science and Engineering: A, 2007. 466(1): p. 187-194.

130. H. Qu, P. Li, S. Zhang, A. Li, and H. Wang, *The effects of heat treatment on the microstructure and mechanical property of laser melting deposition γ-TiAl intermetallic alloys.* Materials & Design, 2010. 31(4): p. 2201-2210.

131. D. Cormier and O. Harrysson. *Electron beam melting of gamma titanium aluminide*. in *The 16th Solid Freeform Fabrication Symposium, University of Texas, Austin, USA,(August 2005)*. 2005.

132. L. Murr, S. Gaytan, A. Ceylan, E. Martinez, J. Martinez, D. Hernandez, B. Machado, D. Ramirez, F. Medina, and S. Collins, *Characterization of titanium aluminide alloy components fabricated by additive manufacturing using electron beam melting.* Acta Materialia, 2010. 58(5): p. 1887-1894.

133. S. Biamino, A. Penna, U. Ackelid, S. Sabbadini, O. Tassa, P. Fino, M. Pavese, P. Gennaro, and C. Badini, *Electron beam melting of Ti-48Al-2Cr-2Nb alloy: Microstructure and mechanical properties investigation.* Intermetallics, 2011. 19(6): p. 776-781.

134. H. Saari, J. Beddoes, D.Y. Seo, and L. Zhao, *Development of directionally solidified γ-TiAl structures.* Intermetallics, 2005. 13(9): p. 937-943.

135. R.S. Mishraa and Z.Y. Ma, *Friction stir welding and processing.* Materials Science and Engineering: R: Reports, 2005. 50(1-2): p. 1-78.

136. Y. Chen and K. Nakata, *Microstructural characterization and mechanical properties in friction stir welding of aluminum and titanium dissimilar alloys.* Materials & Design, 2009. 30(3): p. 469-474.

137. A. Fuji, *In situ observation of interlayer growth during heat treatment of friction weld joint between pure titanium and pure aluminium.* Science and Technology of Welding & Joining, 2002. 7(6): p. 413-416.

138. T Shinoda, K. Ito, and C. Hayashi, *Friction welding of TiAl intermetallic compound.* Welding International, 1997. 11(3): p. 200-205.

139. A. Wu, W. Yao, G. Zou, and J. Ren, *Formation process of the bonding joint in Ti/Al diffusion bonding.* Materials Science and Engineering: A, 2008. 480(1-2): p. 456-463.

140. Y. Nakao, K. Shinozaki, and M. Hamada, *Diffusion bonding of intermetallic compound TiAl.* ISIJ International, 1991. 31(10): p. 1260-1266.

141. G. Çam, J. Müllauer, and M. Koçak, *Diffusion bonding of two phase γ-TiAl alloys with duplex microstructure.* Science and Technology of Welding & Joining, 1997. 2(5): p. 213-219.

142. A. Shapiro and A. Rabinkin, *State of the art of titanium-based brazing filler metals.* Welding Journal, 2003. 82(10): p. 36-43.

143. X.G. Song, J. Cao, H.Y. Chen, Y.F. Wang, and J.C. Feng, *Brazing TiAl intermetallics using TiNi-V eutectic brazing alloy.* Materials Science and Engineering: A, 2012. 551: p. 133-139.

144. R.K. Shiue, S.K. Wu, and S.Y. Chen, *Infrared brazing of TiAl intermetallic using Pure Silver.* Intermetallics, 2004. 12(7-9): p. 929-936.

145. S.K.W. R.K. Shiue, S.Y. Chen, *Infrared brazing of TiAl intermetallic using BAg-8 braze alloy.* Acta Materialia, 2003. 51(7): p. 1991-2004.

146. I.C. Wallis, H.S. Ubhi, M.-P. Bacos, P. Josso, J. Lindqvist, D. Lundstrom, and A. Wisbey, *Brazed joints in γ TiAl sheet: microstructure and properties.* Intermetallics, 2004. 12(3): p. 303-316.

147. U. Reisgen, J. Holk, and S. Olschok, *Electron beam welding of titanium aluminides.* Materialwissenschaft und Werkstofftechnik, 2009. 40(11): p. 820-823.

148. Q. Xu, M. Chaturvedi, and N. Richards, *The role of phase transformation in electron-beam welding of TiAl-based alloys.* Metallurgical and Materials Transactions A, 1999. 30(7): p. 1717-1726.

149. M. Chaturvedi, N. Richards, and Q. Xu, *Electron beam welding of a Ti–45Al–2Nb–2Mn+ 0.8 vol.% TiB_2 XD alloy.* Materials Science and Engineering: A, 1997. 239: p. 605-612.

150. M. Chaturvedi, Q. Xu, and N. Richards, *Development of crack-free welds in a TiAl-based alloy.* Journal of materials processing technology, 2001. 118(1): p. 74-78.

151. B. Zhang, G. Chen, W. Liu, and J. Feng, *Crack formation and control upon electron beam welding of TiAl-based alloys.* Intermetallics, 2011. 19(12): p. 1857-1863.

152. E. Akman, A. Demir, T. Canel, and T. Sinmazçelik, *Laser welding of Ti6Al4V titanium alloys.* Journal of Materials Processing Technology, 2009. 209(8): p. 3705-3713.

153. A. Wu, G. Zou, J. Ren, H. Zhang, G. Wang, X. Liu, and M. Xie, *Microstructures and mechanical properties of Ti–24Al–17Nb (at.%) laser beam welding joints.* Intermetallics, 2002. 10(7): p. 647-652.

154. M. Cabibbo, S. Marrone, and E. Quadrini, *Mechanical and microstructural characteristics of laser welded titanium–aluminium joints.* Welding international, 2005. 19(2): p. 125-129.

155. A. Short, *Gas tungsten arc welding of [alpha] + [beta] titanium alloys: a review.* Materials Science and Technology, 2009. 25(3): p. 309-324.

156. R. Wang and G. Welsch, *Joining titanium materials with tungsten inert gas welding, laser welding, and infrared brazing.* The Journal of prosthetic dentistry, 1995. 74(5): p. 521-530.

157. M. Balasubramanian, V. Jayabalan, and V. Balasubramanian, *Effect of Pulsed Current Gas Tungsten Arc Welding Parameters on Microstructure of Titanium Alloy Welds.* Journal of Manufacturing Science and Engineering, Transactions of the ASME, 2009. 131(6): p. 0645021-0645024.

158. T. Kelly. *Repair welding of gamma titanium aluminide castings*. in *24th International SAMPE Technical Conference*. 1992.

159. L. Mallory, W. Baeslack, and D. Phillips, *Evolution of the weld heat-affected zone microstructure in a Ti-48AI-2Cr-2Nb gamma titanium aluminide.* Journal of materials science letters, 1994. 13(14): p. 1061-1065.

160. R. Mallory and W. Baeslack, *Gas tungsten-arc welding of a Ti-48 Al-2 Cr-2 Nb gamma titanium aluminide.* Titanium'92: Science and technology, 1993: p. 1.

161. D. Bharani and V. Acoff, *Autogenous gas tungsten arc weldability of cast alloy Ti−48Al−2Cr−2Nb (Atomic percent) versus extruded alloy Ti−46Al−2Cr−2Nb−0.9Mo (Atomic percent).* Metallurgical and Materials Transactions A, 1998. 29(13): p. 927-935.

162. A.V. Arenas MF, *Analysis of Gamma Titanium Aluminide welds produced by Gas Tungsten Arc welding.* Welding Journal, 2003. 5(72): p. 110-115.

163. M.F. Arenas and V.L. Acoff, *The effect of postweld heat treatment on gas tungsten arc welded gamma titanium aluminide.* Scripta Materialia, 2002. 46(3): p. 241-246.

164. A.J. Studer, M.E. Hagen, and T.J. Noakes, *Wombat: The high-intensity powder diffractometer at the OPAL reactor.* Physica B: Condensed Matter, 2006. 385: p. 1013-1015.

165. B. Baufeld, O.V.D. Biest, and R. Gault, *Additive manufacturing of Ti6Al4V components by shaped metal deposition: Microstructure and mechanical properties.* Materials & Design, 2010. 31: p. S106-S111.

166. J. Xiong, G. Zhang, Z. Qiu, and Y. Li, *Vision-sensing and bead width control of a single-bead multi-layer part: material and energy savings in GMAW-based rapid manufacturing.* Journal of Cleaner Production, 2013. 41: p. 82-88.

167. R.S. Funderburk, *The Importance of Interpass temperature.* Welding Innovation, 1998. XV(1).

168. H. Wang, W. Jiang, J. Ouyang, and R. Kovacevic, *Rapid prototyping of 4043 Al-alloy parts by VP-GTAW.* Journal of Materials Processing Technology, 2004. 148(1): p. 93-102.

169. E. Brandl, V. Michailov, B. Viehweger, and C. Leyens, *Deposition of Ti–6Al–4V using laser and wire, part I: Microstructural properties of single beads.* Surface and Coatings Technology, 2011. 206(6): p. 1120-1129.

170. B. Choi, Y. Deng, C. McCullough, B. Paden, and R. Mehrabian, *Densification of rapidly solidified titanium aluminide powders—I. Comparison of experiments to hiping models.* Acta Metallurgica Et Materialia, 1990. 38(11): p. 2225-2243.

171. E.L. Hall and S.-C. Huang, *Microstructures of rapidly-solidified binary TiAl alloys.* Acta Metallurgica Et Materialia, 1990. 38(4): p. 539-549.

172. M. Oehring, V. Küstner, F. Appel, and U. Lorenz. *Analysis of the solidification microstructure of multi-component γ-TiAl alloys*. in *Materials science forum*. 2007. Trans Tech Publ.

173. M. Göken, M. Kempf, and W. Nix, *Hardness and modulus of the lamellar microstructure in PST-TiAl studied by nanoindentations and AFM.* Acta materialia, 2001. 49(5): p. 903-911.

174. F. Wang, S. Williams, and M. Rush, *Morphology investigation on direct current pulsed gas tungsten arc welded additive layer manufactured Ti6Al4V alloy.* The International Journal of Advanced Manufacturing Technology, 2011. 57(5-8): p. 597-603.

175. H. Yang and C. Lin, *Phase transformation and microstructural evolution in Ti-44Al-4Nb-4Zr alloy during heat treatment.* Metallurgical and Materials Transactions A, 2006. 37(11): p. 3191-3196.

176. N. Hrabe and T. Quinn, *Effects of processing on microstructure and mechanical properties of a titanium alloy (Ti–6Al–4V) fabricated using electron beam melting (EBM), part 1: Distance from build plate and part size.* Materials Science and Engineering: A, 2013. 573: p. 264-270.

177. L. Qian, J. Mei, J. Liang, and X. Wu, *Influence of position and laser power on thermal history and microstructure of direct laser fabricated Ti–6Al–4V samples.* Materials science and technology, 2005. 21(5): p. 597-605.

178. A. Duarte, F. Viana, and H.M. Santos, *As-cast titanium aluminides microstructure modification.* Materials research, 1999. 2(3): p. 191-195.

179. G. Wu and Z. Huang, *Weldability and microstructure of laser-surface-remelted TiAl intermetallic alloy.* Materials Science and Engineering: A, 2003. 345(1): p. 286-292.

180. C. Liu, X. Tian, H. Tang, and H. Wang, *Microstructural characterization of laser melting deposited Ti–5Al-5Mo–5V–1Cr–1Fe near β titanium alloy.* Journal of Alloys and Compounds, 2013. 572: p. 17-24.

181. J.H. Westbrook, *Intermetallic compounds.* John Wiley & Sons: New York, 1967; p. 541.

182. J.K. M. Peters, C.H. Ward, C. Leyens, *Titanium Alloys for Aerospace Applications.* Advanced Engineering Materials, 2003. 5(6): p. 419-427.

183. S. Jones and M. Kaufman, *Phase equilibria and transformations in intermediate titanium-aluminum alloys.* Acta metallurgica et materialia, 1993. 41(2): p. 387-398.

184. H. Sun, Z. Huang, D. Zhu, and X. Jiang, *Dendrite core grain refining and interdendritic coarsening behaviour in W-containing γ-TiAl based alloys.* Journal of Alloys and Compounds, 2013. 552: p. 213-218.

185. Y. Wang, Y. Liu, G.-Y. Yang, H.-Z. Li, and B. Tang, *Microstructure of cast γ-TiAl based alloy solidified from β phase region.* Transactions of Nonferrous Metals Society of China, 2011. 21(2): p. 215-222.

186. A. Singh, K. Muraleedharan, and D. Banerjee, *Solidification structure in a cast γ alloy.* Scripta materialia, 2003. 48(6): p. 767-772.

187. D.M. Dimiduk, P.M. Hazzledine, T.A. Parthasarathy, M.G. Mendiratta, and S. Seshagiri, *The role of grain size and selected microstructural parameters in*

strengthening fully lamellar TiAl alloys. Metallurgical and Materials Transactions A, 1998. 29(1): p. 37-47.

188. G. Dehm, C. Motz, C. Scheu, H. Clemens, P.H. Mayrhofer, and C. Mitterer, *Mechanical Size- Effects in Miniaturized and Bulk Materials.* Advanced Engineering Materials, 2006. 8(11): p. 1033-1045.

189. L. Cha, C. Scheu, H. Clemens, H.F. Chladil, G. Dehm, R. Gerling, and A. Bartels, *Nanometer-scaled lamellar microstructures in Ti–45Al–7.5Nb–(0; 0.5)C alloys and their influence on hardness.* Intermetallics, 2008. 16(7): p. 868-875.

190. E. Arzt, G. Dehm, P. Gumbsch, O. Kraft, and D. Weiss, *Interface controlled plasticity in metals: dispersion hardening and thin film deformation.* Progress in Materials science, 2001. 46(3): p. 283-307.

191. Y.S. Sato, S.H.C. Park, and H. Kokawa, *Microstructural factors governing hardness in friction-stir welds of solid-solution-hardened Al alloys.* Metallurgical and Materials Transactions A, 2001. 32(12): p. 3033-3042.

192. S.-C. Huang and E.L. Hall, *Plastic deformation and fracture of binary TiAl-base alloys.* Metallurgical Transactions A, 1991. 22(2): p. 427-439.

193. J.M. Wiezorek, X.-D. Zhang, W.A. Clark, and H.L. Fraser, *Activation of slip in lamellae of alpha2-Ti_3Al in TiAl alloys.* Philosophical Magazine A, 1998. 78(1): p. 217-238.

194. E. Brandl, B. Baufeld, C. Leyens, and R. Gault, *Additive manufactured Ti-6Al-4V using welding wire comparison of laser and arc beam deposition and evaluation with respect to aerospace material specifications.* Physics Procedia, 2010. 5: p. 595-606.

195. K. Chan and Y. Kim, *Effects of lamellae spacing and colony size on the fracture resistance of a fully-lamellar TiAl alloy.* Acta metallurgica et materialia, 1995. 43(2): p. 439-451.

196. R. Leggatt, *Residual stresses in welded structures.* International Journal of Pressure Vessels and Piping, 2008. 85(3): p. 144-151.

197. X. Cheng, J.W. Fisher, H.J. Prask, T. Gnäupel-Herold, B.T. Yen, and S. Roy, *Residual stress modification by post-weld treatment and its beneficial effect on fatigue strength of welded structures.* International Journal of Fatigue, 2003. 25(9): p. 1259-1269.

198. A. Olabi and M. Hashmi, *The effect of post-weld heat-treatment on mechanical-properties and residual-stresses mapping in welded structural steel.* Journal of materials processing technology, 1995. 55(2): p. 117-122.

199. A. Aloraier, R. Ibrahim, and J. Ghojel, *Eliminating post-weld heat treatment in repair welding by temper bead technique: role bead sequence in metallurgical changes.* Journal of materials processing technology, 2004. 153: p. 392-400.

200. P. McQuay, D. Dimiduk, and S. Semiatin, *The decomposition of alpha phase during continuous cooling and isothermal transformation in gamma titanium aluminide.* Scripta metallurgica et materialia, 1991. 25(7): p. 1689-1694.

201. D. Hu and R. Botten, *Phase transformations in some TiAl-based alloys.* Intermetallics, 2002. 10(7): p. 701-715.

202. A. Singh and D. Banerjee, *Transformations in α_2+ γ titanium aluminide alloys containing molybdenum: Part II. Heat treatment.* Metallurgical and Materials Transactions A, 1997. 28(9): p. 1745-1753.

203. X. Zhang, T. Dean, and M. Loretto, *Phase transformation and structural morphologies of Ti-50Al-2Nb-2Mn during the heat treatment.* Acta metallurgica et materialia, 1994. 42(6): p. 2035-2042.

204. M. Su, Z. Lang, L. Zheng, J. Yan, K. Guan, and H. Zhang, *Effect of heat treatment on microstructures and mechanical properties in a full lamellar PM TiAl alloy.* Materials Research, 2012. 15(3): p. 455-460.

205. J. Yang, J. Wang, Y. Wang, and Q. Xia, *Refining grain size of a TiAl alloy by cyclic heat treatment through discontinuous coarsening.* Intermetallics, 2003. 11(9): p. 971-974.

206. M. Perez-Bravo, I. Madariaga, K. Ostolaza, and M. Tello, *Microstructural refinement of a TiAl alloy by a two step heat treatment.* Scripta materialia, 2005. 53(10): p. 1141-1146.

207. J. Liu, V. Ventzke, P. Staron, N. Schell, N. Kashaev, and N. Huber, *Effect of Post-weld Heat Treatment on Microstructure and Mechanical Properties of Laser Beam Welded TiAl-based Alloy.* Metallurgical and Materials Transactions A, 2014. 45(1): p. 16-28.

208. J. Liu, M. Dahmen, V. Ventzke, N. Kashaev, and R. Poprawe, *The effect of heat treatment on crack control and grain refinement in laser beam welded β-solidifying TiAl-based alloy.* Intermetallics, 2013. 40: p. 65-70.

209. M.B. Prime, *Cross-sectional mapping of residual stresses by measuring the surface contour after a cut.* Journal of Engineering Materials and Technology, 2001. 123(2): p. 162-168.

210. T. Schmoelzer, K.D. Liss, P. Staron, S. Mayer, and H. Clemens, *The Contribution of High- Energy X- Rays and Neutrons to Characterization and Development of Intermetallic Titanium Aluminides.* Advanced engineering materials, 2011. 13(8): p. 685-699.

211. D. Thibault, P. Bocher, M. Thomas, M. Gharghouri, and M. Côté, *Residual stress characterization in low transformation temperature 13% Cr–4% Ni stainless steel weld by neutron diffraction and the contour method.* Materials Science and Engineering: A, 2010. 527(23): p. 6205-6210.

212. M. Mochizuki, M. Hayashi, and T. Hattori, *Residual stress distribution depending on welding sequence in multi-pass welded joints with X-shaped groove.* Journal of pressure vessel technology, 2000. 122(1): p. 27-32.

213. P. Withers and H. Bhadeshia, *Residual stress. Part 2–Nature and origins.* Materials Science and Technology, 2001. 17(4): p. 366-375.

214. A.M. Pardowska, J.W. Price, T.R. Finlayson, and R. Ibrahim. *Evaluation of residual stress measurements before and after post-weld heat treatment in the weld repairs*. in *Journal of Physics: Conference Series*. 2010. IOP Publishing.

215. A. Paradowska, J. Price, P. Dayawansa, B. Kerezsi, X. Zhao, and R. Ibrahim. *Measurement of residual stress distribution in tubular joints considering post weld heat treatment*. in *Materials Forum*. 2006.

216. W. Zhang, B. Reddy, and S. Deevi, *Physical properties of TiAl-base alloys.* Scripta Materialia, 2001. 45(6): p. 645-651.

217. R. Ramanujan, P. Maziasz, and C. Liu, *The thermal stability of the microstructure of γ-based titanium aluminides.* Acta materialia, 1996. 44(7): p. 2611-2642.

218. A. Denquin and S. Naka, *Various transformation modes observed in two-phase γ+ α_2 TiAl-based alloys.* Le Journal de Physique IV, 1993. 3(C7): p. C7-383-C7-388.

219. J. Yang and W.-S. Hwang, *The preparation of TiAl-based intermetallics from elemental powders through a two-step pressureless sintering process.* Journal of materials engineering and performance, 1998. 7(3): p. 385-392.

220. O. Berteaux, F. Popoff, and M. Thomas, *An Experimental Assessment of the Effects of Heat Treatment on the Microstructure of Ti-47Al-2Cr-2Nb Powder Compacts.* Metallurgical and Materials Transactions A, 2008. 39(10): p. 2281-2296.

221. S. Mitao and L. Bendersky, *Morphology and growth kinetics of discontinuous coarsening in fully lamellar Ti-44Al (at.%) alloy.* Acta Materialia, 1997. 45(11): p. 4475-4489.

222. A. Denquin and S. Naka, *Phase transformation mechanisms involved in two-phase TiAl-based alloys—II. Discontinuous coarsening and massive-type transformation.* Acta materialia, 1996. 44(1): p. 353-365.

223. J. Jung and J. Park, *Growth kinetics of discontinuous coarsening of lamellar structure in Ti–44at.%Al(–0.5at.%Cr) intermetallic compounds.* Acta materialia, 1998. 46(12): p. 4123-4130.

224. G. Qin, K. Oikawa, Z. Sun, S. Sumi, T. Ikeshoji, J. Wang, S. Guo, and S. Hao, *Discontinuous Coarsening of the Lamellar Structure of γ-TiAl–based Intermetallic Alloys and Its Control.* change, 2001. 7: p. 22.

225. G. Qin, J. Wang, and S. Hao, *Discontinuous coarsening of primary α_2/γ lamellae at colony boundaries in γ-TiAl-based alloys.* Intermetallics, 1999. 7(1): p. 1-4.

226. D.S. Shong and Y.-W. Kim, *Discontinuous coarsening of high perfection lamellae in titanium aluminides.* Scripta metallurgica, 1989. 23(2): p. 257-261.

227. P. Maziasz and C. Liu, *Development of ultrafine lamellar structures in two-phase γ-TiAl alloys.* Metallurgical and Materials Transactions A, 1998. 29(1): p. 105-117.

228. P. Maziasz, C. Liu, and J. Wright, *Stability of ultrafine lamellar structures during aging in two-phase {gamma}-TiAl alloys*. 1997, Oak Ridge National Lab., TN (United States).

229. M. Grange, J. Raviart, and M. Thomas, *Influence of microstructure on tensile and creep properties of a new castable TiAl-based alloy.* Metallurgical and Materials Transactions A, 2004. 35(7): p. 2087-2102.

230. D. Hu, H. Jiang, and X. Wu, *Microstructure and tensile properties of cast Ti-44Al-4Nb-4Hf-0.1Si-0.1B alloy with refined lamellar microstructures.* Intermetallics, 2009. 17(9): p. 744-748.

231. V. Recina, D. Lundström, and B. Karlsson, *Tensile, creep, and low-cycle fatigue behavior of a cast γ-TiAl-based alloy for gas turbine applications.* Metallurgical and Materials Transactions A, 2002. 33(9): p. 2869-2881.

232. M. Yamaguchi and H. Inui, *Microstructure and mechanical properties of two-phase TiAl alloys in lamellar form.* Journal of Materials Science & Technology, 1994. 3: p. 005.

233. J. Gandra, R. Miranda, P. Vilaca, A. Velhinho, and J.P. Teixeira, *Functionally graded materials produced by friction stir processing.* Journal of Materials Processing Technology, 2011. 211(11): p. 1659-1668.

234. T. Rajan, E. Jayakumar, and B. Pai, *Developments in solidification processing of functionally graded aluminium alloys and composites by centrifugal casting technique.* Transactions of the Indian Institute of Metals, 2012. 65(6): p. 531-537.

235. J. Reddy and C. Chin, *Thermomechanical analysis of functionally graded cylinders and plates.* Journal of Thermal Stresses, 1998. 21(6): p. 593-626.

236. X. Lin, T. Yue, H. Yang, and W. Huang, *Microstructure and phase evolution in laser rapid forming of a functionally graded Ti–Rene88DT alloy.* Acta materialia, 2006. 54(7): p. 1901-1915.

237. P. Babalola, C. Bolu, A. Inegbenebor, and K. Odunfa, *Development of Aluminium Matrix Composites: A review.* Online International Journal of Engineering and Technology Research, 2014. 2: p. 1-11.

238. T. Niendorf, S. Leuders, A. Riemer, F. Brenne, T. Tröster, H.A. Richard, and D. Schwarze, *Functionally Graded Alloys Obtained by Additive Manufacturing.* Advanced Engineering Materials, 2014.

239. S. Forth, L. Favrow, W. Keat, and J. Newman, *Three-dimensional mixed-mode fatigue crack growth in a functionally graded titanium alloy.* Engineering fracture mechanics, 2003. 70(15): p. 2175-2185.

240. R. Banerjee, P. Collins, D. Bhattacharyya, S. Banerjee, and H. Fraser, *Microstructural evolution in laser deposited compositionally graded α/β titanium-vanadium alloys.* Acta Materialia, 2003. 51(11): p. 3277-3292.

241. X.J. Xu, X. Lin, J. Chen, F. He, and W.D. Huang. *Laser Rapid Forming of Ti-Ni Functionally Graded Alloy*. in *Materials Science Forum*. 2007. Trans Tech Publ.

242. T. Rajan, R. Pillai, and B. Pai, *Functionally graded Al–Al_3Ni in situ intermetallic composites: Fabrication and microstructural characterization.* Journal of Alloys and Compounds, 2008. 453(1): p. L4-L7.

243. Y. Watanabe and Y. Fukui, *Microscopic study of Al-based intermetallics compound-dispersed functionally graded materials fabricated by a centrifugal method.* Formatex Microscopy Book Series, 2004. 2: p. 189-198.

244. Y. Watanabe, A. Kawamoto, and K. Matsuda, *Particle size distributions in functionally graded materials fabricated by the centrifugal solid-particle method.* Composites Science and Technology, 2002. 62(6): p. 881-888.

245. K. Yamagiwa, Y. Watanabe, Y. Fukui, and P. Kapranos, *Novel recycling system of aluminum and iron wastes–In-situ Al-Al_3Fe functionally graded material manufactured by a centrifugal method.* Mater. Trans, 2003. 44(12): p. 2461-2467.

246. J.-M. Lee, S.-B. Kang, T. Sato, H. Tezuka, and A. Kamio, *Evolution of iron aluminide in Al/Fe in situ composites fabricated by plasma synthesis method.* Materials Science and Engineering: A, 2003. 362(1): p. 257-263.

247. T. Chen, J. Li, and Y. Hao, *Microstructures and corrosion properties of casting in situ Al3Ti-Al composites.* Rare Metals, 2010. 29(1): p. 78-85.

248. C. Tijun, L. Jian, and H. Yuan, *Casting fabrication of in situ Al3Ti-Al composites and their wear behaviors.* Research & Development, 2009.

249. Y. Watanabe and S. Oike, *Formation mechanism of graded composition in Al–Al_2Cu functionally graded materials fabricated by a centrifugal in situ method.* Acta materialia, 2005. 53(6): p. 1631-1641.

250. A. Mortensen and S. Suresh, *Functionally graded metals and metal-ceramic composites: Part 1 Processing.* International Materials Reviews, 1995. 40(6): p. 239-265.

251. B. Kieback, A. Neubrand, and H. Riedel, *Processing techniques for functionally graded materials.* Materials Science and Engineering: A, 2003. 362(1): p. 81-106.

252. P. Collins, R. Banerjee, S. Banerjee, and H. Fraser, *Laser deposition of compositionally graded titanium–vanadium and titanium–molybdenum alloys.* Materials Science and Engineering: A, 2003. 352(1): p. 118-128.

253. J. Jung, J. Park, and C. Chun, *Influence of Al content on cast microstructures of Ti–Al intermetallic compounds.* Intermetallics, 1999. 7(9): p. 1033-1041.

254. S. Banumathy, P. Ghosal, and A. Singh, *On the structure of the Ti3Al phase in Ti–Al and Ti–Al–Nb alloys.* Journal of Alloys and Compounds, 2005. 394(1-2): p. 181-185.

255. M. Tanimura, Y. Inoue, and Y. Koyama, *Mechanism of* $\alpha \rightarrow \alpha_2 + \gamma$ *phase separation in hypo-eutectoid Ti-37 at% Al alloy.* Materials transactions-JIM, 1998. 39(1): p. 57-61.

256. K. Nakai, T. Ono, H. Ohtsubo, and Y. Ohmori, *Formation process of lamellar* γ *phase in a Ti-40at.% Al alloy.* Materials transactions-JIM, 1996. 37(4): p. 813-820.

257. K. Hono, E. Abe, T. Kumagai, and H. Harada, *Chemical compositions of ultrafine lamellae in the water-quenched Ti-48Al alloy.* Scripta materialia, 1996. 35(4): p. 495-499.

258. C. McCullough, J. Valencia, C. Levi, and R. Mehrabian, *Phase equilibria and solidification in Ti-Al alloys.* Acta Metallurgica, 1989. 37(5): p. 1321-1336.

259. J. Valencia, C. McCullough, C. Levi, and R. Mehrabian, *Solidification microstructure of supercooled Ti-Al alloys containing intermetallic phases.* Acta Metallurgica, 1989. 37(9): p. 2517-2530.

List of Publications during PhD Course

1. **Y. Ma**, D. Cuiuri, N. Hoye, H. Li and Z. Pan: Characterization of in-situ alloyed and additively manufactured titanium aluminides. *Metallurgical and Materials Transactions B*, 2014, 45(6), pp. 2299-2303.
2. **Y. Ma**, D. Cuiuri, N. Hoye, H. Li and Z. Pan: Effects of wire feed conditions on in situ alloying and additive layer manufacturing of titanium aluminides using gas tungsten arc welding. *Journal of Materials Research*, 2014, 29(17), pp. 2066-2071.
3. **Y. Ma**, D. Cuiuri, N. Hoye, H. Li and Z. Pan: The effect of location on the microstructure and mechanical properties of titanium aluminides produced by additive layer manufacturing using in-situ alloying and gas tungsten arc welding. *Materials Science & Engineering A*, 2015, 631, pp. 230-240.
4. **Y. Ma**, D. Cuiuri, C. Shen, H. Li and Z. Pan: Effect of interpass temperature on in-situ alloying and additive layer manufacturing of titanium aluminides using gas tungsten arc welding. *Additive Manufacturing*, under review.
5. **Y. Ma**, D. Cuiuri, N. Hoye, H. Li and Z. Pan: Effect of arc current on in-situ alloying and additive layer manufacturing of titanium aluminides using gas tungsten arc welding. *67th IIW Annual Assembly and International Conference*, July 2014, Seoul, Korea.

6. **Y. Ma**, D. Cuiuri, C. Shen, H. Li and Z. Pan: The effect of heat treatment on additively manufactured γ-TiAl based alloys. *Ti-2015: 13th World Conference on Titanium*, August 2015, San Diego, CA, USA, accepted.
7. C. Shen, Z. Pan, **Y. Ma**, D. Cuiuri and H. Li: Fabrication of Fe_3Al based Fe-Al intermetallics using the wire-arc additive layer manufacturing process, *Additive Manufacturing*, accepted.
8. S. Uzgur, H. Li, M.C. Kushan, **Y. Ma**, Y. Uzunonat and F. Diltemiz: Electron Beam Welding Varestraint Test of ALLVAC 718 Plus™ for Aviation Technology. *Advanced Science Letters*, 2012, 13(1): pp. 831-832.